

Journal of Radar and Optic Remote Sensing

Volume 1, Issue 1

February – March 2018

Islamic Azad University, Yazd Branch, Iran

Permission to publish Journal of Radar and Optic Remote Sensing

With respect to the Reference Number: **96/ص/87/7** dated 1396/01/14 (3th April 2017), the 104th commission session was held to evaluate and approve the scientific journal of the Islamic Azad University. The commission announced to grant permission to establish the journal entitled “Journal of Radar and Optic Remote Sensing”.

Editorial team of JRORS

Editor- in-chief

Dr. S. Ali Almodaresi - Associate Professor, GIS and RS Department, Yazd Branch, Islamic Azad University

Associate Editor- in-chief

Dr. Ali Akbar Jamali - Associate Professor, Department of GIS-RS and Natural Engineering, Maybod Branch, Islamic Azad University

Editorial Board

Dr. Mohammad Hossein Ramesht - Professor, Department of geography, Isfahan University

Dr. Seyed Kazem Alavi Panah - Professor, Department of Remote Sensing and GIS, Tehran university

Dr. Ali Sarkargar - Part-time faculty member of Yazd Branch, Islamic Azad University

Dr. Hooman Latifi - Assistant professor, Department of Remote Sensing of the University of Wuerzburg,

Dr. Mahdi Motagh - Department of Geodesy and Remote Sensing, Helmholtz-Zentrum Potsdam

Dr. Mostafa Khabbazi - Faculty member of Shahid Bahonar University of Kerman

Dr. karim Naghdi - Faculty member of Taft Branch, Islamic Azad University

Executive Manager

Atefeh Hemmati - Faculty member of Abarkouh Branch, Islamic Azad University

English language editor

Dr. Ali Boloor - Department of Arts and Architecture, Islamic Azad University, Yazd Branch

Journal designer

Mohsen Eghbali - Department of Computer software engineering, Yazd Branch, Islamic Azad University, Yazd, Iran

Acknowledgement

JRORS would like to thank the following people for their contributions to this volume.

Reviewers

Dr. Fazel Amiri

Dr. Mohammad Zare

Dr. Mohammad Hosein Mokhtari

Dr. Ali Akbar Jamali

Dr. Jalal Karami

Dr. Mohammad Hosein Saraei

Dr. Reza Attarzade

In the Name of God

Dear Readers,

I have the enormous opportunity to share the first journal publication to the readers. The Journal of Radar and Optic Remote Sensing (JRORS) is the first radar journal and the first scientific journal in this area of Islamic Azad University (2017). The first issue will be published this year by the Islamic Azad University, Yazd Branch. The publication of the articles resulting from the scholarly research findings contributes to the advancement of knowledge and performance of remote sensing and radar. This journal focuses on original research papers that develop a basic knowledge in the field of remote sensing and radar.

Over the past years, many research articles have been received in the specialized field and just a few have been accepted for publication in each issue based on the reviewers' and the editorial team's decisions regarding the articles. This has somehow upset the authors. Therefore, an apology on behalf of the editorial team for declining and or delaying the publication of some of these inter-disciplinary scholarly articles. It is hoped to add the scientific richness of the journal by releasing articles that reflect your valuable research activities, providing us with the latest publications in the scientific community of remote sensing and radar.

Finally, I would like to sincerely thank the Editorial Board for their dedication to prepare the first issue. It was their efforts that made it possible to publish the first issue on time.

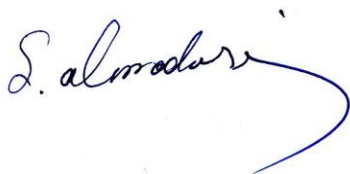
Sincerely,

Dr. Seyed Ali Almodaresi

Editor-in-Chief

Journal of Radar and Optic Remote Sensing

www.jrors.ir



INDEX

NO	TITLE	PAGES
1	Introduction	i-vi
2	Identification of Active Structures via Remote Sensing <i>Vahid Hosseinitoudeshk</i>	7-14
3	Investigation of Urban Biophysical Compounds in the Formation of Thermal Islands Using RS and GIS (Case Study: Yazd) <i>Sedigheh Emami, esmail Emami</i>	15-35
4	Evaluation of super-resolution algorithm for detection and recognition of features from MODIS and OLI images at sub-pixel scale using Hopfield Neural Network <i>Mohammad Hosein Mehrzadeh Abarghooee, Ali Sarkargar Ardakani</i>	36-57
5	Using Remote Sensing to determination of relationship between vegetation indices and vegetation percentage (case study: Darab plain in Fars province, Iran) <i>M.Mokarram, A.R.Mahmoodi</i>	58-67
6	Detecting Spatial-Temporal Changes in Land Use Using Satellite Data in Haraz Basin <i>Naser Ahmadi Sani, Karim Solaimani, Lida Razaghnia</i>	68-82
7	Study of Bio ecological and land cover change of Northern Lands of Khuzestan by Remote Sensing <i>Sara shirzad , Babak Maghsoudi Damavandi , Hamed Piri</i>	83-95

Identification of Active Structures via Remote Sensing

Vahid Hosseinitoudeshki*

Department of Civil Engineering, Zanjan Branch, Islamic Azad University, Zanjan, Iran

Received 1 January 2018; revised 6 April 2018; accepted 16 May 2018

Abstract

Active structures have an important role in controlling fluvial systems through longitudinal and lateral tilting. The Ghezel Ozan River in northwest of Iran has responded to ongoing tectonic deformation in the basin. The study area is located in the Western Alborz zone and includes part of the Ghezel Ozan River. This paper presents the role of active structures in making active deformations via detection and characterization of fluvial anomalies and correlation with structures. The study area is characterized by association of fluvial anomalies viz. deflection, anomalous sinuosity variations and knick point in longitudinal profile. Such fluvial anomalies have been identified on the repetitive satellite images and maps; and interpreted through Digital Elevation Model and field observations to identify the active structures in the area. Some of the structures in the study area have caused the fluvial anomalies; and the most active structures are surface and sub-surface faults and folds with trend of NE-SW.

Keywords: Active structures; Ghezel Ozan River; Fluvial anomalies

* Corresponding author. Tel: +98-2634302278.

E-mail address: v.h.toudeshki@iauz.ac.ir.

1. Introduction

River responses to active tectonics produce geomorphological anomalies manifesting surface deformation in any area. These processes can be responsible for river incision and river diversions. River incision is related to tectonic uplift, although other processes such as base-level lowering and climatic variations are also responsible for river incision (Pérez-Peña et al., 2010).

The interactions between tectonic uplift and river erosion are fundamental processes which have acted to shape the landscapes. The geomorphic analyses are useful to investigate the impact of tectonic activity on geomorphic processes and landscape development (Giaconia et al., 2012). Tectonic geomorphology aims to highlight the behavior of active faults and the successive earthquakes that they generate (Ritz et al., 2016). Geomorphic indices are useful indicators for evaluating the influence of active tectonics (Cheng et al., 2016). Geomorphic indices have been used as a tool to identify the region deformed by active faults (Pedrera et al., 2009; Perez-Peña et al., 2010). Mahmood and Gloaguen (2012) have used geomorphic indices to compute the IRAT using GIS at the Hindu Kush, Karakorum, and Himalayas ranges. Sarp and Duzgun (2012) have tested the significance of the morphometric indices in tectonically active Bolu pull-apart basin.

The indicative values of the IRAT are compatible with uplift rates. Gao et al. (2013) have used geomorphic indices such as the hypsometric integral index to evaluate the recent uplift of the northeastern margin of the Tibetan Plateau. Alipoor et al. (2011) recognized active tectonics using geomorphic indices in the High Zagros Belt (SW of Iran). The morphometric analyses for assessing relative tectonic activity were applied for the Sarvestan area of central Zagros (Iran) (Dehbozorgi et al., 2010). Demoulin et al. (2015) have studied the patterns of Quaternary tectonic movements in the area of the Corinth rift (north Peloponnese, Greece) by fluvial landscape morphometry. Sarp (2014) has analyzed the tectonic and geomorphic history of the Bingol pull-apart basin based on morphometric features. Pirasteh (2018) applied The Light Detection and Ranging (LiDAR) techniques to investigate tectonic geomorphology analysis of the Karun River mobility with high resolution Digital Elevation Models (DEMs). The Karun River responses were investigated by using an integration of LiDAR, geomorphology, and field survey to determine the tectonic geomorphology signatures.

The studies in Iran terrene have shown ongoing convergence and active tectonic in this area (Jackson et al., 2002; Allen et al., 2003; Allen et al., 2004). This paper presents the results of studies from the part of the Ghezel Ozan River basin in northwest of Iran. One of the major unresolved questions is whether the drainage and topographic features of the Ghezel Ozan River are due to the recent Tectonism. The main objective of this paper is to evaluate the drainage basin of the Ghezel Ozan River; according to fluvial anomalies from the entrenched section and discuss their implications.

There are some surface and subsurface faults and folds in the study area. In this paper, we have attempted to understand the surface deformation pattern along the surface and subsurface faults and folds with the help of geomorphological anomalies and fluvial processes.

The geomorphology provides the situation to identify active and potential hazardous faults. We apply this opportunity through the use of digital elevation models. Our observations demonstrate the potential for using drainage basins as tectonic markers in the quantification of uplift, which may have wider applicability in other deforming parts of the world.

We propose a general model of fluvial anomalies in the study area in which the detection of these features can lead to the identification of the most active fault segments in the Ghezel Ozan River region. Such approach can help better constrain faults activity in long-term deformation. Such configuration is likely to occur in many datasets worldwide where fluvial anomalies are controlled by fault zones.

2. Regional setting

The study area is located in the Western Alborz zone (Figure. 1) and include the part of the Ghezel Ozan River with trend of NW-SE. Volcano-sedimentary rocks of Eocene Karaj tuff comprise most of outcrops in the area. The Western Alborz zone deforms actively due to the north–south Arabia–Eurasia convergence, and westward motion of the adjacent South Caspian relative to Iran. This zone, deforms by strain partitioning of oblique shortening onto range-parallel left-lateral strike-slip and thrust faults (Allen et al., 2003) and forms a composite orogenic belt and suffered shortening and uplift during Tertiary (Alavi, 1996). There are indication for recent uplift in the western Alborz, in the form of incised river terraces and coastal marine terraces (Berberian, 1983).

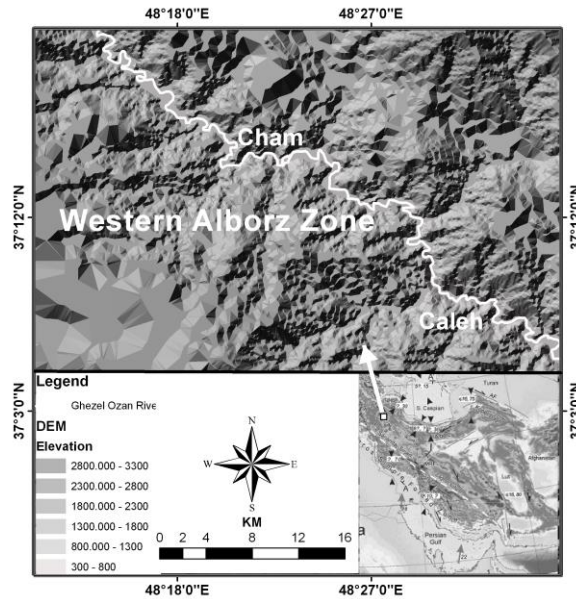


Figure 1. DEM of the study area (USGS/SRTM data) illustrating the Western Alborz structural zone in NW Iran.

3. Materials and methods

In this study, we used topographic maps at the scale of 1: 25,000, geological maps at scale of 1:100000, aeromagnetic maps at scale of 1:250000 and satellite images. Also, we have used 10-m grid cell DEM. Its projection was the UTM zone 39 N. The DEM was derived from the contour lines of the 1: 25,000 topographic maps provided by Iranian Survey Organization (ISO) with 10-m contour intervals. In order to evaluate qualitative and quantitative data for such drainage anomalies, a geographic information system (GIS) is used to manage digital elevation model (DEM).

In order to identify the role of structures in creating the fluvial anomalies, the following works were accomplished:

1- The geomorphic anomalies along the length of Ghezel Ozan River were recognized by use of Landsat ETM images with resolution of 28.5 m and by subsequent field verification.

2- The DEM were derived from the contour lines of the 1: 25,000 topographic maps provided by Iranian Survey Organization (ISO) with 10-m contour intervals. The DEM was employed for the preparation of longitudinal profiles of the Ghezel Ozan River.

3- This channel profiles provided data on river profile irregularities (knick points) that may be associated to active tectonics.

4- The whole surface structures (faults and folds) were extracted from geologic maps at scale 1:100,000 provided by the Geological Survey of Iran (GSI).

5-The whole magnetic lineaments were extracted from aeromagnetic maps at scale 1:250,000 provided by the GSI.

6- The fluvial anomalies created by surface structures, such as abnormal sinuosity and compressed meanders, were omitted and only the geomorphic anomalies related to magnetic lineaments were considered.

7- In this way, the surface and sub-surface active faults and folds in the Ghezel Ozan River basin have been recognized.

4. Results

The Ghezel Ozan River in the study area flows toward the southeast; and the length of the river in this section is 51 kilometer (Figure. 2). The geomorphic anomalies and tectonic structures in the area are shown in Figure. 3.

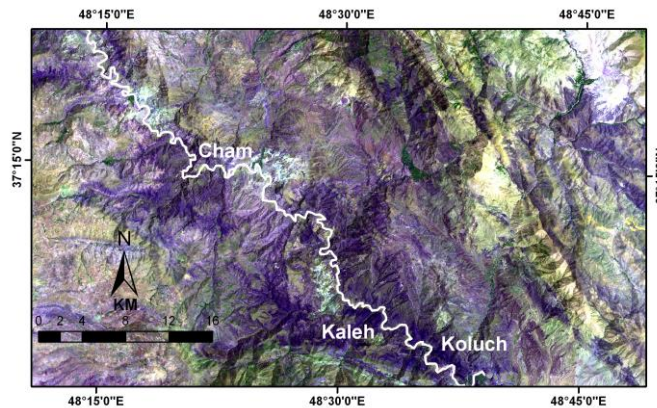


Figure 2. Annotated Landsat image depicting the situation of the Ghezel Ozan River and the key geographical regions of the study area.

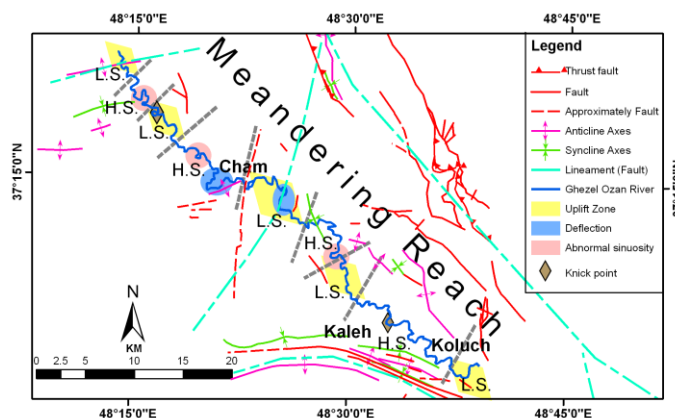


Figure 3. Structural map illustrating the role of structures in creation of fluvial anomalies in the study area. Abbreviations in this map are as follows: H.S., High Sinuosity; L.S., Low Sinuosity.

The intense and sudden deflection in the river course, the abnormal changes in the river sinuosity and knick points on the longitudinal profile of the river are recognized in the area. Deflection of the river course and abnormal changes in the river sinuosity are identified on the satellite images and approved through field observations. The knick points are specified on the longitudinal profile of the river that has been obtained from digital elevation model (DEM).

Some of the magnetic lineaments in the Ghezel Ozan River basin have caused the geomorphic anomalies along the river length. The lineaments with trend of NE - SW have created fluvial anomalies such as variations of channel pattern of the river and deflection of the river course (Figure. 3) and could be identified as active subsurface structures.

Several of the faults and folds with trend of NE - SW have created fluvial anomalies such as deflection of the river course and changes in the river sinuosity (Figure. 3) and could be identified as active surface structures. None of the knick points coincide to the lineaments or faults and folds. Therefore, it concludes that the knick points are created by other factors such as variations of lithology.

The alluvial Rivers in Himalayan basin shows similar morphological features in the uplift zone. Active tectonics in Hindu Kush has greatly influenced the drainage system and geomorphic expressions. The average of the seven measured geomorphic indices was used to evaluate the distribution of relative tectonic activity in the study area. Landsat imagery and field observations evidence the presence of active tectonics; based on the deflected streams, deformed landforms and active mountain fronts (Mahmood and Gloaguen, 2012).

5. Conclusion

This study aims to understand the different effects of tectonism on fluvial network and to interpret the tectonic deformations using described, and analysed systematic anomalies in the drainage basin of the Ghezel Ozan River. The survey influence of the structures on the rivers can detect the surface deformation pattern of the area in the surface and sub-surface faults and folds. River response to active tectonics depends upon the trend of the faults, folds and lineaments with respect to river flow. In the study area, some of the structures cut across the river channel and affect the fluvial process. The differential movements along the structures have produced longitudinal tilting in the area.

One of the most important tectonic problems in fluvial basins is the recognition of surficial deformation patterns, which are mostly produced by the action of active faults and folds in the sub-surface. In many cases, these structures are located beneath a thick sedimentary cover and their direct survey is not possible. Therefore, using fluvial anomalies we can recognize regional surface deformation patterns related to sub-surface faults and folds.

The Arabia-Eurasia collision deforms the study area, making it as one of the regions of convergent deformation on the earth. The ongoing convergence was caused both by uplift and reactivation of basement faults in the area. Active incise of river channel occurred due to the created uplift and incised river terraces. The reactivation of basement faults initiate development of fault lineaments on the sedimentary cover that were recognized on the aeromagnetic maps. These concealed structures have caused above-mentioned geomorphic anomalies in the Ghezel Ozan River basin.

Regarding the effective structures in the creation of fluvial anomalies it is specified that structures with trend of NE-SW are the most active structures in the study area. Dominance of structures with trend of NE-SW in this area (Western Alborz zone) is due to the westward movement of the Caspian Basin, which causes the oblique left lateral compression of the Western Alborz; as a result of the reactivation of deep-seated transverse basement faults. The high tectonic activity in the study area is in agreement with the seismicity of region, for example the Rudbar earthquake of June 20, 1990 ($M_S = 7.7$, $M_W = 7.3$, $m_b = 6.4$) that occurred in the vicinity of this area.

Acknowledgements

The author would like to thank the referees for their comments and recommendations.

References

- Alavi, M. (1996). Tectonostratigraphic synthesis and structural style of the Alborz mountain system in northern Iran. *Journal of Geodynamics*, 21(1), 1–33.
- Alipoor, R., Poorkermani, M., Zare, M., & El Hamdouni, R. (2011). Active tectonic assessment around Rudbar Lorestan dam site, High Zagros Belt (SW of Iran). *Geomorphology*, 128(1-2), 1–14.
- Allen, M.B., Ghasemi, M.R., Shahrabi, M., & Qorashi, M. (2003). Accommodation of late Cenozoic oblique shortening in the Alborz range, northern Iran. *Journal of structural geology*, 25(5), 659-672.
- Allen, M., Jackson, J., & Walker, R. (2004). Late Cenozoic reorganization of the Arabia-Eurasia collision and the comparison of short-term and long-term deformation rates. *Tectonics*, 23(2). doi: 10.1029/2003 TC001530.
- Berberian, M. (1983). The southern Caspian: a compressional depression floored by a trapped, modified oceanic crust. *Canadian Journal of Earth Sciences*, 20(2), 163–183.
- Cheng, W., Wang, N., Zhao, M., & Zhao, S. (2016). Relative tectonics and debris flow hazards in the Beijing mountain area from DEM-derived geomorphic indices and drainage analysis. *Geomorphology*, 257, 134–142.
- Dehbozorgi, M., Pourkermani, M., Arian, M., Matkan, A. A., Motamedi, H., & Hosseiniasl, A. (2010). Quantitative analysis of relative tectonic activity in the Sarvestan area, central Zagros, Iran. *Geomorphology*, 121(3-4), 329–341.

- Demoulin, A., Beckers, A., & Hubert-Ferrari, A. (2015). Patterns of Quaternary uplift of the Corinth rift southern border (N. Peloponnese, Greece) revealed by fluvial landscape morphometry. *Geomorphology*, 246, 188–204.
- Giaconia, F., Booth-Rea, G., Martínez-Martínez, J.M., Azañón, J.M., Pérez-Peña, J.V., Pérez-Romero, J., & Villegas, I. (2012). Geomorphic evidence of active tectonics in the Sierra Alhamilla (eastern Betics, SE Spain). *Geomorphology*, 145, 90-106.
- Gao, M., Zeilinger, G., Xu, X., Wang, Q., & Hao, M. (2013). DEM and GIS analysis of geomorphic indices for evaluating recent uplift of the northeastern margin of the Tibetan Plateau, China. *Geomorphology*, 190, 61–72.
- Jackson, J., Priestley, K., Allen, M., & Berberian, M. (2002). Active tectonics of the South Caspian Basin. *Geophysical Journal International*, 148(2), 214–245.
- Mahmood, S.A., & Gloaguen, R. (2012). Appraisal of active tectonics in Hindu Kush: Insights from DEM derived geomorphic indices and drainage analysis. *Geoscience Frontiers*, 3(4), 407–428.
- Pedrerá, A., Pérez-Peña, J.V., Galindo-Zaldivar, J., Azañón, J.M., & Azor, A. (2009). Testing the sensitivity of geomorphic indices in areas of low-rate active folding (eastern Betic Cordillera, Spain). *Geomorphology*, 105(3-4), 218–231.
- Pérez-Peña, J.V., Azor, A., Azañón, J.M., & Keller, E.A. (2010). Active tectonics in the Sierra Nevada (Betic Cordillera, SE Spain): Insights from geomorphic indexes and drainage pattern analysis. *Geomorphology*, 119(1-2), 74–87.
- Pirasteh, S. (2018). Improving Tectonic Geomorphology Analysis and Interpretation of River Mobility Utilizing LiDAR-derived DEMs. *Trends in Civil Engineering and Material Science*, 1(5), 1-9.
- Ritz, J. F., Avagyan, A., Mkrtychyan, M., Nazari, H., Blard, P. H., Karakhanian, A., Philip, H., Balescu, S., Mahan, S., Huot, S., Münch, P., & Lamothe M. (2016). Active tectonics within the NW and SE extensions of the Pambak-Sevan-Syunik fault: Implications for the present geodynamics of Armenia. *Quaternary International*, 395, 61-78.
- Sarp, G., & Duzgun, S. (2012). Spatial analysis of morphometric indices: the case of Bolu pull-apart basin, western section of North Anatolian Fault System, Turkey. *Geodinamica Acta*, 25(1-2), 86–95.
- Sarp, G. (2014). Evolution of neotectonic activity of East Anatolian Fault System (EAFS) in Bingol pull-apart basin, based on fractal dimension and morphometric indices. *Journal of Asian Earth Sciences*, 88, 168–177.

Investigation of Urban Biophysical Compounds in the Formation of Thermal Islands Using RS and GIS (Case Study: Yazd)

Sedigheh Emami^{a*}, esmail Emami^b

^a*Ms in GIS, remote sensing, Yazd Branch, Islamic Azad University, Yazd, Iran*

^b*Graduate student University of electric power systems of the Islamic trends free khomeynishahr*

Received 2 December 2017; revised 1 June 2018; accepted 3 June 2018

Abstract

The urban thermal island phenomenon has intensified in recent years, due to the changes in urban airspace along with the rise of urbanization. Spatial-temporal patterns of biophysical constituents, which include vegetation, impermeable surfaces and soil type in the city, have a significant impact on urban thermal islands. The purpose of this study is to investigate the role of effective urban parameters in the formation and clustering of Yazd urban thermal islands. In order to achieve the proposed goal, the thermal map was developed using the single-window algorithm on the thermal band of OLT sensor of Landsat ETM+ sensors for August, 2015 and 2017; Land surface temperature (LST) was calculated and using spatial correlation (LISA), hot and cold clusters of thermal islands of Yazd were extracted. In order to evaluate the surface temperature, with the intensity of LST, spatial heterogeneity of the clusters increases nonlinearly. The relationship between the thermal islands with NDVI and urban carrion layers were investigated: cold clusters are around the places with more green space and hot clusters are in the arid areas and in areas without vegetation cover. The result of the correlation between the surface temperature and the NDVI, NDBI, and NDBaI indicated that the relationship between NDVI and LST is negative, and the relationship between NDBaI and LST is also nonlinear and negative. But the relationship between NDBI and LST is nonlinear and positive. A spatial correlation

* Corresponding author. Tel: +98-9166225978.

E-mail address: s.emami061@gmail.com.

with the local index has emphasized on the extent of thermal islands in the studied periods.

Keywords: Urban thermal islands; Ahwaz city; Local spatial correlation index (LISA)

1. Introduction

Urban thermal islands are the phenomenon in which the temperature of urban areas, in comparison with the surrounding area (rural), is evident. This urban phenomenon has intensified due to the change in airspace and with increasing urbanization (Vogt & Oke, 2003; Song & Wu, 2016). Accordingly, humanized activities in urban areas lead to the release of enormous amounts of energy, and this is a major contributor to the climate change of the regions associated with the transformation of energy exchange (Yuna & Bauer, 2007). The importance of urban thermal islands made the researchers and thinkers of the environmental and urban sciences have different definitions and categories of this phenomenon. In one of the divisions, which Voogt and Oke (2003) have the most important and cited partings of this urban phenomenon, urban thermal islands are three categories:

1. Coating layer of thermal islands. (CLHI) 2. Frontal Layer of Thermal Isles. (BLHI) 3. Level of urban thermal island. (SUHI). From the first two groups, Teuton was named "Air Separation Thermal", which is most often assessed using air temperature records collected from weather stations. While SUHI is recovered more often through surface temperature (LST) and is viewed from remote sensing satellites, it is usually observed with high precision and universal spatial coverage and low cost compared to data collected through water ponds and weather forecasting are very popular. On the other hand, this technology is able to more clearly demonstrate the spatial and metamorphic patterns of urban thermal islands, which reveals the role of biophysical parameters in the formation and management of urban thermal islands (Li et al., 2011; Weng, 2012). As it was said, today remote sensing is an effective tool for understanding urban environments, because with its unique capabilities (repeating images taken from a region), maps with multiple spatial spaces are made available to the public and the curtains Has found many problems at the micro level (urban level) (Yuan & Bauer, 2007). Remote Sensing Services does not end there. In particular, the US Geological Survey (USGS) developed the National Land Use Land Cover with the help of TM ETM + imaging sensors. which contributed greatly to thematic interpretation Coverage of land and land use. Since the traditional land cover classification methods failed to meet the growing need for urban studies, analyzes were developed at sub-pixel levels (Deng & Wu, 2012). This method is known from urban studies in the literature of (Vegetation-Impervious surface-soil) or vegetation - impermeable - soil. Under this conceptual framework, types of land cover (except water) in urban environments can be considered as a combination. The city's biophysical concept consists of three basic parts:

vegetation, impenetrable surface and soil. Accordingly, two groups of different methods have been developed to determine the quantity of urban biophysical compounds: the first group includes methods for learning machine learning: such as the neural network (Mohapatra & Wu, 2008; Pu et al., 2008) Regression and decision tree (Lu & Weng, 2009; Mohapatra & Wu, 2010) and regression models

(Yang & Liu, 2005; Yang, 2006). In this method, information derived from spatial and spatial features extracted from remote sensing methods is illustrated with an experimental relationship. The second group consists of separating spectral techniques (Small, 2005; Powell et al., 2008; Weng, 2012). The basic assumption of the present method is that each cell is a combination of several homogeneous sample spectra that the spatial fragmentation coverage of each of the components of the earth can be attributed to the spectral mixture analysis. Previous studies on the relationship between the behavior and prospects of urban thermal islands indicate that the composition and configuration of land cover and its uses in this regard are important from studies (Connors et al., 2013). Global studies in this area show that the processing of remote sensing data at urban levels has been increasing dramatically in recent years. Cao et al., (2010) evaluated the intensity of the Urban Cooling Island in urban urban parks in Japan using ASTER, IKONOS data. The results of the athletic research in 92 parks in Nagoya showed that the cooling effect is dependent on the size and seasonal seasonal conditions of the park, and the park's size is non-linear to the cooling of its surroundings. Buyantuyev & Wu (2010) investigated the relationship between temporal variations of ground-level temperature with land cover and social and economic patterns in the Sonoran Desert in northern Aryrana. They studied two pairs of images of the day and night in the middle of the year (June) and the semi-cold of the year (October). Their research results showed a significant

difference in temperature, due to the high role of vegetation loss. Also Finally, using geographic weighted regression, social and economic spatial relationships were assessed with surface temperature, which indicated the positive role of human factors in the formation of thermal islands. The study of the effect of urban biophysical constituents on surface temperatures in the city of Wisconsin, including Washington, Ozaki, Milwaukee and Wakkushah, is a study by Deng and Woo (2013). In this study, they studied the level of the urban thermal islands (SUHI) in the areas mentioned, and concluded that moisture in the soil (wet and dry) had important implications for the SUHI modeling. Although the Deng and Wu study presented valuable results in modeling the surface of the island's thermal island (SUHI), it failed to address urban biophysical compositions in modeling clusters of urban thermal islands. A research that can address the deficiencies and explore a new method while designing research strengths, Guo et al. (2015) is located in Guangzhou, Guangdong Province, China. In this study, Numerical Analysis of NDVI, NDBI, NDBaI indices in this study, using spatial correlation index (LISA), extracted clusters of urban thermal islets. And concluded that the NDVI and NDBI indices had the most impact on urban thermal island clusters. A survey of the biophysical impact on the urban thermal

island, conducted by Song & We (2016) in Wisconsin, USA. The overall result of this study is the unimaginable role of impermeable surfaces in the thermal island diversity of urban areas. Among the studies carried out in Iran, Ahmadi et al. (2012) have been investigating the temporal-temporal variations of thermal patterns in Shiraz. Their results, based on TM image processing and ETM +, showed that the temperature rings of Shiraz conform to the polluted and high-traffic areas of the city and the coldest areas are also consistent with vegetation. Spatial analysis of Shiraz's temperature during the warm and cold season with an emphasis on statistical and satellite processing is also a research that Ahmadi et al. (2015) have focused on. The output of this study showed that in the warm season, the lowest temperature thresholds were consistent with vegetation, but in the cold season, the northern and northwest regions, which dominated the new settlements and the northwest highlands, which dominated the new settlements and altitudes The northern part of the city has been matched. Considering that documentary research has not been conducted with the approach of urban biophysical combinations and the spatial correlation index, the present research has focused on this issue. To this end, we will propose strategies to prevent the spread of thermal islands in Yazd.

2. Materials and Methods

2.1. Area of study

Yazd is located at 31° and $55'$ north, 54° and $20'$ east. The height of Yazd is 1218 meters above sea level. Yazd is located in the dry and semi-dry belt of the Northern Hemisphere. Yazd city is located in a wide, dry and enclosed valley between Shirkouh and Kharanag mountains. (figure 1)

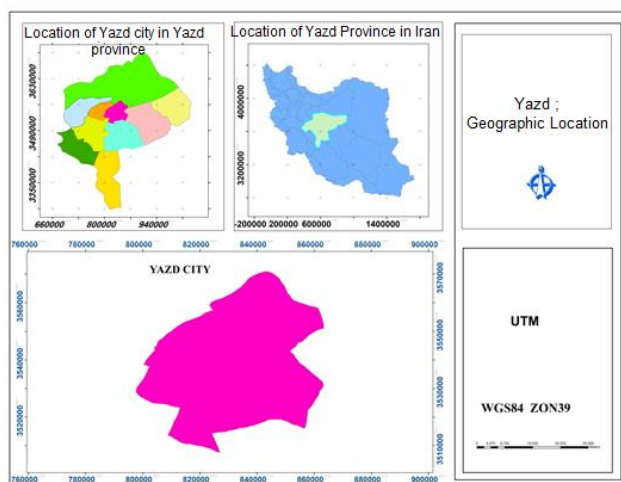


figure 1. Area of study

2.2. Materials

This research is an analytical method. But it should be added in terms of purpose. In the applied dimension, the results can be used in decision making and planning. To extract the surface temperature of the city of Yazd, the data from the thermal images of the ETM + Landsat satellite is used. One of the most important analytical steps in this study is to convert the digital value of the image to spectral radiance (Chander and Groeneveld, 2009). The steps for estimating the surface temperature are as follows, which will be explained below: 1. Convert the digital value of the image to the spectral radiance; 2. Convert the spectral radiance to the brightness temperature. 3 Conversion of light temperature to kinetic temperature (Chander & Markhan, 2003). In the third step, the correction of the earth surface temperature emission for the conversion of light temperature to kinetic temperature was calculated according to the equations of Li et al. (2011) and Sobrino et al. (2004). To assess the vegetation situation, some indicators have been proposed, the most common and most accurate of which are the NDVI index (Atzberger, 2013), and the capabilities of this indicator were used in this study. Also, in order to evaluate other urban biophysical parameters, the Normalized Difference Build-up Index (NDBI) Normalized Difference Bareness Index (NDBaI) We got.

In this study, the land surface temperature evaluation process using Landsat 8 satellite images was presented in MATLAB software in three stages including preprocessing of image, calculating ground temperature and estimating frequency of plant using spectral composition linear analysis.

Step 1 (Preprocessing the image): This study should be performed on triangles 4, 5 and 10 on non-cloudy days. At this stage, geometric and atmospheric corrections are usually done to accurately calculate the surface temperature of the earth.

Step 2 (calculating ground temperature): The researchers were able to find a meaningful relationship between these factors by examining different light spectra and reflecting them at different temperatures and reflection of phenomena. In this regard, it is possible to use the Landsat 10, which is a thermal infrared image.

In fact, this reflects the thermal reflection of phenomena as a black body. In order to find the surface temperature, the temperature of the satellite or the temperature of the black body must first be obtained and then, with the two methods mentioned above, the surface temperature of the earth can be calculated. Calculation of satellite effective temperature: At this stage, digital numbers are first converted into spectral sensors using Equation (1).

$$(1) \quad L_{\lambda} = \frac{(L_{\max} - L_{\min}) \times DN}{2 \times 5} + \text{offset}$$

The L_{\max} , L_{\min} and offset values are extracted using metadata. Then, the satellite effective temperature at this stage will be obtained from equation (2):

$$(2) \quad T_s = \frac{T_s}{\ln(K_1/L_\lambda + 1)}$$

In this equation, T_s is the effective temperature of the satellite or the illumination temperature of the sensor. K_1 and K_2 are correction coefficients that have values of 666.09 and 1287.71 respectively (for Landsat images). The temperature of this stage is also known as black body temperature.

Calculation of ground surface temperature: Two methods can be used to calculate ground surface temperature.

The single-window algorithm was developed to provide surface temperature image of the earth. Although atmospheric correction still needed. This algorithm requires three parameters: the emissivity, transmission and atmosphericity. The average atmospheric temperature of the single-window algorithm are calculated using equation (3) (Yang & Liu, 2005).

$$(3) \quad T = \frac{1}{C[a(1 - C - D) + (b(1 - C - D) + C + D)T_s - DT_a]}$$

In this equation, T_s is the effective temperature of the satellite and T_a is the average atmospheric temperature that can be obtained by a simple equation with near-surface temperature (T_a). The coefficients a and b have a value of -67/355351 and 0/458606, respectively. Also, C and D are derived in equations 4 and 5.

$$(4) \quad C = t\varepsilon$$

$$(5) \quad D = (1 - t) [1 + (1 - \varepsilon) t]$$

In these equations, t is an atmospheric transition that can be estimated using near-surface temperature and water vapor data as well as meteorological observations of the area. Based on the findings, there is always a linear relationship between t and water vapor (Zhang et al, 2007).

The t -value and the average atmospheric temperature can be estimated according to Qin studies (Qin et al., 2003 and 2001). In fact, each of the land leakage has a certain specific flux determined by their Snyder study (Snyder, 1998). With the detection of a minimum NDVI for coated areas and a maximum NDVI for areas with a dry soil, a range for NDVI was obtained in other areas. If we accept that the plants have a greater reflection in the infrared band than the red band, then NDVI for plants will always be positive. Therefore, identification of the outer soil cells can be made in NDVI smaller than or equal to zero

(SalmanMahini and Kamyab, 2009). Therefore, with the average of soil irradiance and vegetation cover, we can calculate the dissipation of other areas from Equation (6):

$$(6) \quad \varepsilon = \varepsilon_v PV + \varepsilon_s (1 - \varepsilon_v) + d\varepsilon$$

In this equation, Emissivity are areas with a full coverage and areas with a dry soil. Also, calculating the effect of surface distribution is possible using Equation (7).

$$(7) \quad D\varepsilon = (1 - \varepsilon_s) (1 - F) \varepsilon_v$$

F is a form factor in this equation whose mean value based on different geometric distribution is 0.55. Also, the percentage of vegetation cover can be obtained from Eq. (8).

$$(8) \quad PV = \left[\frac{NDVI - NDVI_{min}}{NDVI_{max} - NDVI_{min}} \right]^2$$

Corrected ground temperature: In this method, the ground surface temperature is obtained from Equation (9) in terms of Kelvin (Artis & Carnahan, 1982)

$$(9) \quad T = \frac{T_s}{1 + \left(\lambda \times \frac{T_s}{(P)I_n\varepsilon} \right)}$$

In this regard, the wavelength of the radiation radiated is 11.5 μm .

Also, $(1.438 \times 10^{-2} \text{ Km}) p = hc / \sigma, j / \text{K}$ is Boltzmann's constant, h is the Planck constant, and equal to 6.626×10^{-34} and c is the light speed with $2.998 \times 10^8 \text{ m / s}$.

2.3. Preparing indicators maps

Stage 3 (calculating ground temperature and estimating frequency of plant using spectral composition linear analysis (P8) (P LSMA)): Rid (1995) used the V-I-S model to parametrized the urban biophysical composition.

This model was later used in many studies due to its valuable results from the description of urban composition and dynamics (Yang & Liu, 2005).

The V-I-S model is used with NDVI, NDIs and NDBAIs for urban land classification (Weng et al, 2004). By providing these three images, we can better understand a combination of city users.

There are significant variations in the spectra of each floor covering. After normalizing, the amount of light shifts can be eliminated or reduced, although much information will be

reduced. The normal reflection of each bond is obtained by using equation (11) (Yang & Liu, 2005).

The NDBI¹ index is calculated using the following equation. This indicator indicates the built areas.

$$(10) \quad \text{NDBI} = \frac{\text{SWIRI} - \text{NIR}}{\text{SWIRI} + \text{NIR}}$$

Preparing NDBaI² Map for Yazd City:

Using the following equation, the NDBaI is calculated. This indicator indicates the arid areas.

$$(11) \quad \text{NDBaI} = \frac{\text{SWIRI} - \text{TIRSI}}{\text{SWIRI} + \text{TIRSI}}$$

In the above relationships, SWIR represents the infrared wavelength band and the TIRS is thermal band.

Preparing NDVI Map for Yazd City:

This index was calculated in the field emission calculations. NDVI represents the vegetation cover.

After calculating the ground surface temperature with single-window and NDVI-Emissivity algorithms and NDBI indices, NDBaI, using MATLAB software, selects 3,017 dots randomly in images obtained from NDBI, NDBaI, NDVI indices, and surface temperature. Extract image information in selected points with Extract by value to point, in ArcGIS software. Then, we analyze the correlation between NDBI, NDBaI, NDVI and LST indices in SPSS software. To analyze the spatial statistics, the temperature of the surface of the earth and the thermal islands has been used from the local Moran index.

3. Results

Statistical analysis of surface temperature in Yazd city

By reviewing the data on the surface temperature of Yazd in August, the two study periods (2015 and 2017) showed that the surface temperature is decreasing (Table 1), so that the minimum temperature from 25.717601 Celsius in 2015 decreased to 18.98599 Celsius in 2017. The average temperature has dropped by 5.3 degrees Celsius, with a maximum temperature of 55.4741 degrees Celsius in 2015 to 51.2445 degrees Celsius in 2017. The maximum temperature of the studied courses has also decreased significantly. The difference between the years (2015-2017) was 4.23 degrees Celsius. In the studied period, mode in 2015 has changed dramatically, but in 2017 there is no significant difference with two statistics.

¹ - Normalized Difference Build-up Index (NDBI)

² - Normalized Difference Bareness Index (NDBaI)

Table 1. Statistical indexes of the surface temperature of Yazd

2017	2015	Statistics
3017	3017	N
41.41731805	46.711420857	Mean
.078651793	.0811714129	Std. Error of Mean
42.48099900	47.745998000	Median
43.254902	51.8032990	Mode
4.320124725	4.4585204236	Std. Deviation
18.663	19.878	Variance
-1.226	-1.156	Skewness
.045	.045	Std. Error of Skewness
1.886	1.585	Kurtosis
.089	.089	Std. Error of Kurtosis
29.900401	28.2581000	Range
18.98599	25.717601	Minimum
51.2445	55.4741	Maximum
124956.048549	140928.3567250	Sum

Spatial relationships modeling

This tool model the relationships between variables that are related to geographic complications and allow us to predict the values of unknown variables and better understand the factors that affect a variable. Regression methods allow us to examine relationships between variables and measure the severity and weakness of those relationships.

Space relationship analysis tool

Geographic weighted regression: Geographical weight regression is local model of the variable or process that you are trying to understand. Geographic weighted regressions do this by providing separate regression equations for each complication by considering dependent and independent variables that are complicated throughout the band (range).

Geographic weighted regression is a technique used for descriptive analyzes of spatial statistics. The equation is written as follows (Rezaei, 2017)

$$(12) \quad YI = \beta_0 + \beta_1 X_1 + \varepsilon$$

In this equation, y is a dependent variable, β is the coefficient of correlation, X is independent variable and ε is random error.

Correlation coefficients

One of the basic definitions in the science of statistics is the definition of correlation and the relationship between the two variables. In general, we define the correlation as the severity of the dependence of the two variables on each other. There are many types of different correlation coefficients that each measure the correlation between the two variables according to the type of data and the conditions of the variables. In general, the correlation coefficients vary between -1 and +1, and the relationship between the two variables can be positive or negative. Correlation coefficient is a reciprocal relationship, the more correlation coefficient is closer, the greater the degree of dependence of the two variables.

Pearson correlation coefficient

This correlation coefficient is based on covariance of two variables and their standard deviations, which can be used to calculate the Pearson correlation coefficient.

$$(13) \quad r_{xy} = \frac{cov(x, y)}{\sigma_x \sigma_y}$$

Table 2. Pearson correlation coefficient between land surface temperature (LST) and NDBAI, NDVI, NDBI

Pearson Correlation	LST	NDVI	NDBAI	NDBI
LST	1	-.230**	-.525**	.232**
NDVI	-.230**	1	.111**	-.235**
NDBAI	-.525**	.111**	1	.020
NDBI	.232**	-.235**	.020	1

** . Correlation is significant at the 0.01 level (2-tailed).

In this study, the relationships between NDVI and LST were negative, since the distribution of these two parameters in the city did not have a uniform dispersion. A strong and negative relationship occurs between two parameters when the city or its surface has one-handed cover or it has a gradual decrease. The results of the evaluation of the temperature are a good confirmation that the relationship between NDVI and LST, or between NDBI and LST, is not necessarily linear or non-linear. The relationship between NDBAI and LST is also negative. But NDBI and LST have a positive relationship. (Figure2)

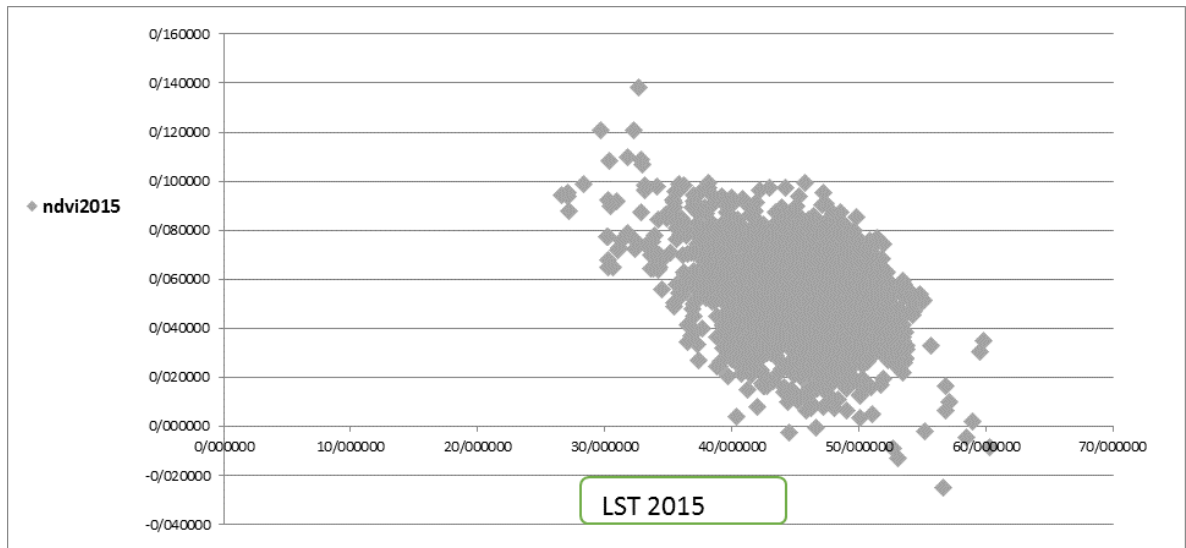


Figure2.A. The relationship between LST and NDVI in 2015

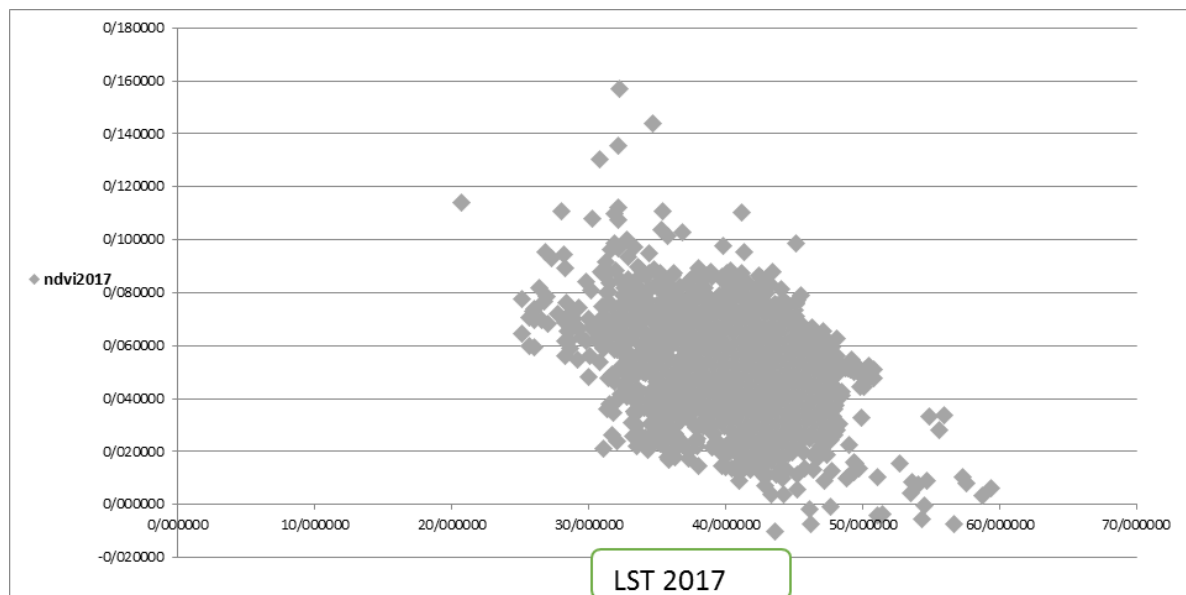


Figure2. B. The relationship between LST and NDVI in 2017

The temperature range for August 2015 and 2017 on (Figure 3) shows a fundamental change in ground temperature for a minimum and a maximum. The lowest temperature in 2015 is 25.71 degrees Celsius and in 2017 it is 18.98 degrees Celsius. The maximum temperature in 2015 is 55.47 degrees Celsius and in 2017 it is 51.24 degrees Celsius. Minimum temperature is shown with cream color and maximum temperature with blue.

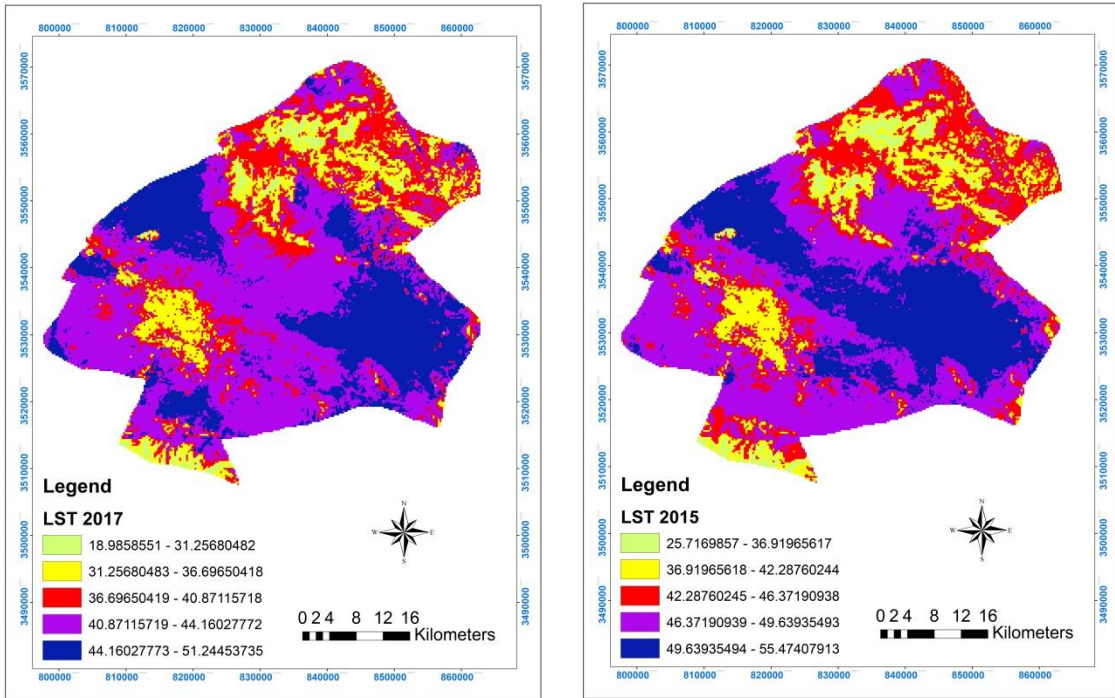


Figure3. Land surface temperature (2017 and 2015)

The comparison of the temperature with the vegetation shows that the hot spots are in the arid areas and the areas without vegetation. They are marked with red dots, and cold spots are marked with green dots (Figure. 4).

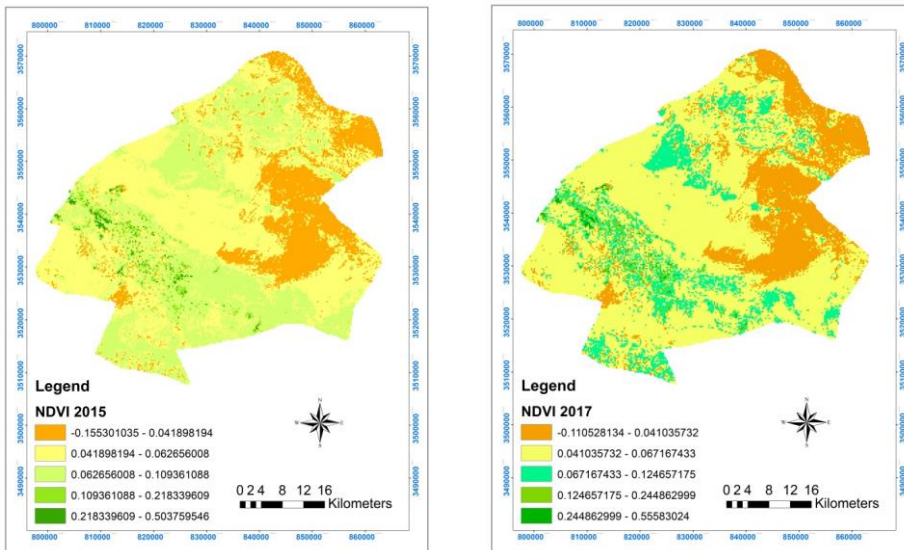
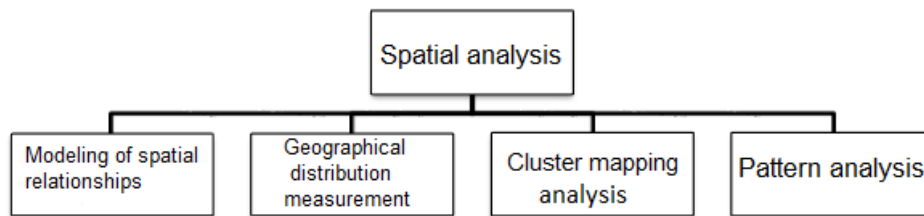


Figure4. Vegetation (2015 and 2017)

Spatial statistics in the ArcGIS environment

This analysis is based on spatial data and its basic function is to obtain information that is necessary so that planners move towards statistical-graphing of locational data. Perhaps the misconception about GIS is that the GIS is a kind of software. It is not true because the GIS is considered as a powerful system for planning and specialized software is used for it (Rezaei, 2017).

To carry out spatial analysis, four important and practical parts for implementing spatial variations that include relevant steps will be given.



Pattern analysis

To investigate the spatial pattern of data, we can use the Moran index to determine the quantity and test the spatial structure. The Moran index examines autocorrelation based on the location of the two values and analyzes the geographical condition in that location (Griffith, 1987). In order to calculate the Moran index, the z and p-value scores are firstly calculated, and in the next step, the evaluation and significance of the index are examined (Fisher and Gates, 2009). ArcGIS 10.3 software has been used to calculate spatial autocorrelation using the Global Moran index. If the Moran index is close to +1, the data are spatial autocorrelation and cluster pattern and if the Moran index is close to -1, the data are dispersed.

Cluster mapping analysis

If we have a set of weighting effects, this tool identifies clusters of points with similar and different values of size. Creating a map of clusters, especially when it comes to the location of one or more clusters, is very useful. Unlike methods and tools that show trends and general patterns and produce figures and statistics, cluster mapping tools allow us to visualize clusters (Rezaei, 2017).

Analysis of hot and cold clusters

If we have a set of weighting effects, this tool identifies the clusters of complications with high amounts (hot clusters) and clusters of complications with low amounts (cold clusters).

Analysis of hot and cold clusters of urban thermal islands has been used from the local Moran index. This index classifies the temperature values of the earth's surface in the form

of a warm / cold cluster in places close to each other and most closely resembling it (Anslin et al., 2006). Therefore, this study was used to determine the clusters of urban thermal islands, after obtaining the temperature of the surface of the earth.

The cluster revealed by this method has revealed the relationship between urban thermal islands and urban biophysical compounds on a city scale. The local Moran is calculated from the following equation.

$$I_i = n \times \frac{(x_i - \bar{x})}{\sum_i (x_i - \bar{x})^2} \times \sum_j w_{ij}(x_i - \bar{x}) = \frac{z_i}{m_0} \times \sum_j w_{ij}z_j, \quad \text{with: } m_0 = \sum_i \frac{z_i}{n},$$

(14)

In the above equation, X_i is the property of i , X is the average of the desired property and W_{ij} is the spatial weight between the i and j components. The points generated by this statistic, along with the significance of local Moran, produce four categories of distribution of dispersion, which a user and scientific scholar can use to determine their spatial correlation type of their data. These four categories of information are as follows:

Hot thermal islands (HH): This type of thermal islands represents areas where the surface temperature of earth (LST) is much higher than the average surface area of the entire area.

Cold thermal islands (LL): This type of thermal islands represents areas where the surface temperature of earth is lower than the average of the entire area.

Hot thermal islands near cold thermal islands (HL): This type of thermal islands represents areas where the surface temperature of earth is high, while the temperature of adjacent regions is lower than the average of the entire area.

Cold thermal islands near warm thermal islands (LH): This type of thermal islands represents areas where the surface temperature of earth is low, while the temperature of adjacent regions is higher than the average of the entire area.

In addition to the four types of thermal islands, the output of this function may have a fifth type, which is briefly depicted NS (meaningless). Areas with such a degree actually show that there was no significant local connection at the surface temperature of that area.

This tool also detects spatial clusters. To do this, this tool calculates the local Moran value, Z score, P value and a code that indicates the type of cluster for each complication. The Z score and P value represent a significant amount of calculated index (Rezaei, 2017).

Geographic distribution measurements

. Spatial autocorrelation of surface temperature in Yazd city (Global Moran Index)

Autocorrelation relates to the relationship of residual values along the regression line. Autocorrelation is based on the first law of geography and randomness (random). This tool, in fact, specifies the Moran index. The Moran statistic is expressed using a correlation coefficient, and its orbit varies between +1 and -1. So that if its value moves to +1, it shows a high and concentrated cluster pattern in most of the studied area. If it moves to -1, it will represent a dispersed pattern on the geographic side. If Moran is close to zero, that is, autocorrelation does not exist and this indicates a random and non-significant pattern at the desired level of confidence (Ahmadi, Dadashiroudbari, 2016).

$$-1 < \text{Moran} < +1$$

In order to evaluate spatial autocorrelation, surface temperature data of Ahwaz with a spatial scale of 30 meters was used. Table 3 shows the global Moran autocorrelation values for the Earth's surface temperature. Based on table (3), surface temperature in Yazd has a positive spatial autocorrelation in all studied years. We conclude that the surface temperature data of Yazd have a space structure and are distributed in the form of a cluster. According to Table 4, the temperature distribution pattern of Yazd is in a hot-hot cluster pattern.

Table 3. The output of Moran statistics for Yazd city

Global Moran's I Summary	2017	2016	2015
Moran's Index:	0.79	0.85	0.83
Expected Index:	-0.0003	-0.0003	-0.00
Variance	0.0002	0.0002	0.0002
z-score	51.53	55.20	53.57
p-value	0.00	0.000	0.00

Table 4. Temporal distribution pattern of the region

Distribution pattern type	P-value	z-score	Number
Strong cluster - cold – cold	0.01	-2.58>	1
Medium cluster - cold – cold	0.05	(1.96-)-2.58-	2
Weak cluster - cold – cold	0.1	(1.65-) - 1.96-	3
Random - Distorted Distribution	1.65 - 1.65 -	4
Weak cluster - hot – hot	1.65	1.96-	5
Medium cluster - hot – hot	0.05	2.58-1.96	6
Strong Cluster - Hot – Hot	0.01	2.58<	7

. Local Indicator of Spatial Coherence

As discussed earlier, the Global Moran Space Autocorrelation function specifies only the type of surface temperature pattern. For this reason, to show the spatial distribution of the governing pattern of the thermal islands of Yazd and its clustering during the studied period, the local correlation is used. In this statistic, HH represents clusters of high surface temperature values (positive spatial correlation at 99% confidence level), LL denotes clusters of low surface temperature values (negative spatial correlation at 99% confidence level). On this basis, as shown in Table (6), the cluster of thermal warming is 12,600 meters in 2015 and 14,670 meters in 2017, and finally 27,270 meters in area of Yazd city. The cold thermal islands also have 14850 meters in 2015 and 15720 meters in 2017 from the city's atmosphere. Areas lacking an autocorrelation pattern are also presented in Table 6. These regions explain urban biophysics in the formation of thermal islands because of the high changes in the surface temperature in the findings and its high contrast in the city of Yazd. In fact, this function only reveals the thermal islands that are most likely to focus and cluster in space.

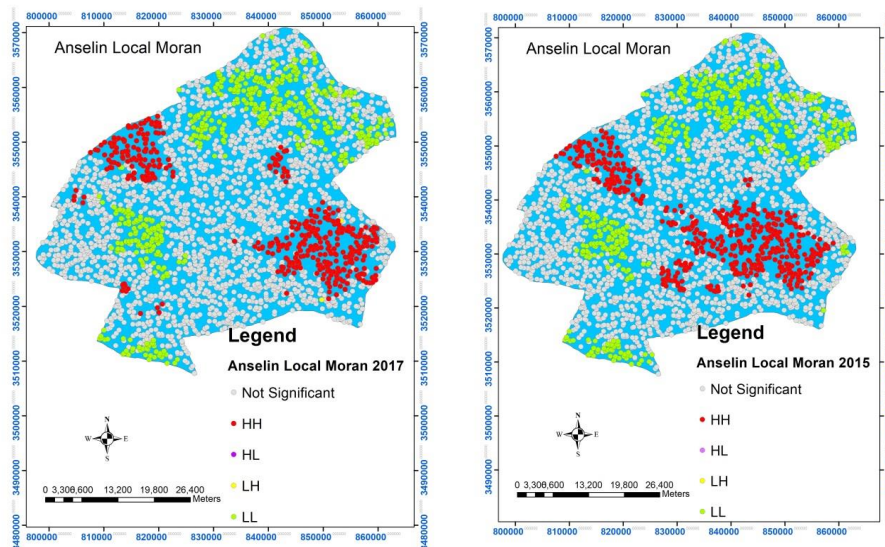


Figure5. The Moran index of Yazd in 2015 and 2017

Table 5. Area under thermal island cluster coverage (m)

Pattern type	2015	2017
Hot thermal islands (HH)	12600	14850
Cold thermal islands (LL)	14670	15720
No significant pattern (NS)	63150	59910

. Spatial Relations Modeling

Multiple regression

The correlation coefficient (R^2) in 2015 between the variables is 0.595, which indicates that there is a relatively high correlation between the variables. Also, the adjusted R Square value of 0.593 indicates that 59 percent of the total temperature variation in Yazd is dependent on these three variables used in this equation.

The regression equation of 2015:

$$(15) \quad \text{Lst}_{2015} = 46.86 - 19.76 * \text{NDVI} - 13.98 * \text{NDBai} + 25.09 * \text{NDBi}$$

The correlation coefficient (R^2) in 2017 between variables is 0.582, which shows that there is a relatively good correlation between the variables. Also, the Adjusted R Square value of 0.574 indicates that 57 percent of the total temperature variation in Yazd is dependent on these three variables used in this equation.

The regression equation of 2017:

$$(16) \quad \text{Lst}_{2017} = 41.66 - 18.71 * \text{NDVI} - 13.56 * \text{NDBai} + 22.09 * \text{NDBi}$$

4. Conclusion and Discussion

Earth surface temperature plays a crucial role in the exchange and interaction of energy flux between the surface and the air, so understanding the link between LST and the features of the urban surface is critical to designing effective measures to reduce the thermal island range.

This study was carried out with an innovative and object oriented approach using spatial correlation index with the aim of studying the effects of urban biophysical parameters on the formation and clustering of urban thermal islets of Yazd. For this purpose, OLS sensor images of Landsat 8 were received in August 2015 and 2017 from the US Earth Science Foundation (USGS), and the surface temperature of each of the images was calculated for the Yazd area. In the next step, three indicators of NDVI, NDBI, and NDBai were calculated and their results were studied to evaluate the biophysical combinations of Yazd.

The results indicate that the two NDVI and NDBi indices have a significant correlation with LST, so that the NDVI index has a negative effect on LST and, conversely, NDBi has a positive effect. It was found that two NDBai and NDVI indices are good indicators for studying urban thermal islands.

In this study, it was found that the distribution of NDVI and LST clearly revealed both warm and cold edges in Yazd. In such a way that the relations between these two parameters in the city do not have a uniform dispersion. The strong negative relationship between these two parameters occurs when the city or surface of it has a uniform coverage or gradual decrease, which is another claim for the structural interaction of city thermal islands.

The results of the spatial autocorrelation of the global Moran show that the temperature data of the Yazd has a structured pattern and is distributed in the form of strong hot-hot

clusters. That is, high temperatures and low temperatures tend to be concentrated or clustered in space.

The results of clustering the urban thermal islands with local Moran function showed that in the course of time, the size of warm thermal islands has been increased and consequently the size of the cold islands has also been increased. The changes in the earth surface temperature of Yazd have contributed to the disappearance the order of clustering of the thermal islands, but the extent of areas with such a statistical characteristic (lacking statistical significance) has been reduced. As noted, based on the type of urban management features, the results of this research in the area of helping urban planners to reduce the effects of Yazd urban thermal islands is clear.

A comparison of the results of this study with the research carried out by Wang (2012) and Yang and Baer (2007) showed that Heat has a positive relationship with the city's biophysical properties, and the temperature has a positive relationship with impenetrable surfaces and a negative relationship with the coating. There is a green plant that has a logical relation to the results of this research. Lee et al. (2011) showed that the development of urbanization has an impact ISA and NDVI have a positive effect on urban thermal islands and the relationship between distribution of LST coverage pattern indicates the direct relation of LST to Land, which is consistent with the results of this research. The study by Xiao and Modi (2005) showed that the temperature in urban areas was directly related by distributing the land cover pattern, which is consistent with the findings of this research. Comparison of the results of this study with Ahmadi et al. (2012 and 2015) and Gao et al. (2015) have shown that due to the simultaneous application of multivariate partitioning methods in order to reduce the complexity of urban space and spatial correlation function, this research has better explained the clusters of thermal islands.

References

- Ahmadi, M. And Ashoorl, d., Mandans Fred, M., 2015, Analysis of the temperature of Shiraz city in hot and cold seasons using statistical analyzes and satellite images. *Geographic Quarterly Journal*, Year 30, Issue 2, pp. 147-160.
- Ahmadi, M. And Ashoorl, d., Mandans Fred, M., 2012, Temporal and temporal variations of thermal and user patterns in Shiraz city using TM & ETM sensor data, *Remote Sensing and GIS*, 2009, 4 (4), pp. 55-68.
- Ahmadi, M. and Dasashi roudbari, A., 2016. Effects of Biophysical Compounds on the Formation of Urban Thermal island (Case Study: Mashhad), *Remote Sensing and GIS*, No. 8, autumn 2015, pp. 39-58.
- Anselin, L, Syabri, I and Kho,Y, 2006. GeoDa: An Introduction to Spatial Data Analysis, *Geographical Analysis*, 38(1), pp.2-22.

- Artis, D. A. & Carnahan, W. H. 1982. Survey of emissivity variability in thermography of urban areas. *Remote Sensing of Environment*, 12: 313–329.
- Atzberger, C., 2013, *Advances in Remote sensing of Agriculture: Context Description, Existing Operational Monitoring Systems and Major Information Needs*, *Remote Sensing*, 5(2), pp.949-981.
- Buyantuyev, A. & Wu, J., 2010, Urban Heat Islands and Landscape Heterogeneity: Linking Spatiotemporal Variation in Surface Temperatures to Land-cover and Socioeconomic Patterns, *Landscape Ecology*, 25(1), pp. 17-33.
- Cao, X., Onishi, A., Chen, J. & Imura, H., 2010, Quantifying the Coll Island Intensity of Urban Parks Using ASTER and IKONOS Data, *Landscape and Urban Planning*, 96(4), pp. 224-231.
- Chander, G. & Groeneveld, D.P., 2009, Intraannual NDVI Validation of the Landsat 5 TM Radiometric Calibration, *International Journal of, Remote Sensing*, 30(6), pp. 1621-1628.
- Chander, G. & Markham, B., 2003, Revised Landsat-5 TM Radiometric Calibration Procedures and Postcalibration Dynamic Ranges, *IEEE Transition on Geoscience and Remote Sensing*, 41(11), pp. 2674-2677.
- Connors, J.P., Galletti, C.S. & Chow, W.T., 2013, Landscape Configuration and Urban Heat Island Effects: Assessing the Relationship between Landscarpe Characteristics and Land Surface Temperature in Phoenix, Arizona, *Landscarpe Ecology*, 28(2), 271-283.
- Deng, C. & Wu, C., 2012, BCI: A Biophysical Composition Index for Remote Sensing of Urban Environment, *Remote Sensing of Environment*, 127. pp.247-259.
- Deng, C & Wu, C., 2013, Examining the Impacts of Urban Heat Island: A Spectral Unmixing and Thermal Mixing Approach, *Remote Sensing of Environment*, 131. pp.262-274.
- Fischer, M.M. & Getis, A., 2009, *Handbook of Applied Spatial Analysis: Software Tools, Methods and Applications*, Springer Science & Business Media.
- Griffith, D. A. (1987). *Spatial Autocorrelation: A Primer* (Washington, DC: Association of American Geographers). Resource Publications in Geography.
- Guo, Wu, Z., Xiao, R., Chen, Y., Liu, X., & Zhang, X., 2015, Impacts of Urban Biophysical Composition on Land Surface Temperature in Urban Heat Island Clusters, *Landscape and Urban Planning*, 135, pp.1-10.
- Li, J., Song, C., Cao, L., Zhu, F., Meng, X. & Wu, J., 2011, Impacts of Landscape structure of Shanghai, China, *Remote Sensing of Environment*, 115(12), pp.3249-3263.
- Liu L, Zhang Y. 2011. Urban Heat Island Analysis Using the Landsat TM Data and ASTER Data: A Case Study in Hong Kong. *Remote Sensing*, 3(7):1552-1535.
- Lu, D. & Weng, Q., 2009, Extraction of Urban Impervious Surfaces from an IKONOS Image, *International Journal of, Remote Sensing*, 30(5), pp. 1297-1311.

- Mohapatra, R.P.&Wu, C.,2008, Subpixel Imperviousness Estimation with IKONOS Imagery: An Artificial Neural Network Approach (pp.21-37).
- Mohapatra, R.P. & Wu, C., 2010 High Resolution Impervious Surface Estimation. *Photogrammetric Engineering & Remote Sensing*, 76(12), pp, 1329-1341.
- Powell, S.L., Cohen, W.B., Yang, Z., Pierce, I D. & Alberti, M., 2008, Quantification of Impervious Surface in the Snohomish Water Resources Inventory Area of Western Washington from 1972-2006, *Remote Sensing Environment*, 112(4), pp. 1895-1908.
- Pu, R., Gong, P., Michishita, R.& Sasagawa, T.,2008, Spectral Mixture Analysis for Mapping Abundance of Urban Surface Components from the Terra /ASTER Data, , *Remote Sensing of Environment*, 112(3), PP. 939-954.
- Qin, Z., Karnieli, A. and Berliner, p., 2001. A mono-window algorithm for retrieving land surface temperature from Landsat TM data. *International Journal of Remote Sensing*. 22(18): 3719-3746.
- Qin, Z., Li, W. & Zhang, M. 2003. Estimating of the essential atmospheric parameters of mono-window algorithm for land surface temperature retrieaval from Landsat TM6. *Remote Sensing for Land and Resources*, 56: 37-43.
- Rezaei, Akram, 2017, Extraction of the main factors affecting life in the city using spatial analysis (Case Study: Genaveh), Yazd Azad University, pp. 31-34.
- SalmanMahini, AS. And Kamyab, h. 2009 Remote sensing and GIS applications with Idrisi software. Mehr Publication
- Small, C.,2005, A Global Analysis of Urban Reflectance, *International Journal of, Remote Sensing*, 26(4), pp. 661-681.
- Snyder, W. C. 1998. Classification based emissivity for land surface temperature measurement from space. *International Journal of Remote Sensing*, 19: 2753–2774.
- Sobrino, J. A.,Jimenez-Munoz, J.C. & Paolini,L., 2004, Land Surface Temperature Retrieval Form LANDSAT TM 5 , , *Remote Sensing of Environment* , 90(4), pp. 434-440.
- Song,Y.& Wu, C.,2016,Examining the Impact of Urban Biophysical Composition and Neighboring Environment on Surface Urban Heat Island Effect, *Advances inSpace Research* ,57(1), pp.96-109.
- Vogt,J. & Ohe,T.,2003,Termal Remot Sensing of Urban Climates, *Remote sensing of Environment* , 86(3) , pp.370-384.
- Weng, Q., 2012, Remote Sensing of Impervious Surfaces in the Urban Areas:Requirements,Methods, and Trends, *Remote Sensing of Environment* , 117,pp.34-49.
- Weng, Q.; Lu, D. & Schubring, J. 2004. Estimation of land surface temperature-vegetation abundance relationship for urban heat island studies. *Remote Sensing of Environment*, 89: 467-483.

- Xiao J, Moody A. 2005. A comparison of methods for estimating fractional green vegetation cover within a desert-to-upland transition zone in central New Mexico, USA. *Remote Sensing of Environment*, 98(2-3): 237-250.
- Yang, F.& Bauer, M.E.,2007, Comparison of Impervious Surface Area and Normalized Difference Vegetation Index as Indicators of Surface Urban Heat Island Effects in Landsat Imagery, *Remote Sensing of Environment*, 106(3), pp. 375-386.
- Yang, H., & Liu, Y. (2005). A satellite remote sensing based assessment of urban heat island in Lanzhou city, northwest China. *International Archives of Photogrammetry. Netherlands: Remote Sensing and Spatial Information Sciences*.
- Yang, X, 2006, Estimating Landscape Imagery, *Geoscience and Remote Sensing Letters, IEEE*, 3(1), PP.6-9.
- Yang, X. & Liu, Z, 2005, Use of Satellite derived Landscape Imperviousness Index to Characterize Urban Spatial Growth, *Computers, Environment and Urban Systems*, 29(5), pp. 524-540.
- Zhang, J.; Li, Y. & Wang, Y. 2007. Monitoring the urban heat island and the spatial expansion: using thermal remote sensing image of ETM+ band6, viewed 20 January 2011, www.sklog.labs.gov.cn/atticle/B07/B07023.pdf
- Zhou Y, Weng Q, Gurney KR, Shuai Y, Hu X 2012. Estimation of the relationship between remotely sensed anthropogenic heat discharge and building energy use. *ISPRS Journal of Photogrammetry and Remote Sensing*, 67: 65-72.

Evaluation of super-resolution algorithm for detection and recognition of features from MODIS and OLI images at sub-pixel scale using Hopfield Neural Network

Mohammad Hosein Mehrzadeh Abarghoee^{a*}, Ali Sarkargar Ardakani^b

^a *Ms in GIS&RS, Yazd Branch, Islamic Azad University, Yazd, Iran*

^b *GIS&RS Department, Yazd Branch, Islamic Azad University, yazd, Iran*

Received 12 February 2018; revised 9 April 2018; accepted 10 June 2018

Abstract

Fuzzy classification techniques have been developed recently to estimate the class composition of image pixels, but their output provides no indication of how these classes are distributed spatially within the instantaneous field of view represented by the pixel. Super-resolution land-cover mapping is a promising technology for prediction of the spatial distribution of each land-cover class at the sub-pixel scale. This distribution is often determined based on the principle of spatial dependence and from land-cover fraction images derived with soft classification technology. As such, while the accuracy of land cover target identification has been improved using fuzzy classification, it remains for robust techniques that provide better spatial representation of land cover to be developed. An approach was adopted that used the output from a fuzzy classification to constrain a Hopfield neural network formulated as an energy minimization tool. The network converges to a minimum of an energy function. This energy minimum represents a “best guess” map of the spatial distribution of class components in each pixel. The technique was applied to remote sensing imagery (MODIS & OLI images), and the resultant maps provided an accurate and improved representation of the land covers. Low RMSE, high accuracy. By using a Hopfield neural network, more accurate measures of land cover targets can be obtained, The

* Corresponding author. Tel: +98- 3537305726.

E-mail address: hosein_mehrzade@yahoo.com.

Hopfield neural network used in this way represents a simple, robust, and efficient technique, and results suggest that it is a useful tool for identifying land cover targets from remotely sensed imagery at the sub-pixel scale. The present research purpose was evaluation of HNN algorithm efficiency for different land covers (Land, Water, Agriculture land and Vegetation) through Area Error Proportion, RMSE and Correlation coefficient parameters on MODIS & OLI images and related ranking, results of present super resolution algorithm has shown that according to precedence, most improvement in feature's recognition happened for Water, Land, Agriculture land and ad last Vegetation with RMSEs 0.044, 0.072, 0.1 and 0.108.

Keywords: Fuzzy classification, Hopfield Neural Network, Spatial resolution, Sub-pixel, Land cover, Energy function, Super resolution

1. Introduction

Since land cover information is important in the field of management and understanding the environment, extraction and characterization of the location of different land covers as accurately as possible has been a necessary process for many applications such as military, spyware, agricultural planning, water management, etc., and remote sensing technology has made it possible by providing wide and consistent imaging of all points of the earth (for different sensors from 3 hours to 16 days different) (Tatem et al., 2001).

The development of remote sensing technology has enabled the storage of great amount of fine spatial resolution remotely sensed images. These data can provide fine-resolution land cover spatial information and are promising in reducing the SRM uncertainty (Xiaodong et al., 2014). The mixed pixel problem strongly affects the accuracy in extracting land cover information from remotely sensed images (Lu et al., 2011b).

The basic and predominant solution to the interpretation of mixed pixels is based on the fuzzy classification algorithm, but with none of the fuzzy classification methods, the location and position of the land cover class on sub-pixel scale are not determined and for this, it was necessary to use other methods such as super-mapping based on the Hopfield neural network (Tatem et al., 2001). Atkinson assumed the existence of a spatial relationship between and inside pixels to determine the location of different classes in the sub-pixel scale with respect to the output of the initial image fuzzing process (Atkinson, 1997).

Several other factors such as the type of complication, the genus of the earth, the time of imaging plays an important role in the accuracy of extraction of information from satellite imagery. In satellite images, in majority of pixels there is a mixture of coatings and complications, and this affect the subject for the image analysis. Fisher believes that in

remote sensing images, pixels can be broken into smaller pixels, provided that the original pixel values are given to the sub-pixels (Fisher, 1997).

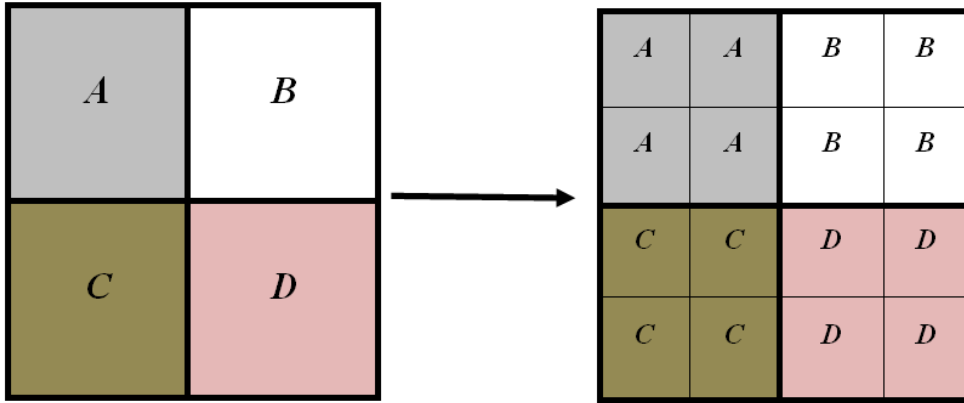


Figure 1. How to break the pixels and set it to the Fisher method

Super-resolution land cover mapping (SRM) (or sub-pixel mapping) is a technique applied to generate land cover maps with finer spatial resolution than the input data (Atkinson, 1997, 2009). This technique has been used for land cover mapping (Tatem et al., 2003; Thornton et al., 2006), waterline mapping (Foody et al., 2005), floodplain inundation mapping (Huang et al., 2014), urban building mapping (Ling et al., 2012b), urban tree mapping (Ardila et al., 2011), and the landscape pattern indices accuracy improvement (Li et al., 2011).

SRM can be categorized into two groups, according to the input data. One group is applied directly on remotely sensed images, including Markov random field based SRM (Li et al., 2012b), SRM with constrained linear spectral un-mixing model (Ling et al., 2012a), and FCM-based SRM (Li et al., 2012a). The other group is applied to land cover fraction images, which are the output of spectral un-mixing or soft classification applied to remotely sensed images. This group of SRM methods involve pixel-swapping model (Su et al., 2012b; Tong et al., 2013), indicator geostatistics based model (Boucher and Kyriakidis, 2006), multiple-point simulation based model (Ge, 2013), linear optimization (Verhoeve and De Wulf, 2002), spatial attraction (Ling et al., 2013b), genetic algorithm (Mertens et al., 2003), interpolation based model (Ling et al., 2013a; Wang et al., 2014b), Hopfield neural network (Muad, 2011; Su et al., 2012a), back propagation neural network (Wu et al., 2011), artificial immune systems based model (Zhong and Zhang, 2013) and multi-scale information based model (Ling et al., 2014).

Another super-resolution HNN-based algorithm was used based on the use of fuzzy output to restrict the energy function (Tatem et al., 2001; Tatem et al., 2001b), in this algorithm, a more precise method has been used for this task, in which the values of the sub-pixel are different with the original pixel values, and this property has the following advantages:

- a) Improve the categorization and location in sub-pixel scale

- b) Calculation of different land covers with a much higher accuracy
- c) Diagnosis of urban objects with higher precision

This algorithm achieved significant success with semi-natural effects, but there is still problem of uncertainty due to the varied complexity in the final reflectance recorded by the sensors.

In another article, the shift and partial change in the position of the effects in the sub-pixel range is used, so that satellite images are collected for a specific location for several days, but the images are not exactly the same due to minor changes in the orbital coordinates of the satellite. You can identify the details of the effects by applying a few images (Ling et al., 2010). In this method, the input parameters of the neural network model were applied with artificial images and the model was implemented for the state of an image, four images, eight images and twelve images, and the improvement of the map accuracy proportional to the increase of the number of images used in the model have been confirmed (Ling et al., 2010).

Xiaodong and his cooperators present a spatial–temporal Hopfield neural network (STHNN) based SRM, by employing both a current coarse-resolution image and a previous fine-resolution land cover map as input (Xiaodong et al., 2014).

Since it is necessary to study the accuracy of the super-resolution algorithm for various complications in terms of tissue, size and imaging sensors, the results should be applied to improve the efficiency of the method. In this study, Super-Resolution algorithm (Hopfield Neural Network) has been using on images of the MODIS and OLI sensors, to examine the results of different effects and prioritize them, which are considered as aspects of innovation in this study.

Despite the wide variety of image complications, it seems that if the super-resolution algorithm is applied to a part of the image (separating the desired frame of the image) constant results are obtained in the accuracy of the extraction of the land covers. Also, the accuracy of the super-resolution algorithm seems to gives different outcomes with different land covers tissues so that they are detected and revealed more uniformly and homogeneously with the borders of the homogeneous tissues. Another hypothesis is that depending on the geometric shape of the land cover, results of the super-resolution algorithm will change in such a way that when the circularity parameter is higher, results in better face detection. The other hypothesis by using super-resolution algorithm can locate and determine the objects with point effects on sub-pixel scale. The general objective of this research is to investigate the Hopfield neural network and achieve a meaningful result in detecting various land covers, by considering the type of land cover and sensory in case of sustainability, the optimal complication categorized for the corresponding sensor is based on the method described above. It is obvious that each of the applied fields of this algorithm can be considered as a specific goal and will result in better extraction of sub-pixel scale land cover and determine the exact boundary achieved for various land covers, which is one of the main objective of remote sensing.

2. Research Methodology

2.1. Location and characteristics of the studied land covers and input maps for the algorithm

Present research is an applied research using Hopfield neural network algorithm on MODIS images and controlling the results with Landsat images. For this purpose, after reviewing the images, the MODIS images include the appropriate spatial land cover classes with acceptable dimensions for use in the selected super-resolution algorithm and raw images were downloaded from the website <http://ladsweb.nascom.nasa.gov/data/search.html>, corresponding to MODIS images and location of the target land covers of the algorithm, relative Landsat images were downloaded with the shooting time approximately same as MODIS images, from the website <http://earthexplorer.usgs.gov>. After the initial study, four images of the MODIS sensor included an Aqua satellite image of March 18, 2016, with a resolution of 250 m from Lavan Island in the Persian Gulf, an Aqua satellite image of July 15, 2016, with a resolution of 250 m Rice fields located in Fars province, a Terra satellite image of April 3, 2016, with a resolution of 250 meters from Sargamish Lake in Turkmenistan and a Terra satellite image of June 17, 2015, with a spatial resolution of 250 m from the vegetation area located in South of the Alborz mountain, and the same number of OLI Landsat8 images are provided for the target areas, coordinate system of images was set using ENVI 4.8 software and geometric correction parameters, and systematic errors, radiometric errors, etc., were corrected and deleted as much as possible, then the images were classified fuzzy and was used as the input data of the algorithm.

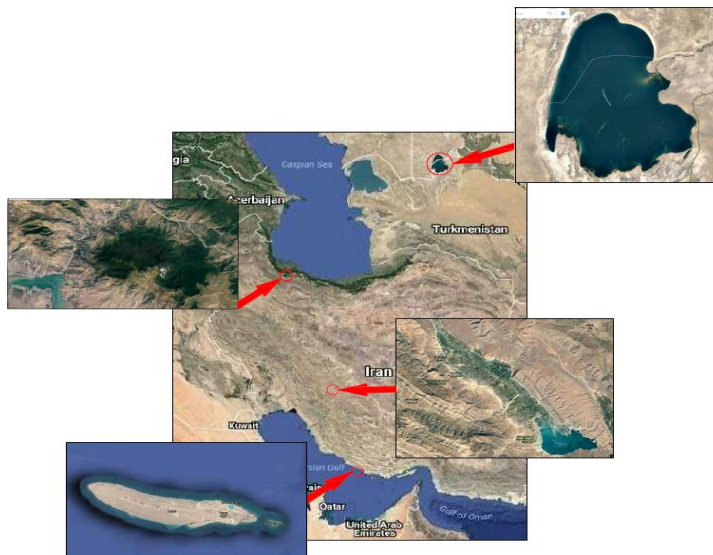


Figure 2. Location of the land cover

2.2. Designing the Neural Network (zoom factor)

In order to allow the entry into the sub-pixel scale, each pixel of the image is converted into $z * z$ network of neurons (actuators) and through these neurons which are at the sub-pixel scale are responsible for determining the location of the effects. According to the pixel values the access to the sub-pixel range has been provided, thereby to improve the classification and the possibility to determine the exact location of the land cover on a smaller scale than the pixel dimensions of the image which can be verified.

The value of z depends on the conditions of the studied case and can be determined optimally according to the results of the algorithm so that; if increase of z does not have a positive effect on the improvement of the results of the algorithm, as increase in z leads to the sharp reduced convergence rate of the algorithm, so as to optimally design the size of neuron network.

In Figure 3, each neuron matrix indicates a land cover class and each neuron (i, j) represents a sub-pixel in the position (i, j) .

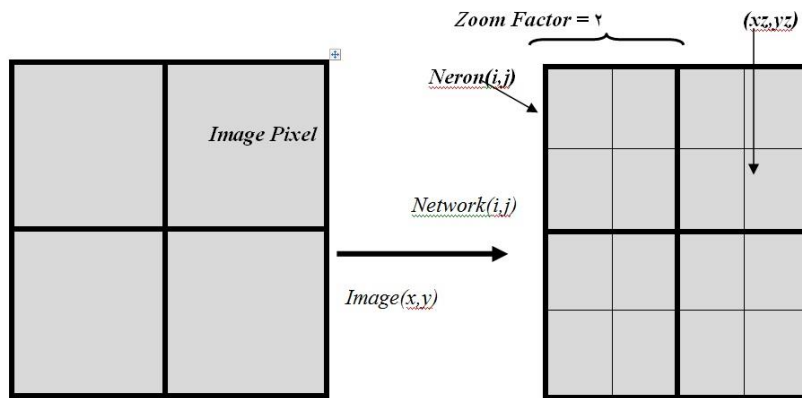


Figure 3. Converting the image to the neuron network

2.3. Primary initialization method to neuron network

In this research, the primary initialization is made intelligently according to proportion of the land cover class in pixels. Based on the principle of spatial correlation of natural phenomena, the neurons close to the center of gravity of the adjacent pixels belonging to the particular class get higher values. This initialization method is used to double the speed of network implementation in the periods of repetition and high zoom factors and the probable bias in the path of the algorithm is acceptable.

2.4. How to implement the algorithm?

In the Hopfield Neural Network (HNN) method, the spatial distribution of the class of land cover at pixel level is defined as formulas and is achieved by minimizing the defined function to the optimal possible state. In this method, the neurons are known by their position, such that the neuron (i, j) in row i and column j has the input value U_{ij} and the output value V_{ij} .

In the neural network method, first, a converted fuzzy image is transformed into a grading space, each neuron is initialized with Unit then the E function is the main equation of the HNN neural network algorithm, including the target functions and the function of the constraint (Limit) is defined as follows:

$$\text{Energy} = \text{Goal} + \text{Constraint} \tag{1}$$

$$E = - \sum_i \sum_j (k_1 G_{1ij} + k_2 G_{2ij} + k_3 P_{ij}) \tag{2}$$

$$dE_{ij} / dv_{ij} = k_1(dG_{1ij} / dv_{ij}) + k_2(dG_{2ij} / dv_{ij}) + k_3(dP_{ij} / dv_{ij}) \tag{3}$$

$$\frac{dG_{1ij}}{dv_{ij}} = \frac{1}{2} (1 + \tanh(\frac{1}{8} \sum_{k=i-1}^{i+1} \sum_{l=j-1}^{j+1} (v_{kl} - 0.5))) \times (v_{ij} - 1) \tag{4}$$

$$\frac{dG_{2ij}}{dv_{ij}} = \frac{1}{2} (1 + (- \tanh(\frac{1}{8} \sum_{k=i-1}^{i+1} \sum_{l=j-1}^{j+1} (v_{kl}))) \times v_{ij} \tag{5}$$

k_1, k_2, k_3 : constant coefficient of weight of various parameters of the energy function
 G_{1ij}, G_{2ij} : The values of the output of the neuron (i, j) for the two target functions
 P_{ij} : The values of the output of the neuron (i, j) for the constraint function.

The energy function E must be minimized, which means that the resultant target functions (G1 & G2) and the constraint function P are the lowest values. This equation is repeated until the difference in the output values of the neurons for two consecutive periods is less than \cong (Epsilon).

$$\sum_{ij} (U_{ij}(t+dt) - U_{ij}(t)) < = \text{TM} \tag{6}$$

In this research, an algorithm function consisting of target functions, increasing and decreasing the values of neurons, and the function of limiting the membership of neurons, is based on determining the location of a particular land cover class in the sub-pixel scale by optimizing the output values. Neurons are related to the natural relationships that points near each other are often more similar in nature. The degree of dissimilarity relates to the environment and the type of data harvest. These impressions can be the same pixels of satellite images, and the discovery of the relationship between pixels is used as the assumption of spatial relationships. In this study, with initialization in the range of [0.3

0.7](intelligence), so that neurons close to the center of gravity of the adjacent pixels have higher values, and finally, after executing the algorithm, we will reach a dipole map representing The location of the class is a special land cover in the sub-pixel scale.

The purpose of this algorithm is to examine the similarity of a neuron's output with respect to adjacent neurons, and if the amount of neurons (i, j) is similar to the average of 8 neurons adjacent, low energy is obtained (the energy function is minimal) And if the output of the central neuron differs from the neighbors, an undesirable condition is obtained based on the definition of spatial relationships (the points are closer to each other are more similar) and are generated a large energy for function. Therefore, for the purpose of producing a dipole map, definition of one function is inadequate, and therefore two objective functions are defined, one for increasing the amount of output of the neuron to one and the other for reducing the output value of the neuron to zero And each one depends on the average output of the 8 Neuron in neighboring.

- The first function (G1) to increase the output of the center neuron to one (vij to 1)
- The second function (G2) to reduce the output of the center neuron to zero (Vij to 0)
- Constraint function

According HNN algorithm, the objective functions will result in the assignment of zero and one outputs for each pixel, so a method to limit the effect of these functions (target functions) is required to apply the function for the areas of the image that is required. If a pixel, X percent belongs to a class, after performing the HNN algorithm and breaking the pixel to the sub-pixels, the total pixels that eventually belong to that class should provide the same percent, and the function Pij applies this limitation.

2.5. Practical methods to improve the efficiency of the algorithm

- Average times for each repeat period
- Define algorithm coefficients
- Zoom Factor Parameter
- Repeat period

Since the land covers differ in nature, such as roads, houses, lakes, forests, agricultural land, etc., these various effects are classified by definition of compactness and circularity parameters. In this study, the effects of the form of land covers on the final results were also examined.

$$r = a / (\pi * Max^2) \quad \text{Circularity} \quad (7)$$

$$C = (4 * \pi * a) / (p^2) \quad \text{Compactness} \quad (8)$$

a is the area of shape, p is periphery of shape and max is maximum distance from center to the edge

2.6. Criteria for evaluating the accuracy of the algorithm

Three main parameters were defined to evaluate the difference between the results of the algorithm implementation on different images.

2.6.1 Area Error Proportion

First parameter is the area error proportion which the amount of bias measured in the results of the algorithm and represents the success rate of the algorithm and is calculated from the following equation based on the output values of the neurons.

$$AEP = \frac{\sum_{q=1}^n (y_q - a_q)}{\sum_{q=1}^n a_q} \tag{9}$$

y is the degree of belonging to a particular class derived from Landsat's classified image
 a is the degree of belonging to a particular class derived from the output of the algorithm
 n is the number of neurons used in the algorithm

2.6.2 Root mean square error

The second parameter is the root mean square error, which in most of the statistical research is an appropriate criterion for accuracy checking. In this study, the accuracy of the estimation for the output values of the neurons has been used. The least squares error value is calculated by using equation 10:

$$RMSE = \sqrt{\frac{\sum_{q=1}^n (y_q - a_q)^2}{n}} \tag{10}$$

2.6.3 Correlation coefficient

The third parameter is the correlation coefficient, which provides an alternative metering to determine the dependence between the results of the algorithm and the initial images, and provides statistical information about the variance and spatial distribution in the sub-pixel range; the correlation coefficient value is computable through equation 11.

$$r = \frac{c_{y,a}}{s_y \cdot s_a} , \quad c_{y,a} = \frac{\sum_{q=1}^n ((\bar{y}_q - y_q) \cdot (\bar{a}_q - a_q))}{n-1} \tag{11}$$

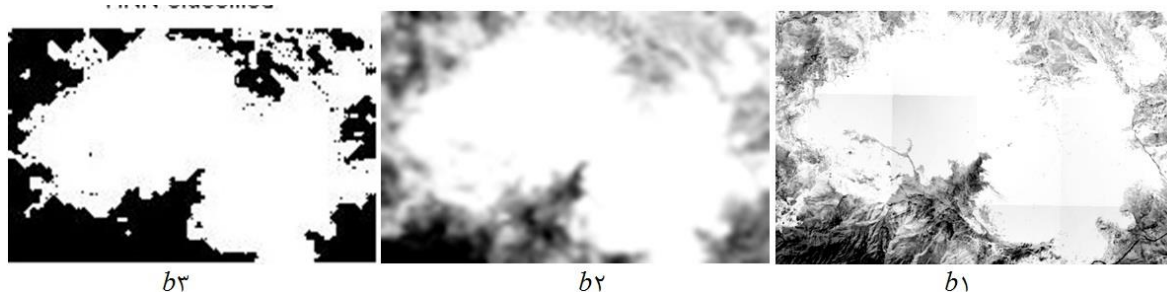
$C_{y,a}$ is covariance between y and a
 S_a and S_y are standard deviation for a and y

3. Results and Discussion

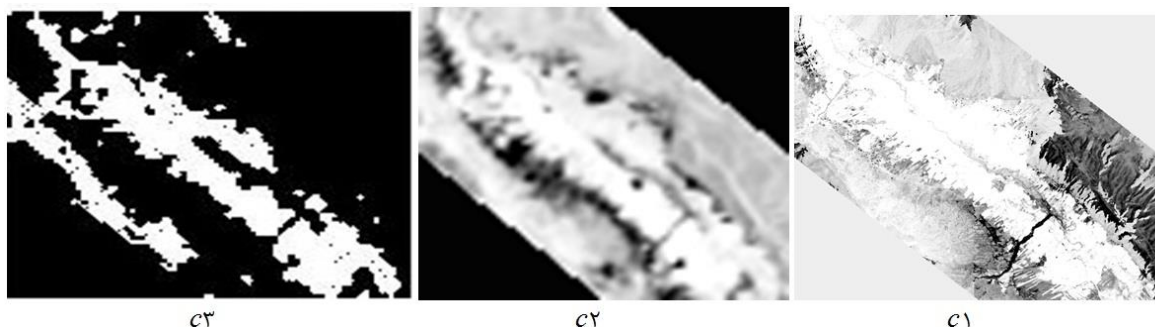
As shown in Fig. 4, the final bipolar maps include the estimated position of the land covers in sub-pixel scale obtained after implementing the algorithm.



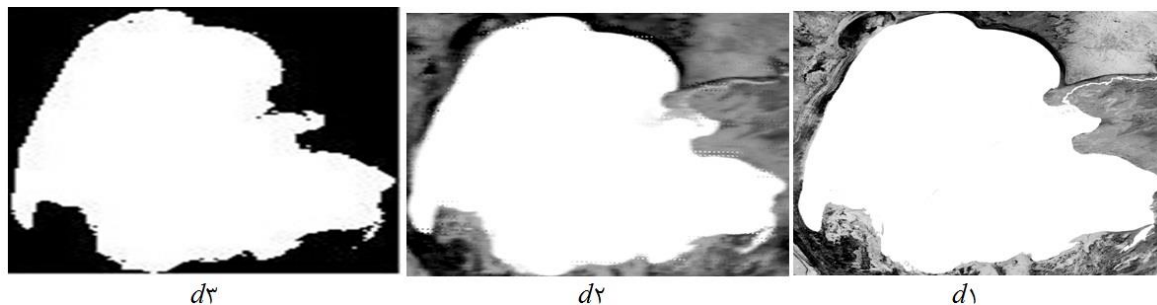
a1: Categorized Image OLI a2: Categorized Image MODIS a3: HNN dipole map with zoom factor 12, iteration 1000, and duration of the algorithm 30 minutes



b1: Categorized Image OLI b2: Categorized Image MODIS b3: HNN dipole map with zoom factor 12, iteration 500, and duration of algorithm execution 35 minutes



c1: Categorized Image OLI c2: Categorized Image MODIS c3: HNN dipole map with zoom factor 12, iteration 400 and duration of algorithm execution 17 min



d1: Categorized Image OLI d2: Categorized Image MODIS d3: HNN dipole map with zoom factor 8, iteration 500 and duration of algorithm 125 min

Figure 4. Bipolar maps (a, b, c, d) obtained from the HNN algorithm with optimal zoom factor

As can be seen in the Figure 4, in case of all land covers of the study area, by increasing the magnitude of the zoom factor, the quality and accuracy of the position of land cover in the sub-pixel scale improves.

3.1 Process of changing the parameters of the algorithm evaluation

In Figure 5, the associated graph with the trend of changes in the parameters of the estimation of the accuracy of the algorithm (correlation coefficient, area error proportion and root mean square error) is related to land class and the use of optimized zoom factor.

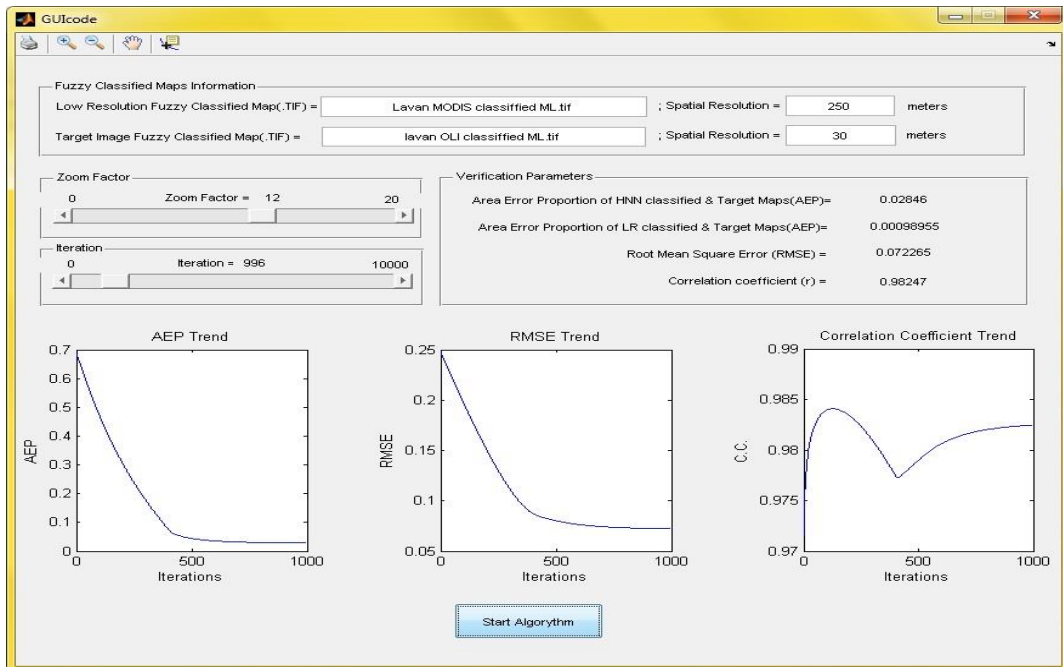


Figure 5. Chart of changes in the parameters of assessment of the accuracy of algorithm for land class (Lavan Island) in Optimal Factor Zoom

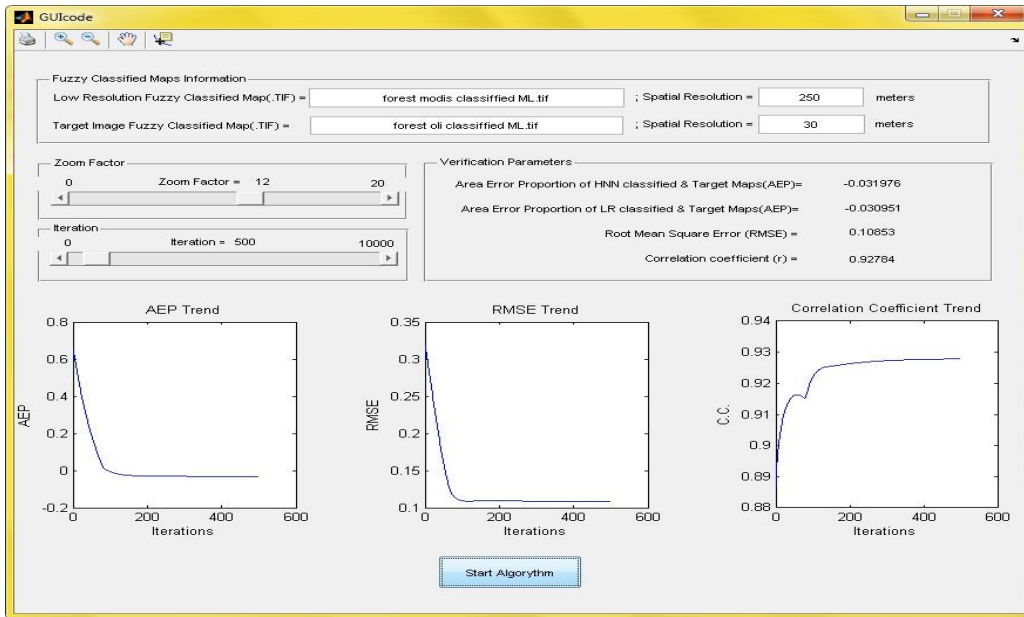


Figure 6. Chart of changes in the parameters of assessment of the accuracy of algorithm for vegetation class (forest) in Optimal Factor Zoom

Comparing Figures 5 and 6 the values of the relevant evaluation parameters is significant; the numerical value of the evaluation parameters shows high accuracy in detecting land class compared to the vegetation class.

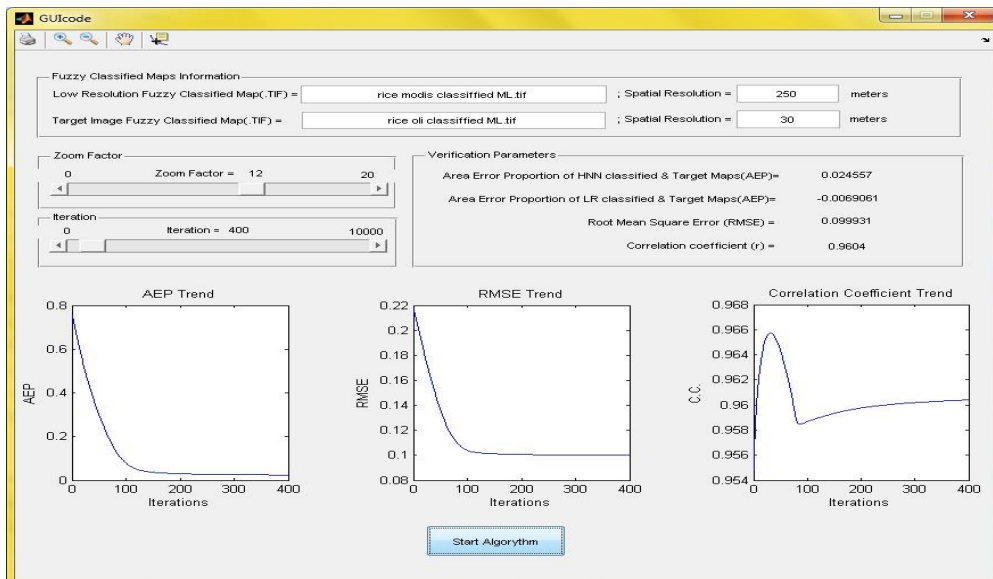


Figure 7. Chart of changes in the parameters of assessment of the accuracy of algorithm for agriculture class (rice) in Optimal Factor Zoom

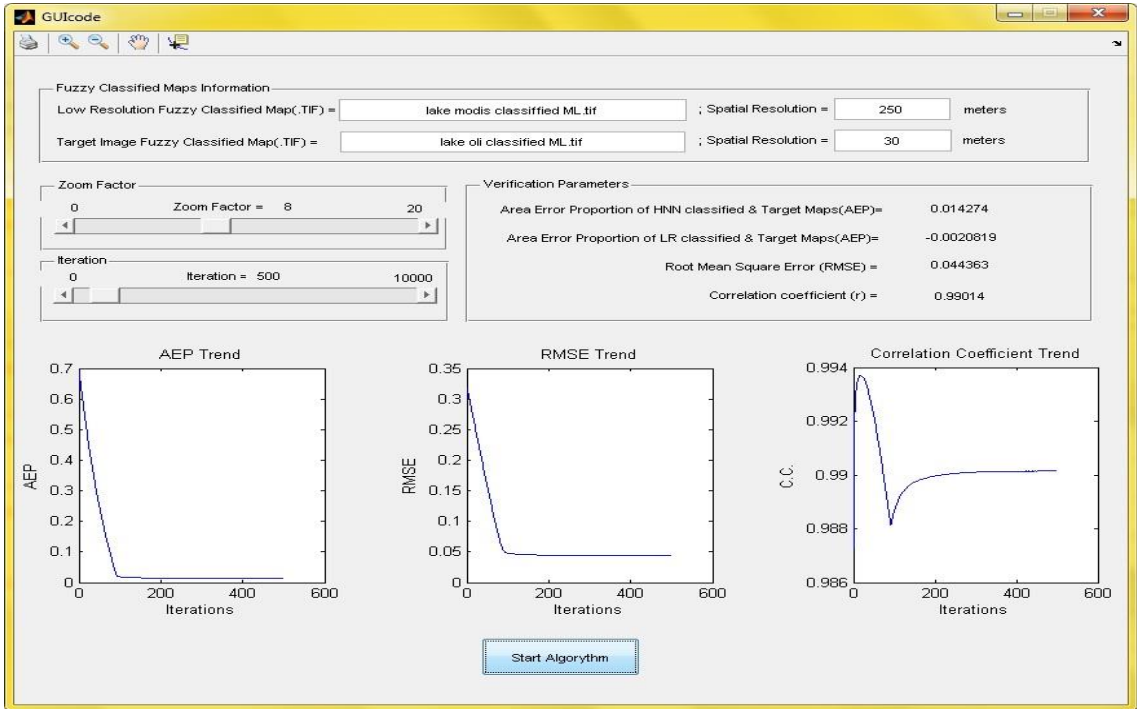


Figure 8. Chart of changes in the parameters of assessment of the accuracy of algorithm for water class (lake) in Optimal Factor Zoom

Comparing Figures 5, 6, 7 and 8, it is clear that the evaluation values of the relevant assessment parameters, the accuracy detection of water is higher than vegetation, land, and agriculture; accuracy detection of land class is higher relative to the land degradation under cultivation and vegetation cover; and the accuracy detection of the agriculture class is higher than the vegetation cover.

Figures 5, 6, 7, and 8 show that for zoom factor 12, the convergence process is performed rapidly and, while obtaining favorable results for the root mean square error and the area error proportion, has been done to achieve high correlation coefficient with acceptable process of change. It should be noted that, the reason for part of the high correlation coefficient is the possibility for precise classification of the input images, partly due to the wide range of land cover studied and, of course, high efficiency of the algorithm.

Also, the results show that, firstly, increasing the zoom factor while reducing the area error proportion rate, leads to a decrease in the resulting bias, which represents the success of the algorithm. Secondly, increasing zoom factor leads to a decrease in the root mean square error rate, which is a suitable criterion for measuring the accuracy of the results. Thirdly, increasing the magnification of the zoom factor increases the correlation coefficient, which indicates that there is correlation between the initial image and the outcomes.

3.2 Reviewing the process of improving the area of exposure

Table 1. Process of improving the apparent area for land class (Lavan Island)

No	Sensor	Zoom factor	No of apparent pixels	Pixel dimension	Area (km ²)
1	OLI	----	82018	30*30 meter	73.816
2	MODIS	1	1140	250*250 meter	71.25
3	MODIS	4	18808	62.5*62.5 meter	73.46
4	MODIS	8	75773	31.25*31.25 meter	73.75

As shown in Table 1, the apparent area of land class was improved from 71.25 to 73.75 km² and its accordance with the reference area (OLI image) indicates a high accuracy of 0.999.

Table 2. Process of improving the apparent area for vegetation class (forest)

No	Sensor	Zoom factor	No of apparent pixels	Pixel dimension	Area (km ²)
1	OLI	----	18559	30*30 meter	162.503
2	MODIS	1	2257	250*250 meter	141.063
3	MODIS	4	39447	62.5*62.5 meter	158.090
4	MODIS	8	159753	31.25*31.25 meter	161.327

As shown in Table 2, the exposed area of vegetation cover from 141.06km² to 161.33km² was improved and its accordance with the reference area indicates a high accuracy of 0.992.

Table 3. Process of improving the apparent area for agriculture class (rice)

No	Sensor	Zoom factor	No of apparent pixels	Pixel dimension	Area (km ²)
1	OLI	----	88524	30*30 meter	79.672
2	MODIS	1	963	250*250 meter	60.188
3	MODIS	4	18894	62.5*62.5 meter	73.800
4	MODIS	8	77335	31.25*31.25 meter	75.522

As seen in Table 3, the apparent area under cultivation improved from 60.19 km² to 75.52km², and its accordance with the reference area indicates a high accuracy of 0.948.

Table 4. process of improving the apparent area for water class (lake)

No	Sensor	Zoom factor	No of apparent pixels	Pixel dimension	Area (km ²)
1	OLI	----	4517211	30*30 meter	4065.49
2	MODIS	1	63157	250*250 meter	3447.31
3	MODIS	4	1023821	62.5*62.5 meter	3999.30
4	MODIS	8	4107981	31.25*31.25 meter	4011.70

As shown in Table 4, the apparent surface area of water has been improved from 3947.31 km² to 4011.70 km², and its accordance with the reference area indicates a high accuracy of 0.987.

3.3 Accuracy check of the algorithm, depending on the shape of land cover

The specification of the land covers including area, compactness coefficient and coefficient of circularity, which is extracted using OLI images, is presented in Table 5.

Table 5. Characteristics of the shape of the land cover

No	Location	Periphery (km)	Area (km^2)	Max distance from center to edge (km)	Compactness	Circularity
1	Lavan Island	52.030	73.816	12.076	0.343	0.161
2	Forest	52.160	162.503	9.760	0.751	0.543
3	Lake	260.600	4,065.490	45.750	0.752	0.618
4	Rice Farm	45.600	79.672	11.500	0.481	0.192

Compactness and circularity parameters are extracted using OLI images. As shown in chart 1, fitted linear regression to the data confirms that, with increasing circularity and compactness, the root mean square error decreases. But, because of the great impact of the type of land covers, its texture and the accuracy of the input images classification of the algorithm in the final results, then the changes are not tangible and definitive comments in this regard are not possible.

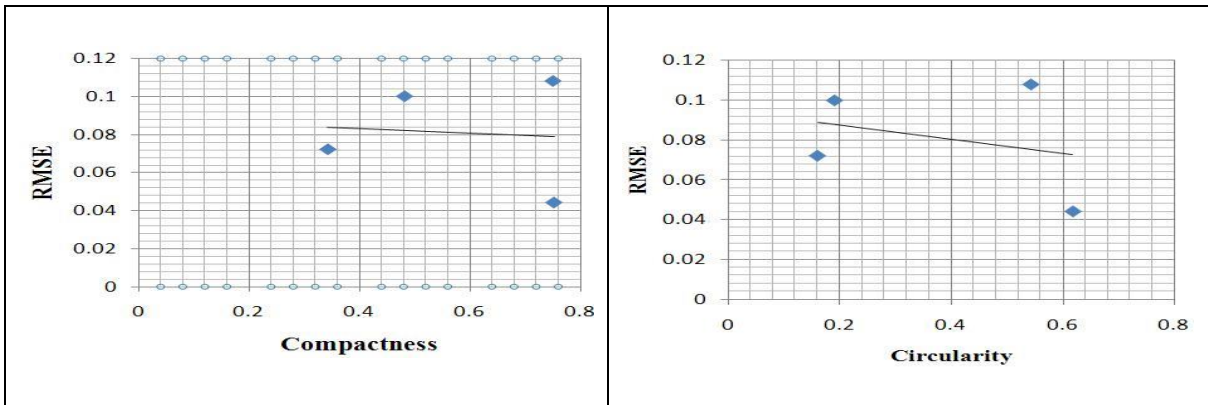


Chart 1. Process of changing the root mean square error values in different circularity and compactness

3.4 Review the changes in algorithm evaluation parameters regardless to land cover type

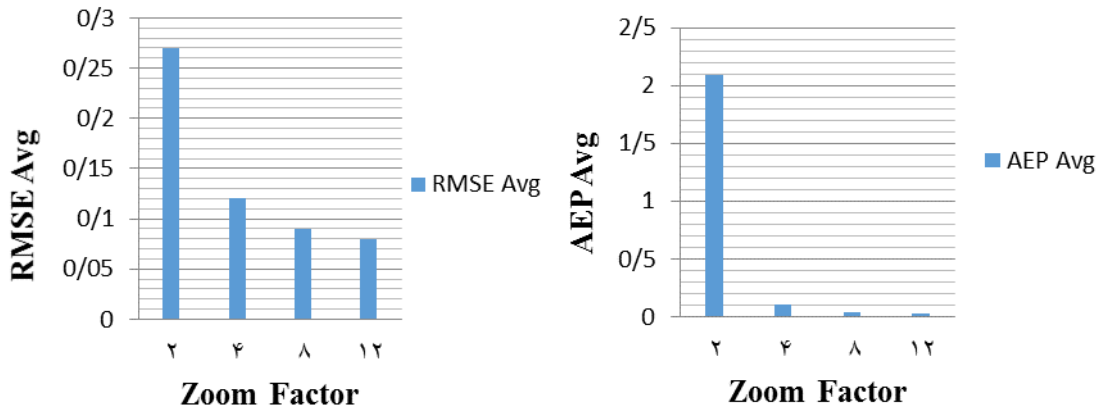


Chart 2. Process of changing the average area error proportion and root mean square error on different zoom factors

Chart 2 illustrates the fact that by increasing the magnitude of the zoom factor, there has been a nonlinear reduction of both parameters, average values of the root mean square error and the average values of the area error proportion level for the various classes. The obvious points in this diagram are, first, the high error in the zoom factor 2, and second is the downward decrease of the average values of the calculated errors. In the review of chart 3, it is obvious that by increasing the zoom factor magnitude, there will be an increase in the mean correlation coefficient for various land covers, a clear indication in this chart is the high correlation between the OLI high resolution classified images and the algorithm results (classification of images with low resolution of MODIS in $z = 12$). Also, as can be seen, there is downward increase of correlation coefficient.

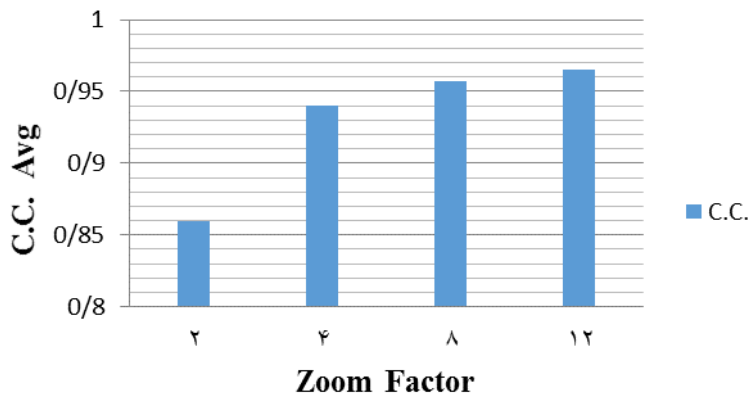


Chart 3. Trend of correlation Coefficient for different zoom factors

3.5 Performance review of the algorithm based on all parameters

Table 6. Characteristics of the classes and results of the algorithm

Agriculture class	Vegetation class	Land class	Water class
0.481 :compactness	0.751 :compactness	0.343 :compactness	0.752 :compactness
0.192 :circularity	0.543 :circularity	0.161 :circularity	0.618 :circularity
79.672 :ref. area	162.503 :ref. area	73.816 :ref. area	km ² 4065.49 :ref. area
75.52 :est. area	161.327 :est. area	۷۳,۷۵ :est. area	4011.70 :est. area
0.948 :Area accuracy	0.992 :Area accuracy	0.999 :Area accuracy	0.987 :Area accuracy
25.47 % :Improved area%	14.3 % :Improved area%	3.5 % :Improved area%	1.63 % :Improved area%
0.0246 : AEP	0.032 : AEP	0.0285 : AEP	0.0143 : AEP
0.1 : RMSE	0.108 : RMSE	0.0722 : RMSE	0.0443 : RMSE
0.96 :correlation Coefficient	0.928 :correlation Coefficient	0.982 :correlation Coefficient	0.99 :correlation Coefficient

By evaluation the data in Table 6 which presents the final results of the algorithm:

- Regarding the AEP parameter that represents the correctness of the algorithm, the best results for the water, agriculture, land and, the vegetation class were recorded.
- Regarding the correlation coefficient parameter, which indicates the precision of spatial distribution of the sub-pixel scale, the best results for water, land, agriculture and vegetation class were recorded.
- Regarding the accuracy parameter of the area calculation, which indicates the proximity of the detected pixels to the OLI image, the best results for land, vegetation, water and cultivated land class were recorded.
- Regarding the parameter of the percentage improvement in area that indicates the effectiveness of the algorithm for a specific class, the best results for the class of cultivated land, vegetation, land and water class were recorded.
- Regarding the RMSE parameter, which best describes the accuracy of the algorithm, the best results for the water, land, cultivated land, and, vegetation class were recorded.

Discussion

The high accuracy of the results presented in Table 6 illustrates the potential of Hopfield's Neural Network algorithm detecting accurately the location of various land cover classes on the sub-pixel scale. The land cover classes that were inspected in this study, the homogeneity and uniformity of the water class led to the high efficiency of the neural network algorithm for this class, and vice versa for vegetation cover class, due to its dispersion and irregularity in the sub-pixel scale, despite the acceptability of efficiency of the algorithm, results with lower accuracy were achieved.

According to Tables 1, 2, 3, and 4, the comparison of OLI-classified images and output maps of Hopfield's super-resolution algorithm proves the ability and efficiency of the algorithm, and the values of revealed surfaces for every land cover have a meaningful proximity to the extracted surfaces from high resolution images. This indicates the high power of the algorithm in detecting and determining the shape of the classes. Another trait

of the algorithm is the detection of the corners of the land cover classes more accurately (closer to reality) and non-abnormal fractures.

In general, in higher zoom factors, due to the access of goals function to smaller areas in the sub-pixel scale, better performance of the algorithm is achievable. With regard to the problem of detecting the corners of the classes, the initial information of the land cover shape can be used as a potential to improve the accuracy of the final maps.

As expected, in the case of vegetation and cultivated land cover, in comparison to the water and land classes, the algorithm for cover classes with complicated, heterogeneous and irregular shapes resulted with less precision. In most of the initial research, artificial images have been used as inputs to investigate the efficiency of the super-resolution algorithm using Hopfield's neural network. In another study in which asphalt and wheat fields were studied, the root mean squares error in zoom factor 5 was 0.1 for Asphalt and 0.1024 for wheat fields, and in zoom factor 7 were 0.094 and 0.088, which showed that the accuracy of the algorithm increases with increasing magnitude of the zoom factor. The values of correlation coefficient parameter, in Factor 7 for asphalt and wheat field were 0.9704 and 0.9799, respectively also the area error proportion parameter in zoom factor 7, the asphalt and wheat field were 0.001 and 0.0001. Comparing the above parameters with the results of this study, Table 6, indicates the proximity of the values and the reliability of the algorithm.

4. Conclusions and suggestions

4.1 Conclusion

The results of the five parameters evaluation, which is the accuracy of the revealed area, the percentage improvement in the exposed area, the area error proportion, the root mean square error and the correlation coefficient show that the algorithm has the best performance for the water class. The three main parameters of the area error proportion, the root mean square error and the correlation coefficient have the best results for the water class, and only two parameters related to the area do not provide significant numbers due to the high accuracy of the initialized classification map. Regarding the vegetation class, in contrast to the water class, all of the three main parameters of the evaluation of algorithm are attributed last-order to this class, which is why the vegetation in the research is in fourth place. Comparing the results of land class and cultivated land class, the land class has the second-lowest root mean square error and the second-highest correlation coefficient. In the parameter, the area error proportion is the third, and vice versa, the class of cultivated land in the two root mean square error and correlation coefficient have the third-order and second rank in the area error proportion, and these two classes in the parameters of the accuracy of the revealed area, the percentage of improvement in the area of exposure, each one has a rank, so the land class in The second place and the class of cultivated land are in the third place.

Based on the above analysis, it can be concluded that the efficiency of the HNN super-resolution algorithm on images of MODIS and OLI sensors in a sub-pixel scale presents the following ranking for revealing the classes studied in this study:

- i. Water class
- ii. Land class
- iii. Cultivated land class
- iv. Vegetation cover class

Generally, increasing the magnitude of the zoom factor from 4 to 12 leads to improve the accuracy and performance of the algorithm for all the classes and the results indicate that the use of zoom factors larger than smaller zoom factors results in more accurate detection of the corners.

Due to the low spatial resolution of the MODIS sensor, the sudden changes in the edge of the effects and the low coverage level (the effects of which are less than a pixel size) cannot be detected. Therefore, this algorithm is applicable to cases such as kilometers forest coverings, sea and lakes, large agricultural land, the extent of fire zones, flood districts, desertification affected areas, the identification of the fire center, military applications in the field of identifying that they create anomaly in any way in the images of the MODIS sensor.

4.2 Suggestion

Regarding the fire complication due to its high anomaly in thermal bands of MODIS sensor and the effect on adjacent pixels, it is possible to determine the edge of the feature class by means of this algorithm more precisely to the point of fire location. This brings a great deal in the direction of discovering a fire point and a faster presence to extinguish and prevent it from spreading.

It is also possible to change the structure of the HNN algorithm, such as how to initialize, how to apply coefficients for different classes depending on compactness and circularity parameters, how to change the averaging method of neurons, how to increase and decrease the values of neurons for each repeat, improved algorithm performance.

References

- Atkinson, P. M. (1997). Mapping sub-pixel boundaries from remotely sensed images. *Innovations in GIS*, 4, 166–180.
- Atkinson, P.M.(2009). Issues of uncertainty in super-resolution mapping and their implications for the design of an inter-comparison study. *International Journal of Remote Sensing*, 30, 5293–5308.

- Ardila, J. P., Tolpekin, V. A., Bijker, W., & Stein, A. (2011). Markov-random-field-based super-resolution mapping for identification of urban trees in VHR images. *ISPRS journal of photogrammetry and remote sensing*, 66(6), 762–775.
- Boucher, A., & Kyriakidis, P. C. (2006). Super-resolution land cover mapping with indicator geostatistics. *Remote Sensing of Environment*, 104(3), 264–282.
- Fisher, P. (1997). The pixel: a snare and a delusion. *International Journal of Remote Sensing*, 18(3), 679–685.
- Foody, G. M., Muslim, A. M., & Atkinson, P. M. (2005). Super-resolution mapping of the waterline from remotely sensed data. *International Journal of Remote Sensing*, 26(24), 5381–5392.
- Ge, Y. (2013). Sub-pixel land-cover mapping with improved fraction images upon multiple-point simulation. *International Journal of Applied Earth Observation and Geoinformation*, 22, 115–126.
- Huang, C., Chen, Y., & Wu, J. (2014). DEM-based modification of pixel-swapping algorithm for enhancing floodplain inundation mapping. *International journal of remote sensing*, 35(1), 365–381.
- Ling, F., Du, Y., Xiao, F., Xue, H., & Wu, S. (2010). Super-resolution land-cover mapping using multiple sub-pixel shifted remotely sensed images. *International Journal of Remote Sensing*, 31(19), 5023–5040 DOI: 10.1080/01431160903252350
- Li, X., Du, Y., Ling, F., Wu, S., & Feng, Q. (2011). Using a sub-pixel mapping model to improve the accuracy of landscape pattern indices. *Ecological Indicators*, 11(5), 1160–1170.
- Lu, D., Moran, E., & Hetrick, S. (2011b). Detection of impervious surface change with multi-temporal Landsat images in an urban-rural frontier. *ISPRS Journal of Photogrammetry and Remote Sensing*, 66(3), 298–306.
- Li, X., Ling, F., & Du, Y. (2012a). Super-resolution mapping based on the supervised fuzzy c-means approach. *Remote Sensing Letters*. 3(6), 501–510.
- Li, X., Du, Y., & Ling, F. (2012b). Spatially adaptive smoothing parameter selection for Markov random field based sub-pixel mapping of remotely sensed images. *International journal of remote sensing*, 33(24), 7886–7901.
- Ling, F., Du, Y., Xiao, F., & Li, X. (2012a). Subpixel land cover mapping by integrating spectral and spatial information of remotely sensed imagery. *IEEE Geoscience and Remote Sensing Letters*, 9(3), 408–412.
- Ling, F., Li, X., Xiao, F., Fang, S., & Du, Y. (2012b). Object-based sub-pixel mapping of buildings incorporating the prior shape information from remotely sensed imagery. *International Journal of Applied Earth Observation and Geoinformation*, 18, 283–292.
- Ling, F., Du, Y., Li, X., Li, W., Xiao, F., & Zhang, Y. (2013a). Interpolation-based super-resolution land cover mapping. *Remote sensing letters*, 4(7), 629–638.

- Ling, F., Li, X., Du, Y., & Xiao, F. (2013b). Sub-pixel mapping of remotely sensed imagery with hybrid intra-and inter-pixel dependence. *International journal of remote sensing*, 34(1), 341–357.
- Ling, F., Du, Y., Li, X., Zhang, Y., Xiao, F., Fang, S., Li, W. (2014). Superresolution land cover mapping with multiscale information by fusing local smoothness prior and downscaled coarse fractions. *IEEE Transactions on Geoscience and Remote Sensing*, 52(9), 5677-5692. <http://dx.doi.org/10.1109/TGRS.2013.2291902>.
- Mertens, K. C., Verbeke, L. P. C., Ducheyne, E. I., & De Wulf, R. R. (2003). Using genetic algorithms in sub-pixel mapping. *International Journal of Remote Sensing*, 24(21), 4241–4247.
- Muad, A. M. (2011). Super-resolution mapping (Doctoral dissertation, University of Nottingham).
- Su, Y. F., Foody, G. M., Muad, A. M., & Cheng, K. S. (2012a). Combining Hopfield neural network and contouring methods to enhance super-resolution mapping. *IEEE Journal of Selected Topics in Applied Earth Observation and Remote Sensing*, 5(5), 1403–1417.
- Su, Y. F., Foody, G. M., Muad, A. M., & Cheng, K. S. (2012b). Combining pixel swapping and contouring methods to enhance super-resolution mapping. *IEEE Journal of Selected Topics in Applied Earth Observation and Remote Sensing*, 5(5), 1428–1437.
- Tatem, A. J., Lewis, H. G., Atkinson, P. M., & Nixon, M. S. (2001). Super-resolution target identification from remotely sensed images using a Hopfield neural network. *IEEE Transactions on Geoscience and Remote Sensing*, 39(4), 781–796.
- Tatem, A. J., Lewis, H. G., Atkinson, P. M., & Nixon, M. S. (2001b). Multiple-class land-cover mapping at the sub-pixel scale using a Hopfield neural network. *International Journal of Applied Earth Observation and Geoinformation*, 3(2), 184–190.
- Tatem, A. J., Lewis, H. G., Atkinson, P. M., & Nixon, M. S. (2003). Increasing the spatial resolution of agricultural land cover maps using a Hopfield neural network. *International Journal of Geographical Information Science*, 17(7), 647–672.
- Thornton, M.W., Atkinson, P. M., & Holland, D. A. (2006). Sub-pixel mapping of rural land cover objects from fine spatial resolution satellite sensor imagery using super-resolution pixel-swapping. *International Journal of Remote Sensing*, 27(3), 473–491.
- Tong, X. H., Zhang, X., Shan, J., Xie, H., & Liu, M. (2013). Attraction-repulsion model-based subpixel mapping of multi-/hyperspectral imagery. *IEEE Transaction on Geoscience and Remote Sensing*, 51(5), 2799–2814.
- Verhoeve, J., & De Wulf, R. (2002). Land cover mapping at sub-pixel scales using linear optimization techniques. *Remote Sensing of Environment*, 79(1), 96–104.
- Wang, Q., Shi, W., & Atkinson, P. M. (2014b). Sub-pixel mapping of remote sensing images based on radial basis function interpolation. *ISPRS Journal of Photogrammetry and Remote Sensing*, 92, 1–15.

- Wu, K., Niu, R., Wang, Y., Zhang, L., & Du, B. (2011). Super-resolution land-cover mapping based on the selective endmember spectral mixture model in hyperspectral imagery. *Optical Engineering*, 50(12), 126201.
- Xiaodong, L., Feng, L., Yun, D., Qi, F., & Yihang, Zh. (2014). A spatial-temporal Hopfield neural network approach for super-resolution land cover mapping with multi-temporal different resolution remotely sensed images. *ISPRS Journal of Photogrammetry and Remote Sensing*, 93, 76–87. <http://dx.doi.org/10.1016/j.isprsjprs.2014.03.013>
- Zhong, Y., & Zhang, L. (2013). Sub-pixel mapping based on artificial immune systems for remote sensing imagery. *Pattern Recognition*, 46(11), 2902–2926.

Using Remote Sensing to Determine of Relationship between Vegetation Indices and Vegetation Percentage (Case Study: Darab Plain in Fars Province, Iran)

Marzieh.Mokarram^{a*}, Alireza.Mahmoodi^b

^a Department of Range and Watershed Management, College of Agriculture and Natural Resources of Darab, Shiraz University, Iran

^b Department of Range and Watershed Management, College of Agriculture and Natural Resources of Darab, Shiraz University, Iran

Received 1 February 2018; revised 22 May 2018; accepted 3 June 2018

Abstract

Vegetation Indices (VIs) obtained from remote sensing (RS) based canopies are quite simple and effective algorithms for quantitative and qualitative evaluations of vegetation cover, vigor, and growth dynamics, among other applications. In the study for modeling and estimated of density and percentage vegetation value of *Artemisia Herba alba* was used Green Difference Vegetation Index (GDVI), Normalized Difference Vegetation Index (NDVI), Optimized Soil Adjusted Vegetation Index (OSAVI), Soil Adjusted Vegetation Index (SAVI) by Landsat 8 ETM+ bands vegetation in the Fathabad of Darab plain, Iran in 2015. By software ENVI preprocessing, processing, geometric and atmospheric corrections were performed, and then vegetation index for the study area was calculated. Also, ArcGIS 10.2 software for mapping of area vegetation was applied. Then the relationship between Vegetation Indices, density and vegetation value of *Artemisia herba alba* was determined. The results show that with increasing of percentage and density of vegetation, the value of vegetation indices increases. Finally, in order to determination of suitable elevation of growing of *Artemisia herba alba* was determined relationship between elevation and percentage of vegetation. The results show that the best elevation for growing of *Artemisia herba alba* was 1767 to 1782.

Keywords: Vegetation Indices (VIs), Remote sensing (RS), *Artemisia herba alba*.

* Corresponding author. Tel: +98-9178020115.

E-mail address: m.mokarram@shirazu.ac.ir.

1. Introduction

Remote sensing (RS) for vegetation studies use data by satellite sensors that measure wavelengths of light absorbed and reflected by green plants. RS of vegetation is mainly performed by obtaining the electromagnetic wave reflectance information from canopies using passive sensors. The reflectance from vegetation to the electromagnetic spectrum is determined by chemical and morphological characteristics of surface of leaves (Zhang and Kovacs, 2012).

Vegetation Indices (VIs) extracted from light spectra range can be attributed to a range of characteristics beyond growth and vigor quantification of plants related to yield (Foley et al., 1998; Batten, 1998). Therefore, Vegetation Indices obtained from the spectra range can be used as a proxy to assess stomata dynamics that regulates transpiration rate of plants. However, the applicability of remote sensing and its different VIs extracted from these techniques usually relies heavily on the instruments and platforms to determine which solution is best to get a particular issue (Xue and Su, 2017).

According to the importance of the Vegetation Indices, the present study is an attempt to determine the relationship between percent and density of the vegetation and Vegetation Indices (VI) for *Artemisia herba alba*. The *Artemisia herba alba* or *A. sieberi* is a medicinal plant that some pharmacological effects of *A. sieberi* plant such as spasmolytic, vermifugal (1), insecticidal (2), anticandidal (3) and asexual reproduction inhibition of some filamentous fungi (4) were confirmed (Mahboubi and Farzin, 2009).

A study on *A. herba-alba* species collected from Sinai and Israel desert showed that Siniol, Thujone, Borneol, and Pinene were the main groups of combinations found in the plant; so that their concentration was a factor of their habitat (Feuerstein et al., 1988). The Pasture Technical Office started to collect and code plants in the pasture and commented on the capacity of *Artemisia* and *A. sieberi* in particular in 1991. Rabie et al. (2007) confirmed the title *A. sieberi* after phytochemical studies on 34 species of *Artemisia* in Iran and *Artemisia herba alba* from Spain and *A. siberi* from Palestine (Rabie et al., 2007). Mirza et al. (1998) extracted and studied essence of species of *Artemisia* genus and *A. sieberi* in particular from quantitative and qualitative viewpoint (Mirza et al., 1998). Also, Mozafarian (1996) was determined the habitats of *Artemisia herba-alba* in Iran.

In order to Determine the relationship between percentage and density of vegetation was used vegetation indices. Many studies on the use of remote sensing techniques and vegetation indices in agriculture and natural resources are done. Arzani et al (2009) using indicators SAVI (Soil-adjusted Vegetation Index), MSAVI (Modified Soil Adjusted Vegetation Index) and PVI have proposed to estimate the crown of Vegetation. In northern China, Bao et al (2009) predicted winter wheat biomass and Ren et al (2008) monitored winter wheat yield using data from Modis, and Koppe et al (2012) estimated estimated winter wheat biomass using Hyperion data. Vegetation index NDVI (Normalized Difference Vegetation Index), NDVI-RE (Red Edg NDVI), msR-RE (Modified Red Edge Simple Ratio) and Curvature demonstrated that the spatial and temporal variations in leaf

area index (LAI) as well can be estimate (Tillack et al., 2014). Ren et al (2011) showed that the linear model based on NDVI (862, 693 nm) relative to the index, SAVI is composed of 887 and 685 nm bands had a better estimates of green biomass of the desert steppe. Baihua and Burgher (2015) stated that the vegetation index NDVI is a good indicator to identify and assess long-term changes in the areas of vegetation.

Allbed et al., 2014 determined relationship between soil salinity and vegetation indices derived from IKONOS high-spatial resolution imageries. The results show that among the investigated indices, the Soil-Adjusted Vegetation Index (SAVI), Normalized Differential Salinity Index (NDSI) and Salinity Index (SI-T) yielded the best results for assessing the soil salinity of cultivated lands with dense and uniform vegetation.

Modeling vegetation was used Yospin et al. (2015) parameterized Fire BGCv2 to identify the effects of different levels of ignition suppression on landscape-level patterns of vegetation and successional dynamics in sub-alpine Tasmania. The results show that because the distribution of vegetation types was unstable temporally and across stochastic replicates, present distributions may be a legacy of previous climate, Aboriginal fire management, or both.

The study area aim is modeling and understanding the behavior of Vegetation Indices for *Artemisia herba alba* in the Fathabad Darab plain in Fars province, Iran. For determination of relationship between vegetation indices and *Artemisia herba alba* was used GDVI, NDVI, OSAVI, SAVI based on Landsat 8 ETM+ in 2015 years.

2. Material and Methods

2.1. Case study

The case areas was located in east of Darab plain, Fars province, Iran. The locations of the case areas are shown in Figure 1. In the study for determination of relationship between vegetation indices and density of *Artemisia herba alba* fifty points were used that are shown in Figure 2. According to Figure 2 distribution of points were quite randomly.

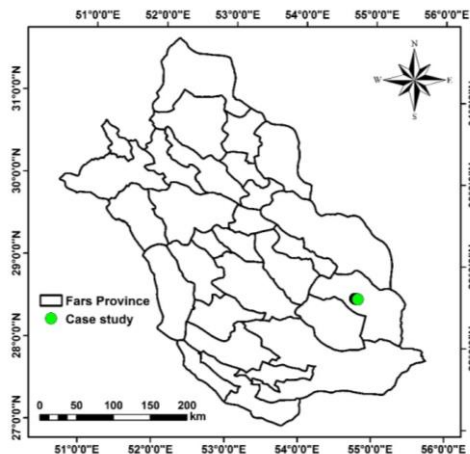


Figure 1. Position of the study area

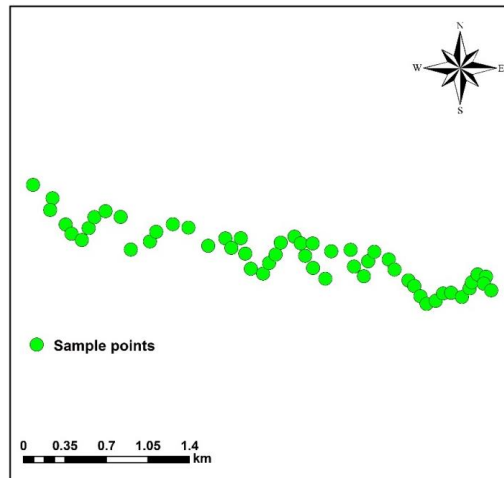


Figure 2. Position of sample points in the study area

2.2. Methods

In this study to calculate the Generalized Difference Vegetation Index (GDVI), Normalized Difference Vegetation Index (NDVI), optimized soil adjusted vegetation index (OSAVI), soil adjusted index (SAVI) have been used that the equations of each indices are in the following:

Green Difference Vegetation Index (GDVI)

This index was originally designed with color-infrared photography to predict nitrogen requirements for corn (Sripada, et al., 2006).

$$GDVI = NIR - Green \quad (1)$$

Normalized Difference Vegetation Index (NDVI)

This index is a measure of healthy, green vegetation. The combination of its normalized difference formulation and use of the highest absorption and reflectance regions of chlorophyll make it robust over a wide range of conditions. It can, however, saturate in dense vegetation conditions when LAI becomes high (Rouse et al., 1973).

$$NDVI = \frac{(NIR - Red)}{(NIR + Red)} \quad (2)$$

The value of this index ranges from -1 to 1. The common range for green vegetation is 0.2 to 0.8.

Optimized Soil Adjusted Vegetation Index (OSAVI)

This index is based on the Soil Adjusted Vegetation Index (SAVI). It uses a standard value of 0.16 for the canopy background adjustment factor. Rondeaux (1996) determined that this value provides greater soil variation than SAVI for low vegetation cover, while

demonstrating increased sensitivity to vegetation cover greater than 50%. This index is best used in areas with relatively sparse vegetation where soil is visible through the canopy.

$$OSAVI = \frac{1.5 * (NIR - Red)}{(NIR + Red + 0.16)} \quad (3)$$

Soil Adjusted Vegetation Index (SAVI)

This index is similar to NDVI, but it suppresses the effects of soil pixels. It uses a canopy background adjustment factor, L, which is a function of vegetation density and often requires prior knowledge of vegetation amounts. Huete (1988) suggests an optimal value of L=0.5 to account for first-order soil background variations. This index is best used in areas with relatively sparse vegetation where soil is visible through the canopy.

$$SAVI = \frac{1.5 * (NIR - Red)}{(NIR + Red + 0.5)} \quad (4)$$

For preparing each of indices was used bands 1, 2, 3, 4, 5 and 7 Landsat 8 ETM + sensor, 2015 years. Spectral characteristics of ETM + bands are shown in Table 1:

Table 1. Spectral characteristics of Landsat 8 ETM +

Spectral Band	Wavelength	Resolution
Band 1 - Coastal / Aerosol	0.433 - 0.453 μm	30 m
Band 2 - Blue	0.450 - 0.515 μm	30 m
Band 3 - Green	0.525 - 0.600 μm	30 m
Band 4 - Red	0.630 - 0.680 μm	30 m
Band 5 - Near Infrared	0.845 - 0.885 μm	30 m
Band 6 - Short Wavelength Infrared	1.560 - 1.660 μm	30 m
Band 7 - Short Wavelength Infrared	2.100 - 2.300 μm	30 m
Band 8 - Panchromatic	0.500 - 0.680 μm	15 m
Band 9 - Cirrus	1.360 - 1.390 μm	30 m

First, using ENVI v.5 preprocessing like geometric and atmospheric corrections were performed, and then vegetation indices for the study area was calculated. ArcGIS10.2 software for mapping of area vegetation was used. Then indexes compared with land use map in order to determine best index for estimate vegetation in study area.

3. Results and Discussion

The results of the vegetation indices maps (GDVI, NDVI, OSAVI and SAVI) in the study area show in the Figure 3. According to Figure 3, value of indices were high in the agriculture field for NDVI and low for OSAVI, SAVI and GDVI indices. Vegetation is low in the salt land. So salt land seen white color in satellite images (Prost, 2013). The OSAVI was between -0.43 to 0.89, SAVI was between -0.18 to 0.5, GDVI was between -0.06 to 0.2 and NDVI was -1 to + 1.

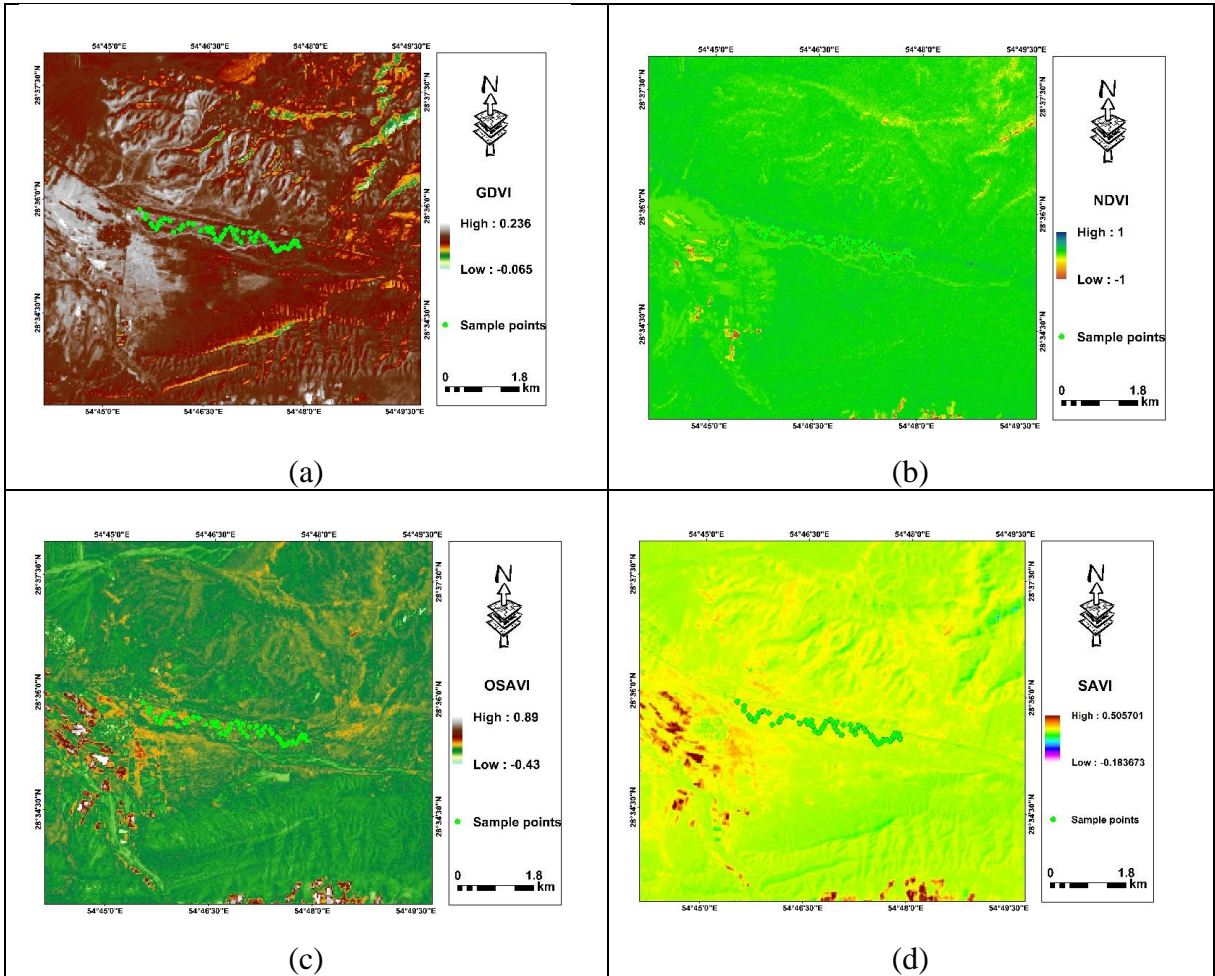


Figure 3. Vegetation indices of the study area. (a): GDVI, (b): NDVI, (c): OSAVI, (d): SAVI

In order to determine the relationship between vegetation index, density and percentage of vegetation indices 15 sample points were used that are shown in Figure 4 and Figure 5, respectively.

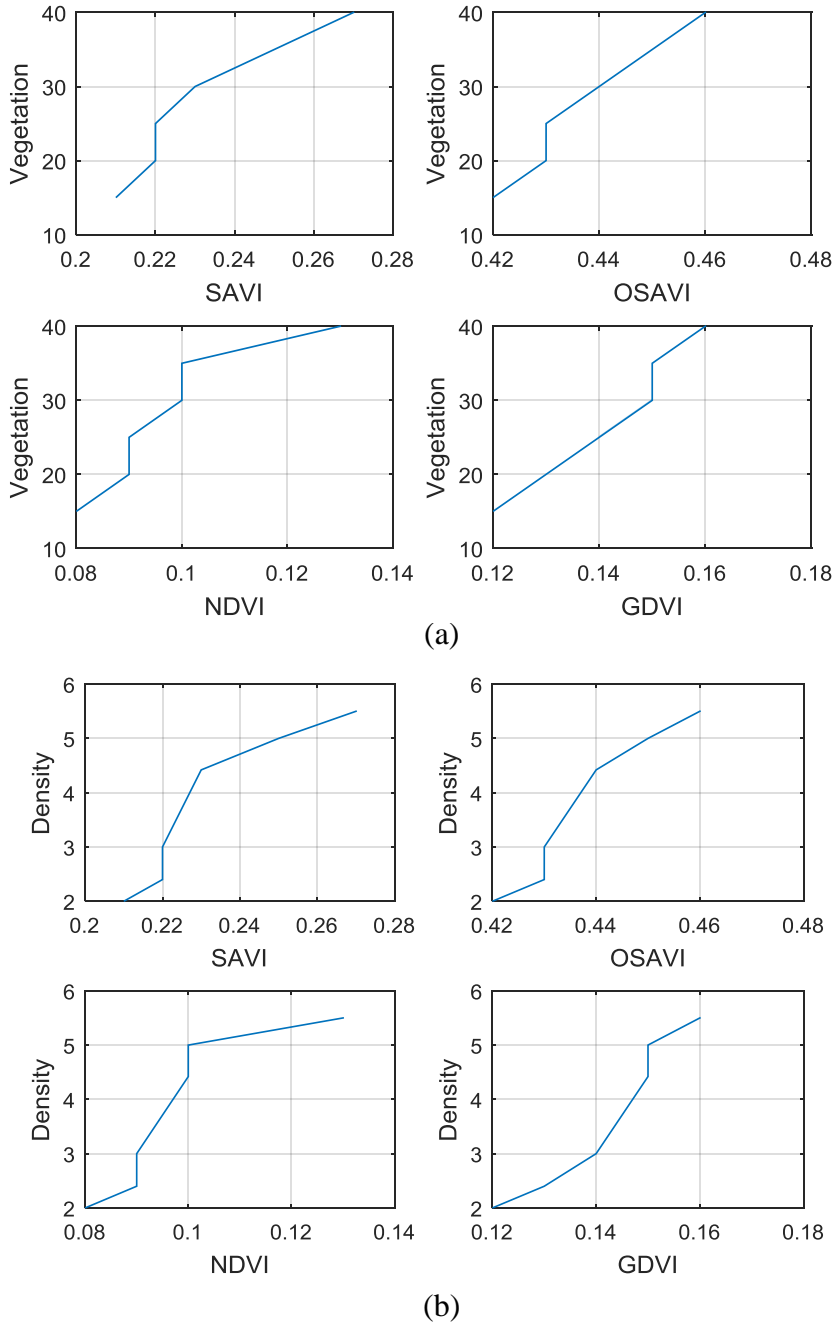


Figure 4. The comparison of vegetation indices in the study area and sample points plotted versus for the vegetation value (a) and value of the density (b).

The results of two Figures show that with increasing of percentage and density of vegetation, the value of vegetation indices increase. Finally, in order to determination of suitable elevation of growing of *Artemisia herba alba* was determined relationship between elevation and percentage of vegetation. According to Figure 5, the best elevation for growing of *Artemisia herba alba* was 1767 to 1782.

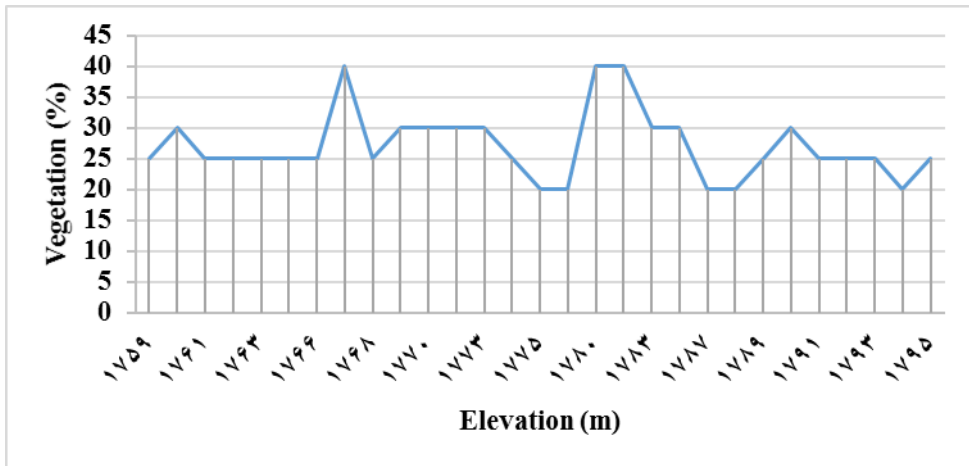


Figure 5. Relationship between elevation and percentage of vegetation for *Artemisia herba alba*

4. Conclusions

Remote sensing is the advanced tool for surveying. It provides the synoptic view of the area. Remote sensing satellites provide data with different spatial, spectral, radiometric and temporal resolutions. In the present study, the relationship between vegetation Indices, density and vegetation value of *Artemisia herba alba* were determined. Due to the importance of *Artemisia herba alba* in medical especially in traditional medicine, the study aimed to investigate this plant. Using remote sensing techniques in the study of vegetation has resulted in a low volume having access to a host of information with a high accuracy. In the study area, the relationship between indices GDVI, NDVI, OSAVI, SAVI and density and percentage of *Artemisia herba alba* were determined. With the increase of the percentage and density of vegetation, the value of vegetation indices increased. Finally, in order to determination of suitable elevation of growing of *Artemisia herba alba* was determined relationship between elevation and percentage of vegetation. Also, the best elevation for growing of *Artemisia herba alba* was 1767 to 1782. Generally, the results of the study showed that vegetation index compared with measured vegetation has benefits including reduced time, frequency of data and saving the cost and labor.

References

- Allbed, A., Kumar, L., & Aldakheel, Y.Y. (2014). Assessing soil salinity using soil salinity and vegetation indices derived from IKONOS high-spatial resolution imageries: Applications in a date palm dominated region. *Geoderma*, 230–231, 1–8.
- Arzani, H., Noori, S., Kaboli, S. H., Moradi, H. R., & Ghelichnia, H. (2009). Determination of Suitable Indices for Vegetation Cover Assessment in Summer Rangelands in South of Mazandaran, *Journal of the Iranian Natural Res*, 61(4), 997-1016.
- Baihua F. & Burgher, I. (2015). Riparian vegetation NDVI dynamics and its relationship with climate, surface water and groundwater, *Journal of Arid Environments*, 113, 59-68.
- Bao, Y., Gao, W., Gao, Z. (2009). Estimation of winter wheat biomass based on remotesensing data at various spatial and spectral resolutions. *Front. Earth Sci. China*, 3(1): 118–128.
- Batten, G. D. (1998). Plant analysis using near infrared reflectance spectroscopy: The potential and the limitations. *Australian Journal of Experimental Agriculture*. 38(7) 697–706.
- Feuerstein, I., Danin, A. & Segal, R. (1988). Constitution of the essential oil from an *Artemisia herba-alba* population of Spain. *Phytochemistry*, 27: 433-434.
- Foley, W. J. McIlwee, A. Lawler, I. Aragonés, L. Woolnough, A. P. & Berding, N. (1998). Ecological applications of near infrared reflectance spectroscopy - A tool for rapid, cost-effective prediction of the composition of plant and animal tissues and aspects of animal performance. *Oecologia*, vol. 116 (3), 293–305.
- Huete, A. R. (1988). A soil-adjusted vegetation index (SAVI). *Remote sensing of environment*, 25(3), 295-309.
- Koppe, W., Gnyp, M.L., Hennig, S.D., Li, F., Miao, Y., Jia, L., Bareth, G. (2012). Multi-temporal hyperspectral and radar remote sensing for estimating winter wheat biomass in the North China Plain. *Photogramm. Fernerkun. Geoinf.* (3), 281–298.
- Mahboubi M., Farzin N. (2009). Antimicrobial activity of *Artemisia sieberi* essential oil from central Iran. *IJM Iranian journal*. 1 (2), 43 – 48.
- Mirza, M., Sefidkan, F. & Ahmadi, L. (1998). *Natural Essential Oil, Extraction Qualitative*. Tehran, Institute of Jungles and Grasslands Researches.
- Mozafarian, V. A. (1996). *Dictionary of Iranian Plant Names (Latin, English, Farsi)*. Tehran, Farhang-E-Moaser.
- Prost, G. L. (2013). *Remote sensing for geoscientists: image analysis and integration*. CRC Press.
- Rabie, M., Jalili, A., Azarnivand, H., Jamzad, Z. & Arzani, H. (2007). A contribution to the *Artemisia sieberi* (Asteraceae) based on photochemical studies in Iran. *Journal of Botany*, 13: 120-8.
- Ren, H., Zhou, G. & Zhang, X. (2011). Estimation of green aboveground biomass of desert steppe in Inner Mongolia based on red-edge reflectance curve area method. *Biosystems Engineering*, 109 (4): 385–395.

- Ren, J., Chen, Z., Zhou, Q. & Tang, H. (2008). Regional yield estimation for winter wheat with MODIS-NDVI data in Shandong, China. *Int. J. Appl. Earth Obs. Geoinf.*, 2008, 10 (4):403–413.
- Rondeaux, G., Steven, M., & Baret, F. (1996). Optimization of soil-adjusted vegetation indices. *Remote sensing of environment*, 55(2), 95-107.
- Rouse J, Haas R, Schell J, Deering D (1973) Monitoring vegetation systems in the great plains with ERTS. In: Freden SC, Mercanti EP, Becker MA (eds) *Third Earth Resources Technology Satellite-1 Symposium- Volume I: Technical Presentations. NASASP-351*. NASA, Washington, DC, p 309.
- Sripada, R. P., Heiniger, R. W., White, J. G., & Meijer, A. D. (2006). Aerial Color Infrared Photography for Determining Early In-Season Nitrogen Requirements in Corn This project was supported in part by Initiative for Future Agriculture and Food Systems Grant no. 00-52103-9644 from the USDA Cooperative State Research, Education, and Extension Service. *Agronomy Journal*, 98(4), 968-977.
- Tillack, A., Clasen, A., Kleinschmit, B. & Forster, M. (2014). Estimation of the seasonal leaf area index in an alluvial forest using high-resolution satellite-based vegetation indices, *Remote Sensing of Environment*, 141 :52–63.
- Xue, J. and Su, B., 2017. Significant remote sensing vegetation indices: a review of developments and applications. *Journal of Sensors*, 1353691, 17.
- Yospin, G. I., Wood, S. W., Holz, A., Bowman, D. M., Keane, R. E., & Whitlock, C. (2015). Modeling vegetation mosaics in sub-alpine Tasmania under various fire regimes. *Modeling Earth Systems and Environment*, 1(3), 16.
- Zhang C. & Kovacs, J. M. (2012). The application of small unmanned aerial systems for precision agriculture: a review. *Precision Agriculture*, 13 (6) 693–712.

Detecting Spatial-Temporal Changes in Land Use Using Satellite Data in Haraz Basin

Naser Ahmadi Sani ^{a*}, Karim Solaimani ^b, Lida Razaghnia ^c

^a Assistant Professor, Faculty of Agriculture and Natural Resources, Mahabad Branch, Islamic Azad University, Mahabad, Iran.

^b Professor, Department of Watershed Management, Sari university, Iran.

^c MSc. of Watershed Management, Department of Watershed Management, Haraz University, Iran.

Received 6 April 2018; revised 18 May 2018; accepted 13 June 2018

Abstract

In recent decades, rapid and incorrect changes in land use have been associated with consequences such as natural resources degradation and environmental pollution. Detecting land use changes is a suitable technique for natural resources management. The goal of this research is to study the land use change in Haraz Basin with an area of 677000 hectares in 15 years (1996-2011) using Landsat data. After making the necessary corrections and preparing the indices, images were categorized into nine classes via supervised classification and Maximum Likelihood Algorithm. Finally, the changes were extracted by post-classification comparison. The results showed that there has been a 27.5% change in land use of the area during the 15 years. These changes are related to conversion of rangelands to bare lands and dry farming ones, and conversion of dense forests to sparse forests, horticulture, farming lands, and residential areas. These changes can be due to an increase in population and human activities, which result in increasing demands for natural resources and converting them into farming lands, horticulture, residential and industrial areas. These land use changes along with climate changes raise the alarm for the Haraz Basin status in the future.

Keywords: Change Detection, Haraz Basin, Land Use, Remote Sensing.

* Corresponding author. Tel: +98-9142960545.

E-mail address: n.ahmadisani@gmail.com.

1. Introduction

With the growing population, lands under cultivation can no longer provide the needs of people. Therefore, more lands are needed to be cultivated which in long terms will result in a decrease in quality and quantity of natural resources (Kamkar and Mahdavi-Damghani, 2012). Today, unplanned land use change is a major problem. Natural processes are affected by the characteristics of land use of the basin (Sreenivasulu and Bhaskar, 2010).

In a time period spatial distribution of changes is an important issue in studies related to natural resource (Baboo and Devi, 2010). Land use change is one of the most important indicators in understanding the interactions between human and the environment (Li et al., 2017). Both human-induced and natural land cover changes can influence the global change because of its interaction with the terrestrial ecosystem, biodiversity, and landscape ecology. In addition, it reflects the human impacts on the environment at various temporal and spatial scales. Therefore, accurate and up-to-date land use information is essential for environmental planning as well to achieve sustainable development (Haque and Basak, 2017).

Change detection is the measure of the thematic change information that can guide tangible insights into an underlying process involving land cover, land use and environmental changes (Lal and Anouncia, 2015). Change detection plays a pivotal role in sustainable development of human society. Change detection methods find the changes in a geographical area with the use of bi-temporal images of the area (Singh and Singh, 2018).

There are two broad methods for Change Detection techniques; pre-classification and post classification method. Pre-classification method analyses the change without classifying the image value. The NDVI is most common and widely used pre-classification method. Post classification evaluates the change in land cover based on detail classification of land cover. Post classification comparison is the most common change detection approach. Post classification analysis is quite flexible and easy to quantify the statistics of change class (Haque and Basak, 2017).

Many studies in recent years point out that, there is a rapid change in land cover in many parts of the world, particularly in areas with high population density. Traditionally land use and land cover is a core information layer for a variety of scientific activities and administrative tasks such as hydrological modeling, climate models and land use planning (Gadrani et al., 2018). The sustainable management of watersheds needs monitoring, understanding the dynamics of changes, ecosystem response to social and natural pressures, the information providing on planning for natural resource conservation (Nowroozi et al., 2012).

Nowadays, natural hazards such as flood, landslide, and erosion in many areas of Iran are noticed (Hosseinzade et al., 2009). Haraz Basin has a high potential for such phenomena (Mohammadi et al., 2009). In order to tackle such problems, there is a need to study the land use changes of the basin in recent years to have a close and timely glance for changing, adjusting and planning of water resources, natural resource protection and

decrease the soil erosion in accordance with basin correct management and achieving sustainable development. On the other hand, providing a land-use map using fieldwork method is expensive and time-consuming. Therefore, methods like remote sensing in a short period of time and with less cost, can provide maps with reasonable accuracy.

Remote sensing is an appropriate tool for providing information. Remote sensing is now providing an effective tool for the advanced ecosystem and socioeconomic management (Haque and Basak, 2017). Remote sensing is a powerful and cost-effective data source for assessing the spatial and temporal dynamics of land use/land cover (Li et al., 2017). Over the past ten years, remotely sensed data used for studying the land use changes of (Gadrani et al., 2018). Remote sensing change detection quantifies the effects of humans on a landscape scale without creating further disturbances to ecologically sensitive areas; the results of which can be used for effective conservation management into the future (Willis, 2015). Satellite images are being widely used for change detection applications like urban planning, vegetation monitoring, forest cover management, disaster management (Singh, and Singh, 2018).

Remote sensing and GIS are useful in analyzing the land cover changes in basins. In fact, multi-temporal data obtained from remote sensing are effective in mapping and detecting changes of the landscape (Yin and He, 2012). By mixing the data obtained from remote sensing and GIS, the land cover changes pattern during the time period can be analyzed and detect the changes (Fichera et al., 2012). Various researchers of inside and outside the country have been done about the land-use change detection using satellite data and different analyzing methods (Matkan et al., 2010; Babykalpana and Thanushkodi, 2011; Vafaei et al., 2013).

Many stakeholders worldwide have acknowledged the advantages of remote sensing. Satellite imagery is the most useful tool employed while studying the land use change. On the other hand, Landsat imagery is practically free with oldest records in the archive date back to the 1970s (Gadrani et al., 2018). The utilization of remote sensing data allows getting spatial data in relatively short and vast areas with high accuracy and low cost compared with the conventional way. Remote sensing also can be multi-temporal which allows analysis of land use changes for few years efficiently. Moreover, understanding the proportion of land use changes over time is essential for planning and development of control measures. According to the study hypotheses, many changes have occurred in the Haraz basin from 1996 to 2011. The Landsat imagery has a high potential for spatiotemporal change detection in land use. Therefore, detecting the comprehensive spatial and temporal changes of the entire basin of Haraz with the use of accessible and low-cost data for both periods, as well as the use of convenient and accurate analysis methods considered as the research innovation. Based on the above ideas, this study aim to quantitative assessment, land use mapping and detect changes during the period using the Landsat imagery in Haraz Basin.

2. Study area

The study area is Haraz Basin, which covers 677000 ha in Mazandaran Province (Figure 1). This area is mostly for range, forest, farming and horticulture land uses.

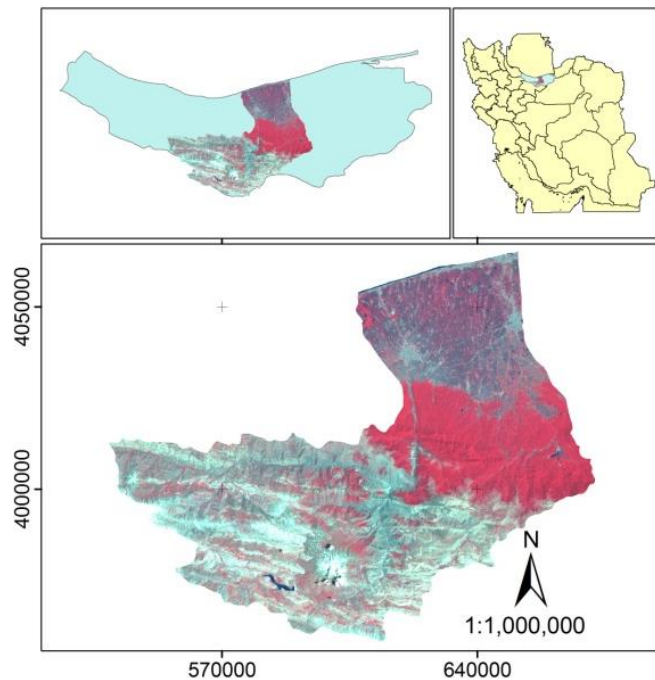


Figure 1. Location of study area in Mazandaran province, Iran

3. Materials and Methods

3.1. Data and Corrections

Landsat satellite images have been used for land use mapping in the beginning and end of the analyzed 15-years period (1996 & 2011). Before using satellite data, the radiometric and geometric errors correction was carried out using Ortho-rectification method with rivers, roads and DEM maps in PCI Geomatica software. In this study, observing of all the bands and different color composites showed the striped error and cloudy areas. Therefore, the classes of cloud and shadow were included in the classification.

3.2. Indices preparation

According to the results of some similar studies, and for better extraction of information, PCA and rationing analysis (SAVI & NDVI indices) were used for indices preparation. Since in PCA analysis, visible bands (1-3) and infra-red bands (4-7) have a high

correlation, it was used separately on these bands set. Then the resulted first components were used as artificial bands in classification. Also, a color composite (RGB432) was used for a better recognition of the area and making of training samples.

3.3. Classification

In this study, supervised classification method and Maximum Likelihood algorithm has been used to classify images. The Supervised Maximum Likelihood classification is the most common method in remote sensing image data analysis. It identifies and locates land cover types known prior through a combination of personal experience, interpretation of aerial photography, map analysis, and fieldwork. It uses the means and variances of the training data to estimate the probability that a pixel is a member of a class. The pixel placed in the class with the highest probability of membership (Haque and Basak, 2017).

The land use classes were: 1 bare land, 2 irrigated farming, 3 dense forests, 4 sparse forests and horticulture, 5 range-dry farming, 6 first-grade range, 7 second-grade range, 8 residential lands and 9 water. Before selecting the best band combination, training samples chosen separately for each image. RGB color composites, field control points, and aerial photos were used in the selection of training samples.

3.4. Accuracy assessment

To remove isolated pixels and to smooth the classified images, a 3×3 window mode filter was used. Then the accuracy of classifications was assessed using a point ground truth map including 130 points.

3.5. Change detection

After ensuring the accuracy of the classification, post classification change detection analysis was executed. For this purpose, each year land use map was converted to vector format. The polygon of the cloudy and striped area processed in GIS environment and converted to correct classes. By overlaying both period land use maps and using Dissolve function, the area percentage of different land uses; and the changed and unchanged areas for a period of 15 years were identified.

4. Results and Discussion

4.1. Data corrections

Geometric correction of images with remove topographic error was done using Ortho-rectification method with RMS error less than one pixel. Figure 2 shows high accuracy geometry correction.

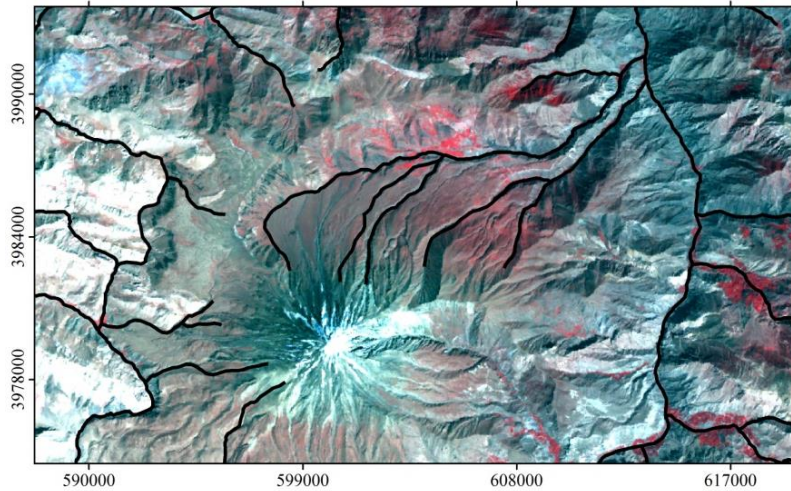


Figure 2. Situation of the image geometric matching

4.2. Indices

The different indices and color composites were generated to decrease the negative effect of inappropriate factor that exist in almost every band (with different quantities), increases the separation capability of the phenomena, and select the training samples. The images color composite (RGB432) and some indices have been shown in Figures 3-6. As that color composites indicate, the most land uses of the area consist range, dry farming, forest, and horticulture.

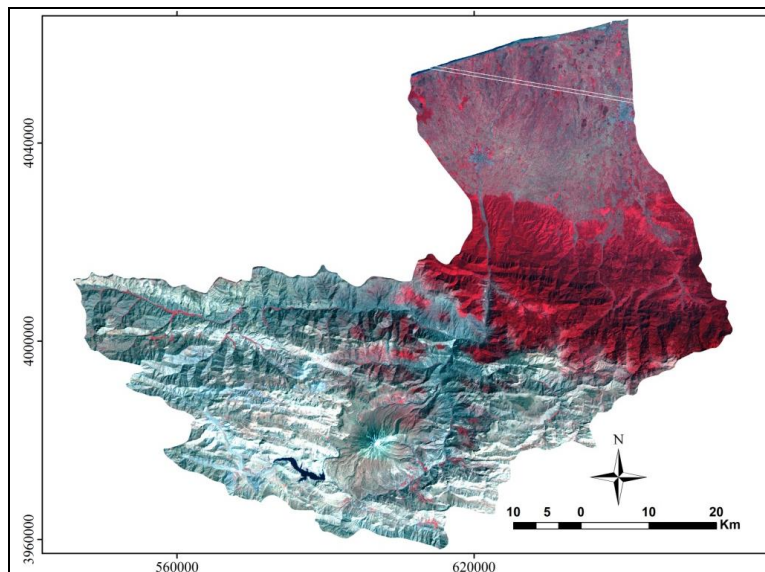


Figure 3. RGB₄₃₂ of 1996

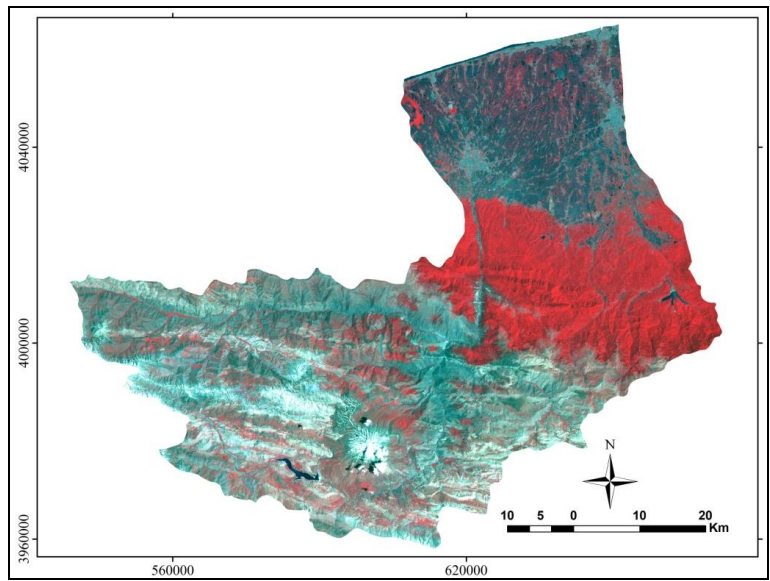


Figure 4. RGB₄₃₂ of 2011

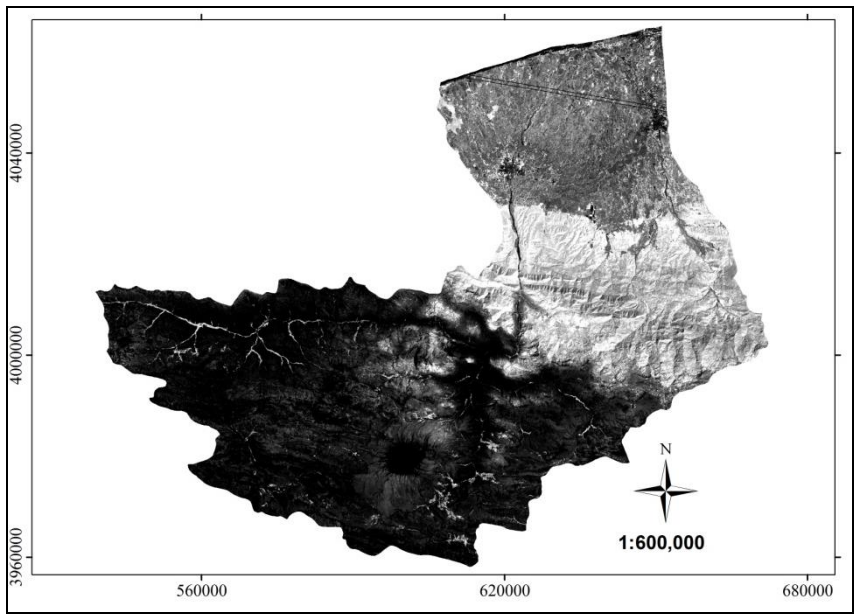


Figure 5. SAVI index of 1996

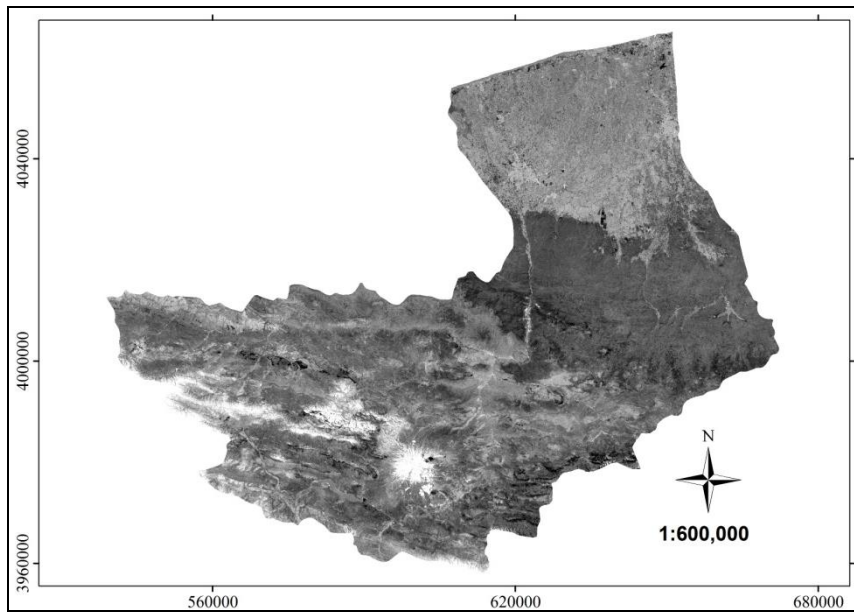


Figure 6. PC₁ (4567) index of 2011

4.3. Land use maps

Land use maps of 1996 and 2011 have shown in Figures 7-8, and Tables 1-2. These Tables and Figures indicates the study area land uses such as residential, farming, water resource, horticulture, forest, range, and bare lands. In 1996, the area percentage of different land uses including residential, farming, water bodies, horticulture and sparse forest, dense forest, first-grade range, second-grade range, dry farming, and bare lands are 0.87, 20.8, 0.38, 1.68, 20.46, 9.86, 8.5, 35.3, and 2.1 respectively. In 2011, the values are 5.04, 16.5, 0.76, 7, 14.4, 1, 7.5, 39, and 8.6. The main land uses were rangelands and range-dry farming in 1996. In 2011 there was an increase in the bare land and range-dry farming area. But, the area of dense forest decreased slightly, and rangelands area decreased significantly. Figure 9 shows the area of different land use classes for each period.

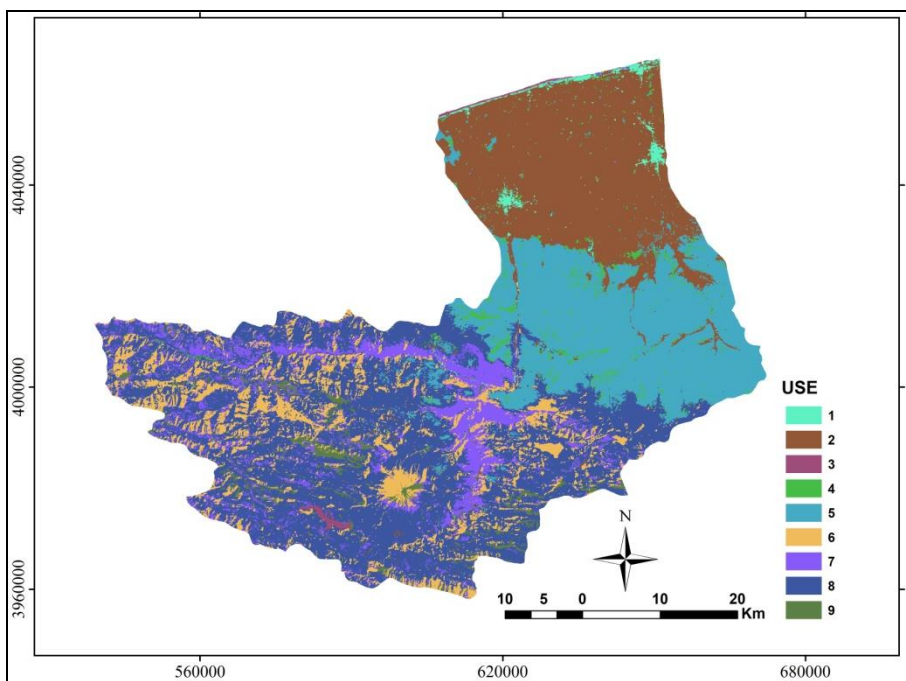


Figure 7. Land use map of 1996

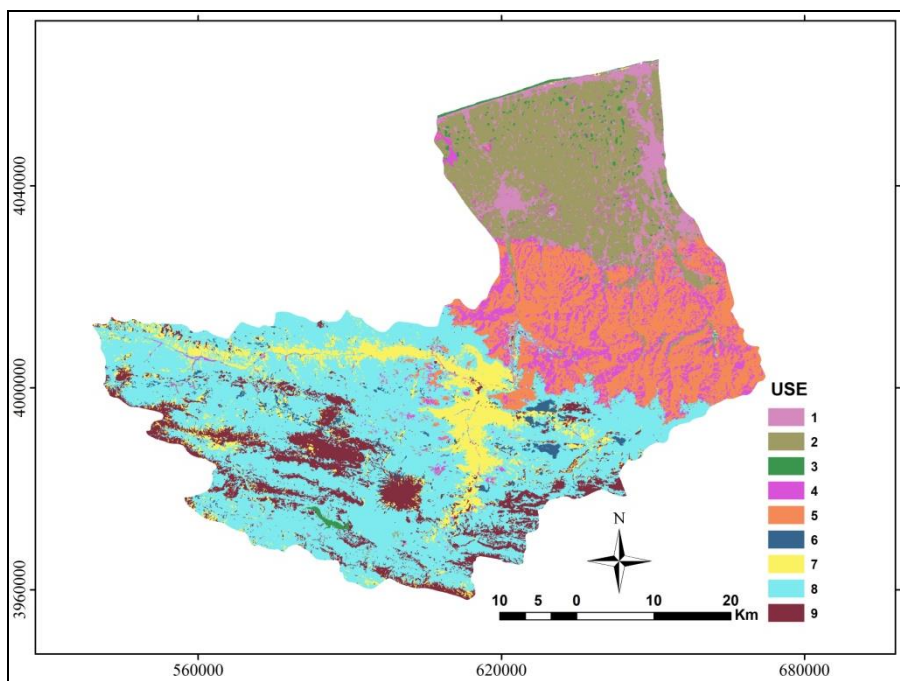


Figure 8. Land use map of 2011

Table 1. Land use area of 1996

Class	Land use 1996	Area (Ha)	Area (%)
1	Residential	5895.931028	0.870386
2	Farming Lands	140991.441	20.813843
3	Water Resource	2575.294254	0.380177
4	Horticulture & Low Density Forest	11443.45214	1.689338
5	Dense Forest	138636.3678	20.466175
6	First Grade Range	66807.17997	9.862401
7	Second Grade Range	57480.99581	8.485624
8	Range-Dry Farming	239283.772	35.324235
9	Bare Lands	14278.19849	2.107817

Table 2. Land use area of 2011

Class	Land use 2011	Area (Ha)	Area (%)
1	Residential	34192.2555	5.047627
2	Farming Lands	111564.8884	16.469752
3	Water Resource	5176.763136	0.764218
4	Horticulture & Low-Density Forest	47746.27049	7.048537
5	Dense Forest	97501.7859	14.393688
6	First Grade Range	7202.241924	1.06323
7	Second Grade Range	51109.25297	7.544996
8	Range-Dry Farming	263999.2077	38.972848
9	Bare Lands	58899.96656	8.695099

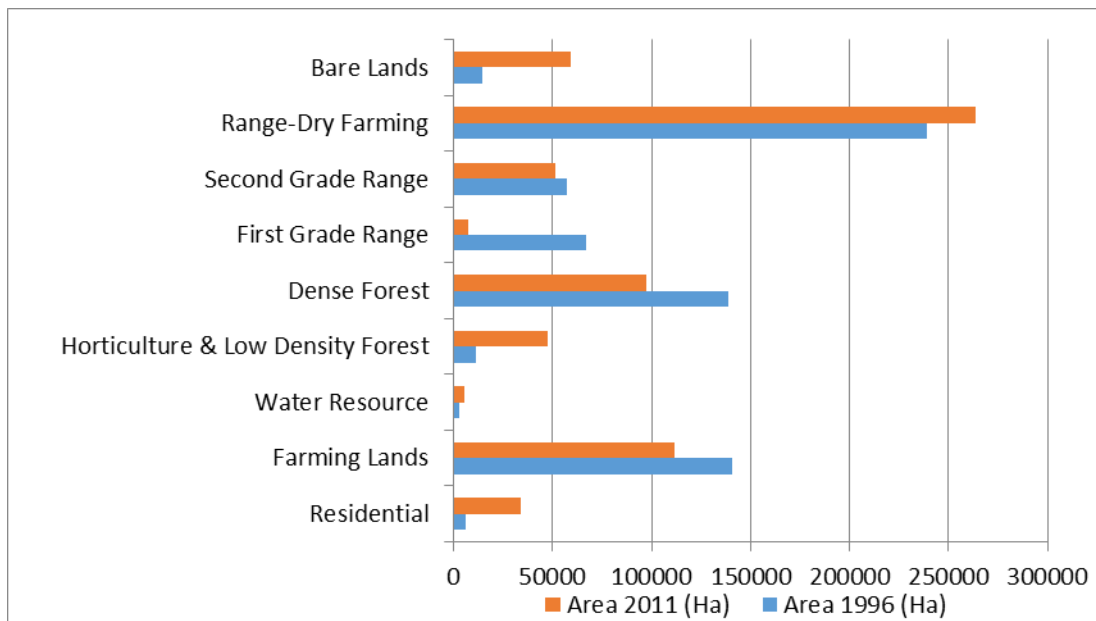


Figure 9. Area of different land use classes in 1996 and 2011

4.4. Land use changes

To understand the spatial changes for 15 years, Figure 10-11 displays the map of change detection for different classes as well changed and unchanged areas. As shown in the earlier studies, many land use changes have occurred in different parts of the world (Gandhi et al., 2015; Haque and Basak, 2017), this study illustrated that during the 15-year period, land uses has changed in 27.5% of the study area. About 16% of the changes the conversion of first- and second-grade rangelands to each other and other land uses.

About 6% of the changes were accounted for the conversion of dense forest to horticulture, sparse forest, farming and water resources and 5% was related to the conversion of farming to a residential, horticulture, and water resources. Also about 0.4% was accounted for the conversion of sparse forest and horticulture to farming land and residential area (Figure 10). In addition, it is noted, that, according to recent droughts, water resources of study area should show a decrease, but in 2011, an increase was observed which is due to the construction of a dam. All the above changes in line with some researchers (Basanna and Wodeyar, 2013; Utomo and Kurniawan, 2016) are positive and negative.

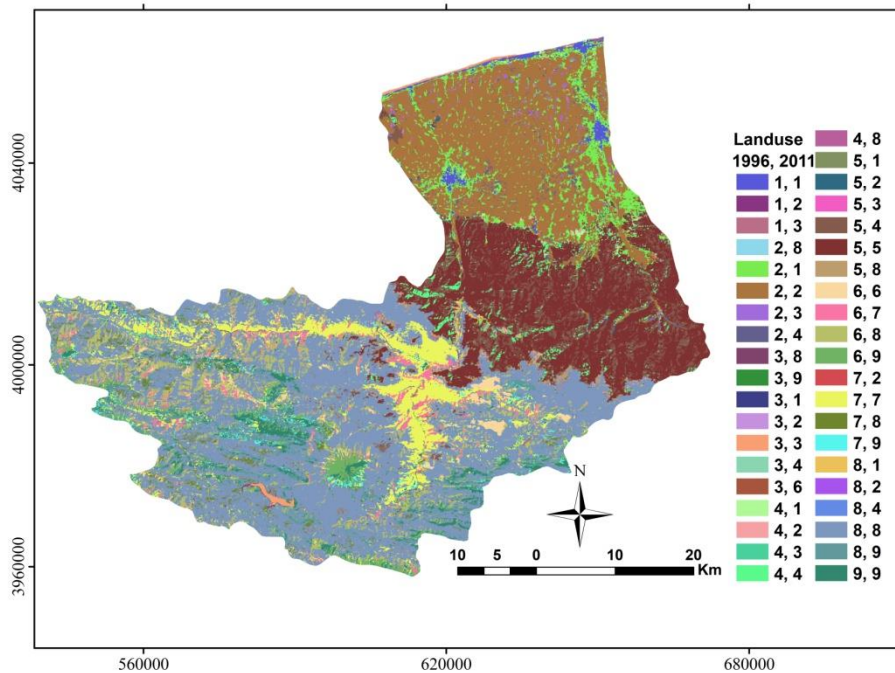


Figure 10. Land use changes of 1996-2011

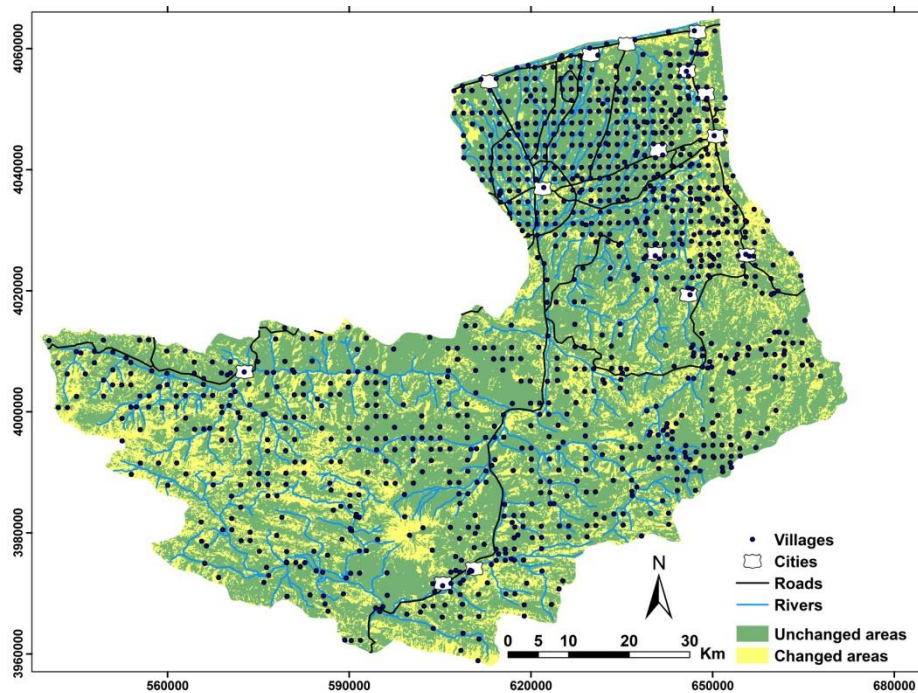


Figure 11. Location of changed and unchanged areas

In Figure 11, manmade phenomena such as roads, villages, and cities, as well as the waterway have been shown on the change map. The human-induced phenomena can lead to more destructive human activities. In this study, about one-third number of cities and villages, and about a quarter of the roads and waterway length was located in the changed areas. The presence of further waterway indicates the mountainous condition of the study area and its effects on soil erosion.

As we know, only phenomena located in the changed areas do not affect the land use change, but the phenomena in other areas can affect directly and indirectly the land use changes in adjacent and distant areas. The effects of these point and line phenomena are not limited to their location.

In addition to the impacts of human activities, climate change can also be another reason for land use changes. Moreover, the role of cultural and scientific educations, monitoring, and appropriate management by governmental and non-governmental organizations, as well as employment and poverty status and dependence degree of local communities on natural resources can also affect land use change rate.

This study has used digital remote sensing data as a spatiotemporal approach to detect land use changes. Similar studies have been done and the approach has been deemed suitable for analyzing the land use changes (Baboo and Devi 2010; Babykalpana and Thanushkodi 2011; Fichera et al. 2012; Yin and He 2012). In the current study, the Kappa statistics calculated for the classified Landsat images indicate high accuracy; which

suggests that Landsat imagery have high potential in land use mapping studies (Li et al., 2017).

The changes caused were mainly by human activities, which increased the demand for natural resources and often represented exploitative and unsustainable use (Githui et al., 2010; Sajikumar and Remya, 2015).

In line with some researchers (Haque and Basak, 2017; Singh and Singh, 2018), the results show that the method used has higher accuracy indicating the effectiveness of the method. The results show that remote sensing and geographic information system are providing effective techniques for the advanced ecosystem and socioeconomic management (Haque and Basak, 2017; Valjarević et al., 2018). Also these technologies are useful in acquiring more detailed insight into the condition of different land uses especially forests in the world (Valjarević et al., 2018).

As noted in earlier studies (Babykalpana and Thanushkodi, 2011; Haque and Basak, 2017), accurate and up-to-date land use/cover information is essential for environmental planning, to understand the impact on the terrestrial ecosystem and to achieve sustainable development. The change analysis can be helpful in predicting the unfortunate natural disasters to provide humanitarian aid, damage assessment and furthermore to device new protection strategies (Gandhi et al., 2015).

5. Conclusion

The obtained results are a warning for the future management of the Haraz Basin because 27% of the study area experienced land use change during the 15-year period. These changes can be due to an increase in population and human activities, which results in increasing demands for natural resources and converting them into farming lands, horticulture, residential and industrial areas. In addition, climate changes are effective on these conversions, which is due to human interference in natural ecosystems. The observed trend may continue in the future, leading to increasing environmental damage and loss of rangelands and forests. Therefore, analyses and predictions of future changes and effects on different processes are important for the efficient and sustainable use of resources, to prevent irreversible changes in the future.

References

- Baboo, S., & Devi, M. (2010). Integrations of remote sensing and GIS to land use and land cover change detection of Coimbatore district. *International Journal on Computer Science and Engineering*, 2(9), 3085-3088.
- Babykalpana, Y., & Thanushkodi, K. (2011). Classification of Land use/ land cover Changes Detection Using Remotely Sensed Data. *International Journal on Computer Science and Engineering*, 3(4), 1638-1644.

- Basanna, R., & Wodeyar, A. K. (2013). Supervised classification for LULC change analysis. *International Journal of Computer Applications*, 66(21).
- Fichera, C., Modica, G., & Pollino, M. (2012). Land cover classification and change detection analysis using multi-temporal remote sensed imagery and landscape metrics. *European Journal of Remote*, 45(1), 1-18.
- Gadrani, L., Lominadze, G., & Tsitsagi, M. (2018). F assessment of landuse/landcover (LULC) change of Tbilisi and surrounding area using remote sensing (RS) and GIS. *Annals of Agrarian Science*. In Press, Accepted Manuscript, Available online 21 April 2018.
- Gandhi, G. M., Parthiban, S., Thummalu, N., & Christy, A. (2015). NDVI: vegetation change detection using remote sensing and GIS—A case study of Vellore District. *Procedia Computer Science*, 57, 1199-1210.
- Githui, F., Mutua, F., & Bauwens, W. (2010). Estimating the impacts of land-cover change on runoff using the soil and water assessment tool (SWAT): case study of Nzoia catchment, Kenya. *Hydrological Sciences Journal*, 54(5), 898-908.
- Haque, M. I., & Basak, R. (2017). Land cover change detection using GIS and remote sensing techniques: A spatiotemporal study on Tanguar Haor, Sunamganj, Bangladesh. *The Egyptian Journal of Remote Sensing and Space Science*, 20(2), 251-263.
- Hosseinzade, M. M., Esmaeli, R., Nohegar, A., & Saghafi, M. (2009). Forest change detection in northern slopes of Alborz. *Environmental Science Journal*, 7(1), 1-20.
- Kamkar, B., & Mahdavi-Damghani, A. (2012). Principles of sustainable agriculture. Mashhad University Press.
- Lal, A. M., & Anouncia, S. M. (2015). Semi-supervised change detection approach combining sparse fusion and constrained k means for multi-temporal remote sensing images. *The Egyptian Journal of Remote Sensing and Space Science*, 18(2), 279-288.
- Li, H., Wang, C., Zhong, C., Zhang, Z., & Liu, Q. (2017). Mapping typical urban LULC from Landsat imagery without training samples or self-defined parameters. *Remote Sensing*, 9(7), 700.
- Matkan, A. A., Saedi, K. H., Shakiba, A., & Hossieni-Asl, A. (2010). Evaluation of land cover changes related to construction Taleghan Dam using Remote sensing techniques. *Applied Researches of Geographical Science Journal*, 16(19), 45-64.
- Mohammadi, M., Moradi, H. R., Faiznia, S., & Poorghasemi, H. M. (2009). Comparison of the efficiency of certainty factor, information value and AHP models in landslide hazard zonation. *Journal of Range and Watershed management, Iranian Journal of Natural Resources*, 62(4), 539-551.
- Nowroozi, M., Vahab-Zadeh, G.H., Solaimani, k., & Shaabani, M. (2012). Application of GIS and remote sensing in modeling land use change detection for environmentally sustainable development. *Second Conference on Planning and Management of Environment*, Tehran.
- Sajikumar, N., & Remya, R. S. (2015). Impact of land cover and land use change on runoff characteristics. *Journal of Environmental Management*, 161, 460-468.

- Singh, A., & Singh, K. K. (2018). Unsupervised change detection in remote sensing images using a fusion of spectral and statistical indices. *The Egyptian Journal of Remote Sensing and Space Science*.
- Sreenivasulu, V., & Bhaskar, P. (2010). Change detection in land use and land cover using remote sensing and GIS techniques. *International Journal of Engineering Science and Technology*, 2(12), 7758-7762.
- Utomo, D. H., & Kurniawan, B. R. (2016). Spatiotemporal analysis trend of land use and land cover change against temperature based on remote sensing data in Malang City. *Procedia-Social and Behavioral Sciences*, 227, 232-238.
- Vafaei, S., Darvishsefat, A. A., & Pir-Bavaghar, M. (2013). Monitoring and predicting land use changes using LCM module. *Iranian Journal of Forest*, 5(3), 323-336.
- Valjarević, A., Djekić, T., Stevanović, V., Ivanović, R., & Jandzicković, B. (2018). GIS numerical and remote sensing analyses of forest changes in the Toplica region for the period of 1953–2013. *Applied Geography*, 92, 131-139.
- Willis, K. S. (2015). Remote sensing change detection for ecological monitoring in the United States protected areas. *Biological Conservation*, 182, 233-242.
- Yin, J., & He, F. (2012). Researching relationship between the change of vegetation cover and runoff based and RS and GIS. *Procedia Environmental Sciences*, 12, 1077-1081.

A Study of Bioecological and Land Cover Change of Northern Lands of Khuzestan by Remote Sensing

Sara Shirzad^a, Babak Maghsoudi Damavandi^b, Hamed Piri^{c*}

^a Department of Agronomy, Khorramshahr-khalij fars International Branch, Islamic Azad University, Khorramshahr, Iran.

^b Department of Agronomy, Khorramshahr-khalij fars International Branch, Islamic Azad University, Khorramshahr, Iran.

^c young researchers and Elite club, Safadasht Branch, Islamic Azad university, Tehran, Iran.

Received 7 April 2018; revised 22 May 2018; accepted 3 June 2018

Abstract

Remote sensing is a useful technology as a superior to other methods thanks to features like vast and integrated view of the area, repeatability, accessibility and high precision of information, and saving in time. Vegetation index is extensively used nowadays in different continental, regional, and areal scales. Due to the excessive use of natural resources, the area of landscapes has been changing day to day, and updating of the maps is a costly and time-consuming task. Thus, many of the well-developed countries take benefit of satellite data at different levels. The analysed factors included 1-preparation of vegetation and land use maps of North Khuzestan; 2-assessment of biological potentials in agriculture development of the studied area using WLC and weighted overlay technique.

Based on the acquired results and performed computations, it was demonstrated that the variations in the pasture and agriculture soil during the years from 2003 to 2014 were 19 percent, and a significant reduction is observed in this part of land use. The changes between the years 2014 to 2016 were equal to approximately 11 percent according to the computations. This value is remarkably high and indicates the intensity of changes during the recent years.

Keywords: Remote Sensing, Landsat Images, Vegetation, Agriculture Development

* Corresponding author. Tel: +98-2165438414.

E-mail address: piriamed@gmail.com.

1. Introduction

Keeping in mind Iran's population growth rate, destruction of natural resources, water and agriculture land deficiency as well as environmental pollutions, it shall be accepted that we are facing the crises associated with natural environments, the respective crises have unprecedentedly pervaded human activities, mass and energy exchange, and dependent natural subsets at the present age (Yousefi et al 2011). Repeated occurrence of floods in Iran, destruction of a vast expanse of forests (severe deforestation), desertification, and abandonment of farmlands due to immigration of villagers to the cities have imposed highly critical conditions to the ecological environments. And, it is not unlikely to lead to loss of all assets of fertile agricultural lands in less than half-century.

It is evident that Iran's natural environments have limited ecological capability for human use. In certain environments, nature is ready for development incurring least damages, whereas in others, unsustainable development has resulted in environmental destruction, implying that the ecological potential of any natural environment shall be evaluated before implementing the development plans therein (SANAIE et al., 2006).

Remote sensing is one of the greatly beneficial methods for acquisition of information concerning vegetation. Providing a vast view of the area, data repeatability and integration are among the characteristics of the respective technology, causing the researchers to utilize this technique for their studies (Dube and Mutanga 2015).

Yang stated that access to updated and new statistics and information and awareness of the trend of variations is one of the key factors in planning, decision-making, and managerial tools in any organization, which will be enabled via deployment of detection process of land use variations (Yang et al., 2015). Perera studied land uses in Sri Lanka using GIS and determined land suitability for cultivation of agricultural crops. They divided their area of study into four units based on parameters of slope, soil type, land capability, and irrigation mechanism. They subsequently evaluated land suitability for each unit using analysis of the maps and relevant information in GIS environment (Perera et al., 2001).

Satellite images are capable of assessing cultivation area of major crops and their health. Also, yield of products in different areas can be predicted and their marketing can be planned in different areas depending on the demand level (Singh et al., 1999). When the plants are attacked by pests, their reflections differ at different wavelengths (Schowengerdt 1997). Water deficiency in leaf causes changes in absorption and reflection of electromagnetic waves. In other words, reflection of a leaf with water-saturated membrane is different from that a leaf suffering from water deficiency at varying wavelengths (Jeong and Howat 2015).

Today, via transmission of images from movement of clouds, position of high-pressure systems, and so on, meteorological satellites can help us get aware of presence of precipitation in the area approximately or with an acceptable probability. Hence, the farmers can plan the cultivation time with further assurance based on the weather forecast.

Also, the moisture content of soil can be analyzed using RADAR images (Peña and Brenning 2015).

Anderson reviewed GIS and deployment of systematic approach toward environmental planning. Objectives of the respective plan included determination of relationship between diversity, production, stability and existing pressures as well as models of water and soil ecosystems, and ultimately, utilization of the results of this type of attitude in larger areas and at different scales.

In planting stage, satellite images, and in particular, RADAR images may help the farmers for better preparation of the land (Jiménez et al., 2014).

Water erosion caused by floods and torrential rains lead to destruction of agriculture lands. And, this destruction is completely visible in satellite images. Appropriate planning can be made by identifying the eroded areas and causes of erosion can be determined and plans can be proposed to mitigate or alleviate erosion (Yu et al., 2014).

In recent years, in Iran, the assessment of the bio-ecological potential of development as a necessity in planning the use of land use has been raised. This is happening in economic, social and cultural programs. Khuzestan has vast and fertile lands and It is necessary to use ecological techniques to evaluate ecological power using new techniques such as remote sensing and geographic information systems. After recognizing the principles of optimal use, the findings are considered in future plans. The purpose of this plan is to estimate the change in agricultural land between 2003 and 2016 in a part of Khuzestan. Hypotheses are When it comes to the last few years, a change has been made and Agricultural lands have fallen.

Geographical location and Tectonics of Khuzestan

Khuzestan is located in the southwest of the country, Contract Between geographic length $32^{\circ} 50'$ - $30^{\circ} 50'$ Oriental and Latitude geography $47^{\circ} 50'$ - $48^{\circ} 50'$ North. The northern part is high and mountain with Moderate summer and cold winter but the southern part is mountainous and like plain. The weather is in this part of the semi desert.

2. Area of study: North of Khuzestan –Iran-

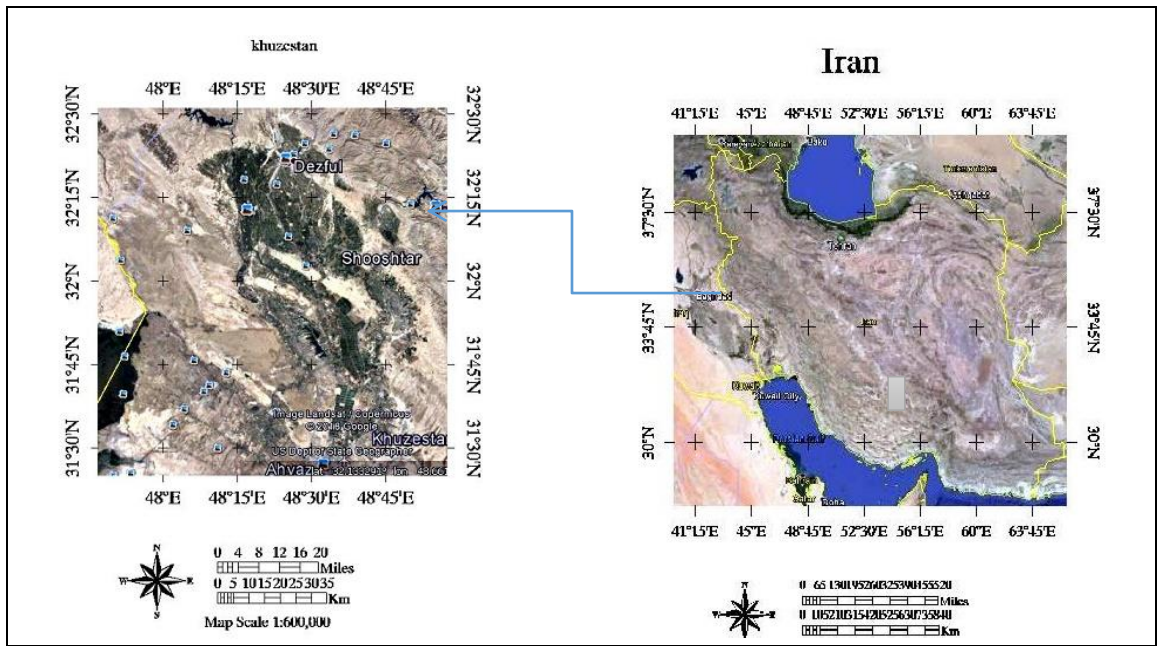


Figure1. Area study

2.1 Geological features

From morphological point of view three morphological structures dominate the province of Khuzestan. The first part is the structures that led to the formation of folded mountains in the northeast of the province. Second, the structure of the hills that surrounds areas of Dezful, Ramhormoz and Ahvaz.

Alluvial plains and floodplains located in the south of Ahvaz to the Persian Gulf coast that alluvial and flood deposits have been deposited there.

The composition of the geological formations lithology, the density and erosion of rocks and the origin of the sediment affect the mentioned morphology (terrane) of tectonic phenomena.

The structural position of Khuzestan province is located in semimetal tectonic state of Zagros that has a special sedimentary history and structure. The mountainous part of Khuzestan is an example of folded mountainous masses that in terms of rocky and tectonic features and following the general process of Zagros geological structure, which extends in the northwest - southeast, is called folded Zagros. But in the southwestern front of this mountain, especially around the Masjed Soleyman, southwest of Ramhormoz, Rags fid Mountain and in the southern anticline of Ahvaz, there are drifting to the southwest that due to tectonic processes in the Zagros sedimentation basin, there have been a lot of thrills in sediments, which is why it is called folded-drifted Zagros. The northern margin of the

Khuzestan plain is part of an indicator tectonic structure which is called Dezful downfall. This downfall is a kind of pre-arc basin formed in the southwest of the mountain front of the northeast of Khuzestan province. One of the geological characteristics of this downfall, is the high thickness of the sedimentary layers between 16 and 18 meters, which made it as one of the oil-rich regions of the province and Iran by forming good reservoir rocks.

The geological formations of the Khuzestan area is a part of folded-drifted Zagros which are formed in different sedimentary and tectonic conditions, Therefore, due to the time and conditions of sedimentation and tectonic location, various facial differences have been formed. Based on three factors of lithology, Tec tonicity and age, the geological formations of the province can be divided into following two tectonostratigraphic units:

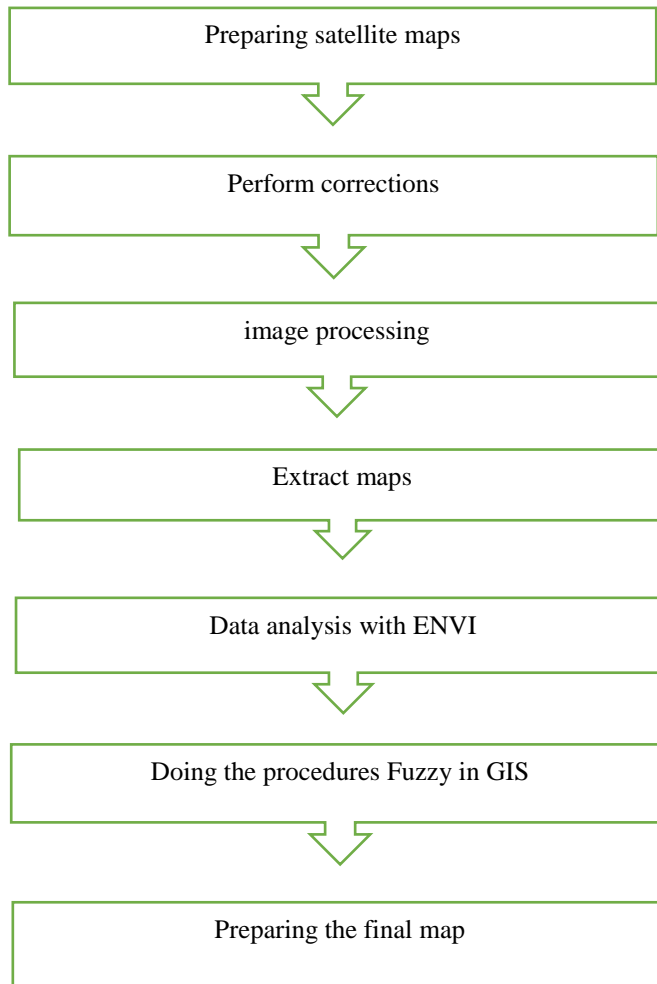
Based on geological-structural divisions of Iran, Khuzestan province is located in the structural zones of Khuzestan Plain, folded Zagros and Zagros highlands.

Khuzestan Plain is part of the vast Mesopotamia Plain, which is part of the Arabic Platform. Khuzestan plain is simple in construction and it has just a very mild bending in the north-south axis, which adheres to the general axial folding of the Arabic platform, and first, second and third era constructions exist in that. Determination of the boundary between Khuzestan plain with the folded Zagros region is not completely clear in terms of superficial changes; because the Neogene lagoon sediments, which thicken to the west, have covered both zones in the same way.

The Zagros Crushed Zone unit with width of 150 to 250 kilometers is located in the southwest of Iran, and its general trend is from northwest to southeast, and Paleozoic, Mesozoic and Cenozoic sediments are aligned on each other with the same slope and these structural units evolved over three stages.

3. Materials and Methods

Basic statistics and statistics and information include topography, soil properties, water resources, and climatic parameters based on which the other maps are prepared. In the present research, after performing the correction and processing of LANDSAT satellite images, the land use map of the area was extracted and the information were analyzed in GIS environment using Envi and ArcGIS software packages. Land capability assessment maps were then prepared by means of fuzzy and weighted overlay techniques. At the last stage, the maps were integrated based on land use priorities and the land use capability map was prepared. Envi and ArcGIS software packages and multiple-criteria analysis and fuzzy methods were used to analyze the data of the prepared map.



4. Results and Discussion

Destruction of these lands will have many environmental and economic consequences. The environmental values of the pastures are several times its economic value, which is forage. In this way, it is safe to say that by destroying or changing the use of a rangeland, though small, a living part of nature is lost. One of the problems encountered in these areas is unnecessary exploitation and overcapacity (De Alban et al., 2018), which leads to a decline in the quality and quantity of these resources. Changing the use of rangelands in

addition to grazing over capacity, which has always been a serious threat to rangelands, mass transfer and alteration of their use is one of the major problems that threatens the existence of rangeland ecosystems and in recent years this has happened in the region The study has been conducted. And lands with vegetation have been altered to other lands (Ahmadi and Vahid 2018). Due to population growth over the period, farmers were forced to plow plenty of pasture land and change their use.

Investigating the studies of other colleagues and researchers in recent years in the same areas indicates tangible changes in the land so that farmers and rangelands are hardly able to cope with their agronomic needs.

This research was carried out with respect to the importance of the study area using satellite imagery. Landsat images were used in this study. Following preparation of images and applying the required preprocessing operations, supervised classification was carried out by means of maximum likelihood estimation technique (Pirnazar et al., 2018). For this purpose, four major classes namely vegetation, urban areas, soil, and water were considered. The classification results were then estimated for all three years i.e. 2003 and 2014 and 2016. (Figure 2.3.4)

The results of changes in use for each of four geographical features in two periods of 2003 to 2014, as well as 2014 to 2016, are presented as percentages as well as the level of changes. According to the results and calculations, the amount of changes in the vegetation cover between years 2003 and 2014 was 19 percent, and there is a significant reduction in this part of the use. The same proportion is 11% just in two years of 2014 until 2016, which is significant comparing with the 11-years period between 2003 and 2014. (Figure 3.4)

Also, the changes between 2003 and 2014 in residential sectors are -43%, considering that the changes between 2014 and 2016 (in only two years) are -15%.

Changes in soil maps are much more impressive than other areas. Just over two years of 2014 and 2016, we see about 2 percent of the change but from 2003 to 2014, this change was only -4% in 11 years. (Figure 3.4)

In terms of regional water change, it was -11% between 2003 and 2014, but in period of 2014 to 2016 it was about -67% that is a very contemplative number.

Consequently, and considering the above factors in the bio-ecological subject, it can be verified that changes over the two years' period of 2014-2016 are very important and demographic changes and dominant faunas in the region are subject to severe fluctuations, and water shortages and high rates of underground utilization will result in irreparable damages in the future.

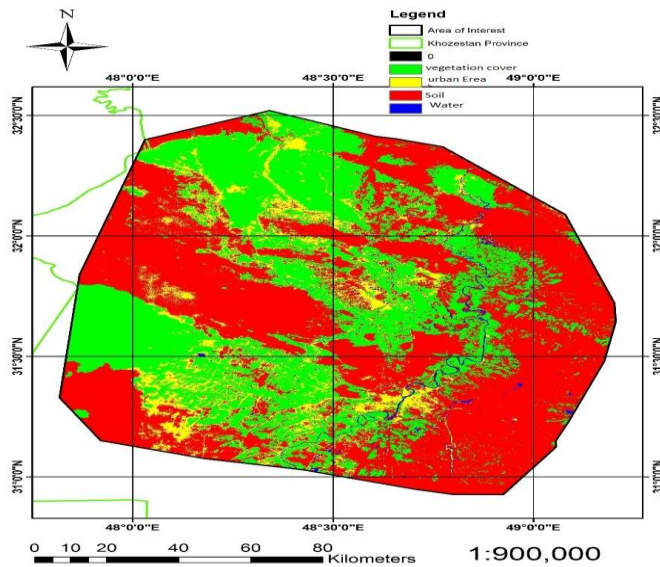


Figure2: Classification results of topographies for data of the year 2003

Overall Accuracy = $(122808/127479)$ 96.3359%

Kappa Coefficient = 0.9367

Ground Truth (Pixels)					
Class	veg	City	Soil	water	Total
Unclassified	0	0	0	0	0
veg[Green]4	4753	56	27	2	47616
City[Yellow]4	5	8632	4053	2	12732
Soil[Red]68	30	456	64499	0	64985
water[Blue]	0	0	0	2146	2146
Total	47606	9144	68579	2150	127479

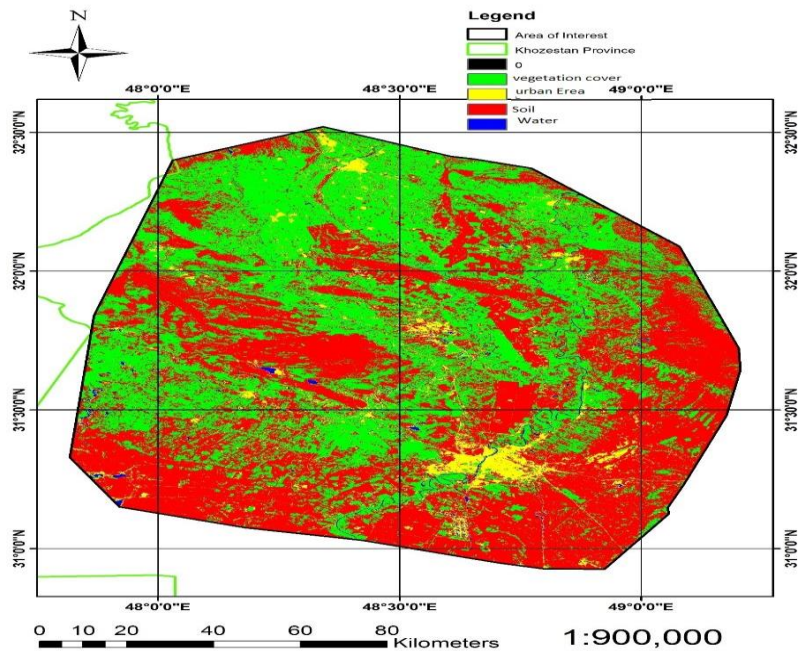


Figure 3: Classification results of topographies for data of the year 2014

Overall Accuracy = (104761/105691) 99.1201%

Kappa Coefficient = 0.9803

Ground Truth (Pixels)					
Class	veg	city	soil	water	Total
Unclassified	0	0	0	0	0
veg[Green]1	13790	60	525	7	14382
city[Yellow] 2		11972	170	8	12152
soil[Red]76	44	114	75887	0	76045
water[Blue] 0		0	0	3112	3112
Total	13836	12146	76582	3127	105691

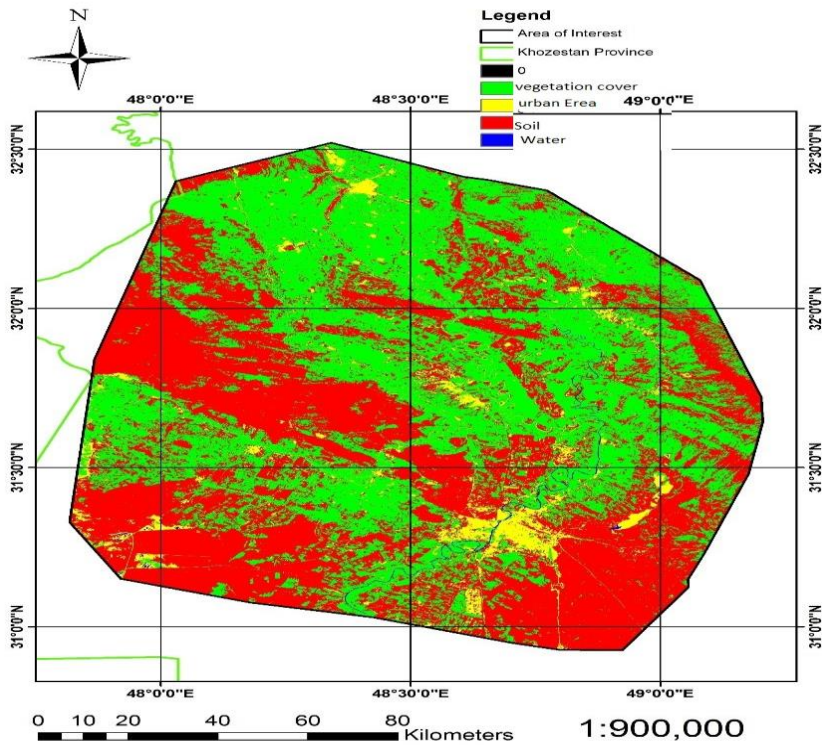


Figure 4: Classification results of topographies for data of the year 2016
 Overall Accuracy = $(294586/297814)$ 98.9161%

Kappa Coefficient = 0.9775

Ground Truth (Pixels)					
Class	Veg	city	soil	water	Total
Unclassified	0	0	0	0	0
veg [Green] 1	103238	24	1284	0	104546
city [Yellow]	277	5777	368	2	6424
soil [Red] 18	1241	31	185379	0	186651
water [Blue]	1	0	0	192	193
Total	104757	5832	187031	194	297814

Figure above illustrates classification results of land uses for four types of topographies during the interval from 2003 to 2014 and also from 2014 to 2016 as percentage as well as variation level.

Table 1: Topography changes during the interval from 2003 to 2014 in terms of percentage and area

	Vegetation	residential areas	soil	water
Vegetation	66.615	32.929	17.365	21.562
residential areas	5.145	17.821	3.029	18.512
soil	27.762	47.649	79.341	27.417
water	0.478	1.601	0.265	32.509
total	100	100	100	100
Percentage change level	19.556	-43.297	-2.033	-11.577
	Vegetation	residential areas	soil	water
Vegetation	4076.0892	668.8143	2531.8278	38.7243
residential areas	314.8038	361.9701	441.675	33.2469
soil	1698.7275	967.8096	11567.8395	49.239
water	29.2563	32.5143	38.6487	58.3839
total	6118.8768	2031.1083	14579.991	179.5941
Percentage change level	1196.5788	-879.4125	-296.3754	-20.7909

Table 2: Topography changes during the interval from 2014 to 2016 in terms of percentage and area

	Vegetation	residential areas	soil	water
Vegetation	75.268	28.982	16.35	7.553
residential areas	1.9	43.145	1.764	53.785
soil	22.807	27.285	81.841	15.232
water	0.025	0.588	0.045	23.431
total	100	100	100	100
Percentage change level	11.918	-15.487	-4.109	-67.129
	Vegetation	residential areas	soil	water
Vegetation	5506.1892	333.7821	2335.3542	11.9943
residential areas	139.0212	496.8936	252.0072	85.4118
soil	1668.4254	314.2449	11689.857	24.1884
water	1.8198	6.7752	6.3972	37.2087
total	7315.4556	1151.6958	14283.6156	158.8032
Percentage change level	871.8642	-178.362	-586.8999	-106.6023

5. Conclusion

Based on the results and calculations it was shown that the changes in the vegetation cover are positive but not very large changes, because satellite images and their analysis show this. But the point to be considered is a lot of changes in the water zone of this region, which is very impressive and shows a significant decrease. The over usage of groundwater and the reduction of surface water and the reduction of precipitation in the years between 2014 and 2016 are indicative of this issue.

Due to the increase in agricultural vegetation and the reduction of water in the area, this increase seems to be in line with the higher usage of groundwater and the expansion of agricultural land and rangelands is the reason of these waters usage.

References

- Anderson MC, Allen RG, Morse A, Kustas WP. 2012. Use of Landsat thermal imagery in monitoring evapotranspiration and managing water resources. *Remote Sensing of Environment*, 122: 50-65.
- Dube T, Mutanga O. 2015. Investigating the robustness of the new Landsat-8 Operational Land Imager derived texture metrics in estimating plantation forest aboveground biomass in resource constrained areas. *ISPRS Journal of Photogrammetry and Remote sensing*, 108: 12-32.
- Jiménez-Muñoz JC, Sobrino JA, Skoković D, Mattar C, Cristóbal J. 2014. Land surface temperature retrieval methods from Landsat-8 thermal infrared sensor data. *IEEE Geoscience and Remote Sensing Letters*, 11(10): 1840-1843.
- Jeong S, Howat IM. 2015. Performance of Landsat 8 Operational Land Imager for mapping ice sheet velocity. *Remote Sensing of Environment*, 170: 90-101.
- Mohammadi, J. 2005. Stimating of volume of standing trees and separating the age levels using satellitic data. Faculty of Natural Sources, Gorgan University.
- Peña M, Brenning A. 2015. Assessing fruit-tree crop classification from Landsat-8 time series for the Maipo Valley, Chile. *Remote Sensing of Environment*, 171: 234-244.
- Schowengerdt, R. A. 1997. *Remote sensing, models and methods for image processing*. Academic Press, United States.
- Singh, S., S. Agarwal, P. K. Joshi, and P .S. Roy. 1999. Biome level classification of vegetation inwestern India-an application of wide field view sensor (WiFs). Joint Workshop of ISPRS Working Groups I/1, I/3 and IV/4: Sensors and Mapping from Space, Hanover
- Yang J, Wong MS, Menenti M, Nichol J. 2015. Study of the geometry effect on land surface temperature retrieval in urban environment. *ISPRS Journal of Photogrammetry and Remote Sensing*, 109: 77-87.

- Yousefi, S., M. Tazeh, S. Mirzaee, H. R. Moradi, and S. H. Tavangar. 2011. Comparison of different classification algorithms in satellite imagery to produce landuse maps (Case study: Noor city). *Journal of Applied RS and GIS Techniques in Natural Resource Science* 2 (2): 15-23.
- Yu X, Guo X, Wu Z. 2014. Land surface temperature retrieval from Landsat 8 TIRS— Comparison between radiative transfer equation-based method, split window algorithm and single channel method. *Remote Sensing*, 6(10): 9829-9852.
- Pirnazar, Mojtaba & Ostad-Ali-Askari, Kaveh & Eslamian, Saeid & Singh, Vijay & Dalezios, Nicolas & Ghane, Mohsen & Qasemi, Zahra. (2018). Change Detection of Urban Land Use and Urban Expansion Using GIS and RS, Case Study: Zanzan Province, Iran. *International Journal of Constructive Research in Civil Engineering*. 4. 10.20431/2454-8693.0401003
- De Alban, Jose Don & Connette, Grant & Oswald, Patrick & Webb, Edward. (2018). Combined Landsat and L-Band SAR Data Improves Land Cover Classification and Change Detection in Dynamic Tropical Landscapes. *Remote Sensing*. 10. 306. 10.3390/rs10020306
- Ahmadi, Vahid. (2018). Deforestation Prediction Using Neural Networks and Satellite Imagery in a Spatial Information System.